UC Santa Barbara
UC Santa Barbara Electronic Theses and Dissertations

Title

Nucleation and Order of a Polymer in a Confined Liquid Crystal Matrix

Permalink

https://escholarship.org/uc/item/3sj101mg

Author

Liu, Lan

Publication Date

2019

Peer reviewed|Thesis/dissertation

University of California
Santa Barbara

Nucleation and Order of a Polymer in a Confined Liquid Crystal Matrix

A dissertation submitted in partial satisfaction
of the requirements for the degree

Doctor of Philosophy

in

Mathematics

by

Lan Liu

Committee in charge:

      Professor Hector D. Ceniceros, Co-Chair
      Professor Xu Yang, Co-Chair
      Professor Carlos J. Garcia-Cervera

June 2019

The Dissertation of Lan Liu is approved.

_____

Professor Carlos J. Garcia-Cervera

_____

Professor Xu Yang, Committee Co-Chair

_____

Professor Hector D. Ceniceros, Committee Co-Chair

June 2019

Nucleation and Order of a Polymer in a Confined Liquid Crystal Matrix

To my family, mentors, friends, collaborators . . .
who believe in me and give me guidance

Acknowledgements

Curriculum Vitæ
Lan Liu

Education

2019	Ph.D. in Mathematics (Expected), University of California, Santa Barbara.
2016	M.S. in Mathematics, University of California, Santa Barbara.
2013	B.S. in Mathematics, Shanghai Jiaotong University, Shanghai, China.

Experience

2014-2019	Graduate Teaching Assistant, UCSB.
2015 Summer	Graduate Research Assistant, UCSB.
2016 Summer	Graduate Teaching Associate, UCSB.
2017 Summer	Graduate Teaching Associate, UCSB.
2018 Summer	Data Scientist Intern, Twilio Inc., San Francisco.

Awards

2013	Shanghai Outstanding Graduate Award
2015	Raymond L. Wilder Award
2019	Honorable mention for the GSA Excellence in Teaching Award

Talks

"Projection Method Over Cavity Flow" by L. Liu, SIAM, Jan 2016.
"Harmonic Extension and its Application in Semi-Supervised Learning" by L. Liu, SIAM, April 2018.

Publications

"Nucleation and Order of a Polymer in a Confined Liquid Crystal Matrix" by L. Liu, S. Joo, X. Yang, C.J. García-Cervera and H.D. Ceniceros; Communications in Computational Physics, Submitted, 2019.

Abstract

Nucleation and Order of a Polymer in a Confined Liquid Crystal Matrix

by

Lan Liu

Phase separation of a binary mixture, which consists of isotropic fluid, such as a flexible polymer, and nematic liquid crystal, can be induced from temperature quench. The separation process proceeds through the initial nucleation of small particles and subsequent growth and coarsening, and a variety of final morphologies can be obtained. This work is focused on the numerical investigation of nucleation and ordered structure formation of a flexible polymer in a nematic liquid crystal matrix confined between two parallel walls in both a 2D and a 3D channel geometry. The model is of Landau-de Gennes type for a conserved, compositional order parameter and a non-conserved, orientational tensor order parameter and allows a study of the system at the nanoscale.

This is the first time the full model has been utilized to learn the phase separation in confined geometries for a 3D geometry. The resulting system is numerically stiff, with several high order nonlinear coupled terms. In addition, to preserve the total volume of the species and be consistent with the variation of the free energy, a nontrivial boundary condition has to be enforced at the walls. These pose a significant numerical challenge that we overcome with the implementation of a linearly implicit method and an extrapolated boundary condition.

Our numerical investigation focuses on the effects of wall and surface anchoring on the nucleation of ordered, polymer-rich domains as well as in the selection of lamellae. In addition, the role of different energies in the system, and the elastic dipole configuration which critically contributes to the formation of structures are also explored.

In 2D, we find that chains of polymer-rich droplets nucleate, starting at the walls and aligned with them, and continue to form until they fill up much of the channel. Without orientational defects observed in the liquid crystal-rich phase, the droplets eventually coalesce, coarsen, and the linear chain order is destroyed. We have justified this by showing that the dipole defect cannot be sustained by the Landau-de Gennes model and instead it splits into two $-1/2$ point defects in a 2D channel and a $-1/2$ disclination ring in a 3D channel. In 3D, the polymer nucleates into layers of cylindrical structures, instead of droplets, whose principal axis is oriented with the wall anchoring angle. We also find that when the liquid crystal component is initially in isotropic state, stable equilibrium lamellae can be obtained for both homeotropic and planar surface anchoring conditions, in 2D and 3D.

Contents

x

Chapter 1

Introduction

Nematic liquid crystals (LC) are an intermediate phase of matter between the commonly observed solid and liquid states of matter, it possess anisotroic properties characterized by the orientational order of molecules [1]. The average orientation of the molecules is referred as the director $\boldsymbol{n}$, which is a unit pseudovector with $\boldsymbol{n}$ and $-\boldsymbol{n}$ represent the same state physically, and this is called head-to-tail symmetry. This anisotropic property makes nematic LC useful in a wide range of electro-optical applications such as LC displays and beam steering devices for optical communication. In most technological applications, the liquid crystal material is not pure but a mixture of two or more species. For example, nematic LCs have used as solvents for micro emulsions or particle dispersions in bio-molecular sensors or in self-assembly structures. LC materials sandwiched between two glass plates are also investigated frequently. In the confined geometries, the surfaces can be treated to impose preferential orientational order, which leads to formation of the regions where the director field is not continuous, these lines or points regions are called topological defects.

In recent years, phase separation of binary mixture containing nematic liquid crystal component has attracted increased attention as it offers a significant potential for techno-

logical innovation [2, 3, 4, 5, 6, 7, 8, 9, 10, 11, 12, 13, 14, 15]. After a temperature quench, the phase separation proceeds through a fast initial nucleation of small particles, subsequent slow growth, coarsening until a steady state is reached [16, 17], and different equilibrium states can be obtained. For example, polymer-dispersed liquid crystals (PDLCs) which consist of an isotropic polymer matrix and a liquid crystal droplet phase are being used in switchable windows, displays, spatial light modulators, tunable filters, and other devices [7, 18, 19]. There have been recent applications of PDLCs involving phase separation induced from rapid temperature quenching [20, 21, 22, 23, 24, 25, 26, 27, 28].

In order to better control and design the properties of these materials, it is crucial to understand the phase separation process and the ultimate morphologies. Due to the complexity of physical models used for phase separation, it is necessary to resort to numerical simulations for a systematic study. In this work, we report a computational investigation of the nucleation mechanism of a polymer in a LC continuous phase in a 2D and a 3D channel with the following setup as shown in Fig. 1.1: the polymer-LC system is confined between two parallel walls which provide strong planar long-range wall anchoring, and rapid temperature quenching induces the nucleation of the minority phase.

In earlier studies, a phase field model with a vector order parameter $\boldsymbol{n}$ has been widely employed for these binary systems [2, 3, 29]. However, a vector does not have head-to-tail symmetry and is incapable to learn biaxial states nor capture line defects. To better describe the domain anisotropy, our framework employs the more comprehensive Landau-de Gennes model which applies a tensor order parameter Q to describe the orientation of the rigid-rod like liquid crystal molecules. The free energy of the system is then formulated with the conserved volume fraction of the species and the non-conserved tensor order parameter. The evolution of the system is governed by the coupled time-dependent Ginzburg-Landau equations (model C) [30, 31]. Similar models have been
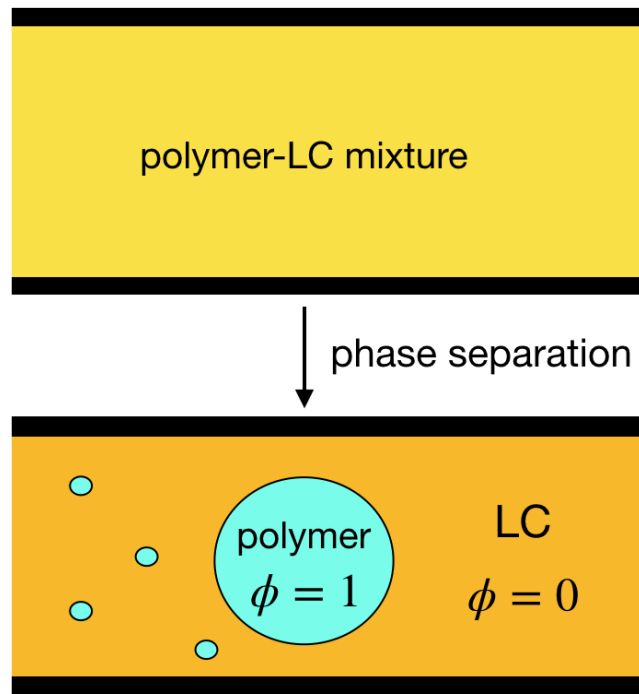
Figure 1.1: The polymer-LC system is confined between two parallel walls which provide strong planar long-range wall anchoring, and rapid temperature quenching induces the nucleation of the minority polymer phase. ϕ represents the volume fraction of isotropic polymer, with $\phi = 1$ and $\phi = 0$ represent the pure polymer phase and LC phase, respectively.

extensively used in phase separation with some degree of simplification [4, 5, 6, 12, 13, 14, 15]. To the best of our knowledge, this is the first time the full model has been utilized to learn the phase separation in confined geometries for a 3D geometry.

The Landau-de Gennes model poses significant numerical challenges. It is a large, highly nonlinear, and coupled system with up to fourth order derivative terms in the compositional order parameter ϕ, and several second order terms in the tensor order parameter Q equations. This makes the time integration markedly stiff. In addition, Q must remain traceless at each time step, and to preserve the integral of ϕ and be consistent with the variation of the free energy, a nontrivial boundary condition has to be enforced at the walls. We overcome these computational challenges with the implementation of a linearly implicit method, a strict enforcement of the traceless condition, and an extrapolated boundary condition.

We find that the nematic component has profound effect on structure formation. By varying thermotropic parameters which control the isotropic to nematic transition temperature of the LC in the presence of the polymer component, we are able to select the initial state of the LC to be nematic or isotropic and this leads to two strikingly different results. In one case, small polymer-rich droplets nucleate in a LC continuous phase and form ordered chain structures, layer by layer, in the early phase separation process in 2D, and cylindrical chain structures in 3D. The colloidal dispersions and emulsions of this type have attracted considerable attention because of the striking self-assembly morphologies [32, 33, 34, 35, 36, 37, 38], which offer great potential applications [39, 40]. The colloidal particles disturb the orientational field and produce defects which stabilize droplet chain structures. Theoretical [41] and numerical [42] studies on nematic liquid crystal colloids indicate that a dipole configuration which is characterized by a -1 point defect produced in between the droplets stabilize the chain. With the Landau-de Gennes model we are able to observe these chain structures, starting at the walls and propagating

into the interior, during a first stage in the phase separation process. However, as we show with one example, the -1 point defect are not preserved in the Landau-de Gennes model and split into $-1/2$ point defects in 2D and $-1/2$ disclination ring in 3D, which destroy the dipole and forms quadrupole. As a result, without the presence of dipole defects, the chain order is ultimately destroyed by coarsening and coalescence.

In a second study case, we consider a mixture in which the LC is initially in isotropic state. We find that the system phase separates into stable equilibrium lamellae, with alternating polymer-rich and LC-rich layers filling the entire region for both the 2D and 3D channel and when either homeotropic or planar surface anchoring conditions prevail.

The remainder of the dissertation is organized as follows. Chapter 2 describes the theoretical background and Landau-de Gennes modeling, Chapter 3 discusses the kinetic equation, the boundary conditions and the numerical scheme employed to solve the equations. Chapter 4 presents a summary of numerical results for 2D simulation and Chapter 5 presents 3D simulation.

Chapter 2

Theoretical Background

2.1 Introduction

In this Chapter, we present the theoretical background to study the nucleation of minority phase in the polymer-LC system. With a binary mixture of different species, we apply the Flory-Huggins theory to model the mixing free energy of our system.

In the continuum theories to study nematic liquid crystals, the microstructure of the material is described by functions taking values in an order parameter space. The choice of order parameters varies between models. In the Oseen-Frank theory, the unit vector order parameter $\boldsymbol{n}(x)$ is used, which is referred as the director that representing the mean orientation of the rigid-rod like molecules at point x. In its simplest form, the Oseen-Frank free energy functional reads

$$F_{OF}(\boldsymbol{n}) = \int_{\Omega} |\nabla \boldsymbol{n}(x)|^2 dx. \tag{2.1}$$

The Oseen-Frank model has several deficiencies in describing nematic liquid crystals. Firstly, the unit vector has no head-to-tail symmetry, and $\boldsymbol{n}$ and $-\boldsymbol{n}$ are treated as

discontinuity while physically they should be equivalent. In addition, the molecular order is assumed uniaxial and puts a limit in the theory to learn biaxial states. Lastly, it only accounts for point defects in 3D, and is incapable to capture the 2D point defects or line defects, which are observed in real experiments. These defects possess infinity energy in the Oseen-Frank theory.

A more comprehensive model is the continuum Ericksen theory, which is also restricted to uniaxial liquid crystal as Oseen-Frank theory, however, it incorporates the scalar order parameter S, which measures the degree of orientation of the molecules. The state of liquid crystal is then described by a pair $(S, \boldsymbol{n})$. With the capability to study the spatially variation of orientational order, this energy can describe all physically observable defects [43].

The most general continuum model is the Landau-de Gennes theory which can account for both uniaxial and biaxial phases and learn all types of defects [1]. Landau-de Gennes theory involves a tensor order parameter Q, which is a traceless symmetric 3×3 matrice, and describes the orientational probability distribution of the molecules.

In the following sections, the theoretical background based on Laudau-de Gennes model [44] are presented. To study the thermodynamic introduced by temperature quenching, the thermotropic energy that describes the phase transition of nematic liquid crystal, and the distortional energy imposed by the deformation of director field are considered in the bulk energy. To account for the anchoring effect induced by the confined walls and the interface of the particles, the surface anchoring energy that penalize the preferred orientation at the surface is included. These are used as central elements in mathematical model in the next Chapter.

2.2   Free Energy of Mixing

Since we have a mixture of two different species, we need to consider the mixing free energy of our system. The general theory for modeling the mixing free energy is the Flory-Huggins theory, which was independently derived by Flory [45] and Huggins [46].

The free mixing energy that governing mixtures of dissimilar component is

$$\Delta G_m = \Delta H_m - T\Delta S_m, \tag{2.2}$$

where ΔG_m is the Gibbs free energy, ΔH_m is the enthaply of mixing, ΔS_m is the entropy of mixing, and T is the temperature.

Let N_p and N_l be the number of the isotropic polymer and nematic liquid crystal molecules, let V_p and V_l be the volume that are occupied by each isotropic and liquid crystal molecule, respectively. The total volume of lattice sites of our system is given by $V = V_l N_l + V_p N_p$. Therefore, the volume fraction of isotropic polymer is $\phi = \dfrac{V_p N_p}{N}$, and the volume fraction of the liquid crystal is $1 - \phi$.

Based on Boltzmann relationship, the entropy of mixing for mixtures of dissimilar components reads

$$\Delta S_m = k_B \ln \Omega, \tag{2.3}$$

where $\Omega = \dfrac{(N_l + N_p)!}{N_l! N_p!}$ represents summation of combinations of arranging N_l and N_p molecules into a regular lattice of $N_L + N_p$ cells, and k_B is the Boltzmann constant. Apply Sterling's approximation,

$$\ln(N!) = N \ln N - N + O(\ln N), \tag{2.4}$$

this yields,

$$\Delta S_m = -k_B(N_p \ln(\frac{N_p}{N_l + N_p}) + N_l \ln(\frac{N_l}{N_l + N_p})). \tag{2.5}$$

In reality, the mole fraction was replaced by volume fraction to yield agreement with the experimental observations,

$$\Delta S_m = -k_B(N_p \ln \phi + N_l \ln(1 - \phi)) = -k_B V(\frac{\phi}{V_p} \ln \phi + \frac{1 - \phi}{V_l} \ln(1 - \phi)). \tag{2.6}$$

The enthaply of the mixture reads

$$\Delta H_m = k_B T V \chi \phi (1 - \phi), \tag{2.7}$$

where χ is Flory-Huggins interaction parameter related to the isotropic van der Waals interactions between unlike molecular species. The temperature dependence of χ has often been expressed $\chi = a + b/T$.

Combining the equations above, we get

$$\frac{\Delta G_m}{k_B T V} = \frac{\phi}{V_p} \ln \phi + \frac{1 - \phi}{V_l} \ln(1 - \phi) + \chi \phi (1 - \phi). \tag{2.8}$$

Our aim here is to understand how the phase separation between two difference phases occurs in a quenching experiment. There will be macroscopic regions of pure isotropic fluid and pure nematic liquid crystal, separated by an interfacial layer. This can be studied through an extension of the Flory-Huggins theory, allowing for spatial variations of volume fraction ϕ. The extended equation reads

$$\frac{\Delta G_m}{k_B T V} = \frac{c^2 (\nabla \phi)^2}{2} + \frac{\phi}{V_p} \ln \phi + \frac{1 - \phi}{V_l} \ln(1 - \phi) + \chi \phi (1 - \phi), \tag{2.9}$$

where the first term represents the conformational entropy of the polymer chains, and c

9

is related with the interfacial thickness [47]. Note that one could use a more appropriate Lifshitz-deGennes term $\frac{c^2(\nabla\phi)^2}{\phi(1-\phi)}$ instead of the gradient square term [47, 48], this will complicate the numerical simulation but essentially leads to the same results [11].

Based on the above discussion, we formulate the mixing free energy as

$$f_{mix}(\phi) = \frac{\lambda}{2}[(\nabla\phi)^2 + \frac{\beta\phi\ln\phi + (1-\phi)\ln(1-\phi) + \frac{g_0}{T}\phi(1-\phi)}{2\epsilon^2}], \qquad (2.10)$$

where λ is the mixing energy strength with units of J/m and ϵ is the capillary width with units of length. $\beta = \frac{V_l}{V_p}$ denotes the molecular volume ratio of liquid crystal and isotropic polymer. The coefficient $\frac{g_0}{T}$ is the interaction parameter related to the isotropic van der Waals interactions between unlike molecular species, where T is the temperature.

2.3   Nematic Order Parameter

As mentioned above, the director $\boldsymbol{n}$ is used to described the average molecular orientation of nematic molecules. We use $\boldsymbol{n}(r,t)$ to account for the spatial and temporal variations, and $\boldsymbol{n}(r,t)$ is physically equivalent with $-\boldsymbol{n}(r,t)$.

By inducing thermal fluctuations, the rod-like molecules are generally skewed off the direction, and the phase of the nematic liquid crystal may vary. At high temperatures, the axes for the liquid crystal molecules orients randomly which results in the isotropic phase. When it cools down, the nematic phase with anisotropy appears. The distinction between the isotropic phase and the nematic phase is due to the extent of orientational ordering of the molecules $\boldsymbol{u}$ around the averaged director $\boldsymbol{n}$, which can be quantified by the scalar order parameter S. To be precise, S is the ensemble average of the second Legendre polynomials of the scalar product between molecular direction $\boldsymbol{u}$ and the average direction $\boldsymbol{n}$ [44].

Let us consider a coordinate system with the director $\boldsymbol{n}$ parallel to z axis, i.e., $\boldsymbol{n} = (0, 0, 1)$, and the orientation of each individual molecule is characterized by the unit vector $\boldsymbol{u}$. Let θ_m and ϕ_m denote the angular deviations of the molecule along the polar and azimuthal directions, respectively. As a result, $\boldsymbol{u}$ can be parameterized as

$$\boldsymbol{u} = (\sin(\theta_m)\cos(\phi_m), \sin(\theta_m)\sin(\phi_m), \cos(\theta_m)), \tag{2.11}$$

therefore the scalar product $\boldsymbol{n} \cdot \boldsymbol{u} = \cos(\theta_m)$.

Let $f(\theta_m, \phi_m)$ be the orientation distribution function of finding a molecule with orientation angle θ_m and ϕ_m. For uniaxial nematic, $f(\theta_m, \phi) = f(\theta_m)$ because of axially symmetry. We can expand $f(\theta_m)$ with Legendre polynomials of the scalar product between $\boldsymbol{u}$ and $\boldsymbol{n}$,

$$f(\theta_m) = \sum_{k=0}^{\infty} f_k P_k(\cos(\theta_m)), \tag{2.12}$$

where $P_k(x)$ is the k-th Legendre polynomial, and

$$f_k = \frac{2k+1}{2} \int_{-1}^{1} f(\theta_m) P_k(\cos(\theta_m)) d(\cos(\theta_m)). \tag{2.13}$$

Because of the head-to-tail symmetry, $\boldsymbol{u}$ and $-\boldsymbol{u}$ are equivalent and thus $f(\theta_m) = f(\pi - \theta_m)$. Hence, the odd terms of f_k vanishes, and $f_0 = 1$ does not convey orientation information. The scalar order parameter is then defined by the first non-zero and orientation sensitive expansion term f_2,

$$S = \frac{1}{5}f_2 = \frac{1}{2} \int_{-1}^{1} f(\theta_m) P_2(\cos(\theta_m)) d(\cos(\theta_m)) = \frac{3}{2} < \cos^2(\theta_m) - \frac{1}{3} > . \tag{2.14}$$

The values of S lie in the interval $[-1/2,\ 1]$, and the values can be interpreted as follow: $S = 1$ corresponds to a perfect nematic order with all molecules orient exactly

11

along the director $\boldsymbol{n}$, $S = 0$ characterizes an isotropic state where molecules have no preferential direction, and $S = -1/2$ indicates that all molecules order along a plane perpendicular to $\boldsymbol{n}$. At room temperature, $S \sim 0.5 - 0.6$ in typical nematic like 5CB [49].

A uniaxial tensor order parameter Q can be obtained by combining the director $\boldsymbol{n}$ and scalar order parameter S. Consider the orientational distribution function up to the second order,

$$
\begin{aligned}
f(\theta_m) &= 1 + f_2 P_2(\cos(\theta_m)) \\
&= 1 + \frac{5}{2} S_2 (3(\boldsymbol{nu})^2 - 1) \\
&= 1 + \frac{15}{2} S(n_i n_j - \frac{1}{3}\delta_{ij}) u_i u_j \\
&= 1 + \frac{15}{2} Q_{ij}^U u_i u_j.
\end{aligned}
\tag{2.15}
$$

Here i, j denote the summation over the repeated indices, and δ_{ij} is the Kronecker delta. The uniaxial tensor order parameter is defined as

$$
Q^U = S(\boldsymbol{n} \otimes \boldsymbol{n} - \frac{1}{3}\boldsymbol{I}).
\tag{2.16}
$$

The largest eigenvalue of Q^U is $2S/3$ with the director $\boldsymbol{n}$ as the corresponding eigenvector, and the other two eigenvalues are $-S/2$ with eigenvectors perpendicular to $\boldsymbol{n}$.

For the rod-like molecules, it may form uniaxial or biaxial configuration, as shown in Fig. 2.1. The fundamental principle of a biaxial system is that it has no axes of rotational symmetry, i.e, no axis about which that a rotation of any angle keeps the system unchanged. In contrast, the uniaxial liquid crystal has rotational symmetry around its director $\boldsymbol{n}$. Typically, the nematic liquid crystal material exists in a uniaxial phase in the bulk when below the nematic-isotropic transition temperature, and biaxial state may occur near the confining surfaces or in the vicinity of defects. In order to
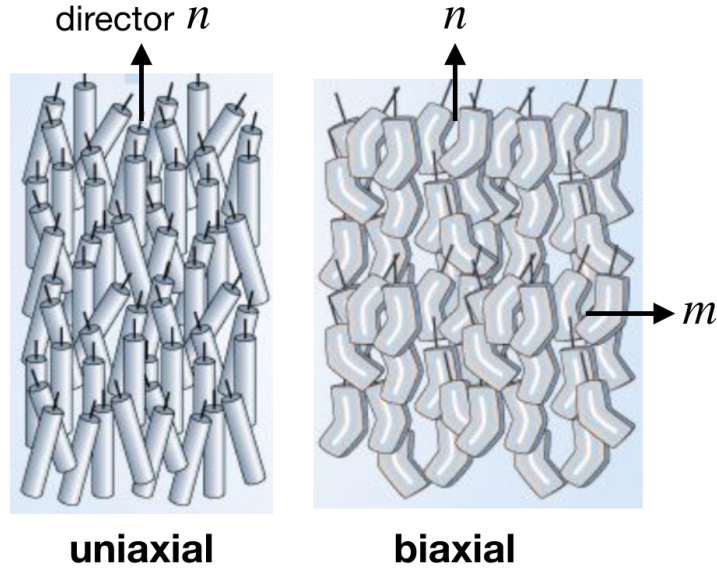
Figure 2.1: Uniaxial and biaxial state for rig rod-like molecules.

describe the biaxial state, it requires two unit vector variables, $\boldsymbol{n}(x,t)$ and $\boldsymbol{m}(x,t)$, and two scalar order parameter, $S_1(x,t)$ and $S_2(x,t)$, all depend on the spatial and temporal variations. The more general form of Q reads

$$Q = S_1(\boldsymbol{n} \otimes \boldsymbol{n}) + S_2(\boldsymbol{m} \otimes \boldsymbol{m}) - \frac{1}{3}(S_1 + S_2)\boldsymbol{I}, \tag{2.17}$$

which is a 3×3 symmetric traceless matrix, and only five of the nine components are independent. This gives three spatial degrees of freedom and two orientational degrees of freedom. The three eigenvalues are a measure of nematic orientational order along the three orthogonal directions denoted by the corresponding eigenvector.

The eigenvalues of the matrix Q are

$$\lambda_1 = (2S_1 - S_2)/3,$$
$$\lambda_2 = (2S_2 - S_1)/3, \tag{2.18}$$
$$\lambda_3 = -(S_1 + S_2)/3.$$

When all the eigenvalues are the same, the system is isotropic, and $S_1 = S_2 = 0$, so that $Q = \mathbf{0}$. When all the eigenvalues are different, it is the biaxial state. Uniaxial states exist when two of these eigenvalues are the same, i.e., $S_1 = 0$ or $S_2 = 0$ or $S_1 = S_2$.

As mentioned by Majumdar et al. in [43], Q can also be equivalently expressed as

$$Q = S(\boldsymbol{n} \otimes \boldsymbol{n} - \frac{1}{3}\boldsymbol{I}) + R(\boldsymbol{m} \otimes \boldsymbol{m} - \boldsymbol{p} \otimes \boldsymbol{p}), \tag{2.19}$$

where $\boldsymbol{n}$, $\boldsymbol{m}$ and $\boldsymbol{p}$ are unit vectors and pairwise perpendicular eigenvectors of Q, and S, R are given by $S = S_1 - \dfrac{S_2}{2}, R = \dfrac{S_2}{2}$. This can be derived by the fact that

$$\boldsymbol{I} = \boldsymbol{n} \otimes \boldsymbol{n} + \boldsymbol{m} \otimes \boldsymbol{m} + \boldsymbol{p} \otimes \boldsymbol{p}, \tag{2.20}$$

with which (2.17) and (2.19) both equal to

$$Q = \frac{2S_1 - S_2}{3}\boldsymbol{n} \otimes \boldsymbol{n} + \frac{2S_2 - S_1}{3}\boldsymbol{m} \otimes \boldsymbol{m} - \frac{S_1 + S_2}{3}\boldsymbol{p} \otimes \boldsymbol{p}. \tag{2.21}$$

This is the spectral decomposition of Q and indicates that the pairwise perpendicular eigenvector $\boldsymbol{n}, \boldsymbol{m}, \boldsymbol{p}$ corresponds to the eigenvalues λ_1, λ_2, λ_3 in Eq. (2.18).

The biaxiality parameter in the liquid crystal literature is usually defined as [50, 43]

$$\beta(Q) = 1 - 6\frac{(tr(Q^3))^2}{(tr(Q^2))^3}, \tag{2.22}$$

where $\beta(Q) \in [0, 1]$, and $\beta(Q) = 0$ stands for the uniaxial case. We present a simple
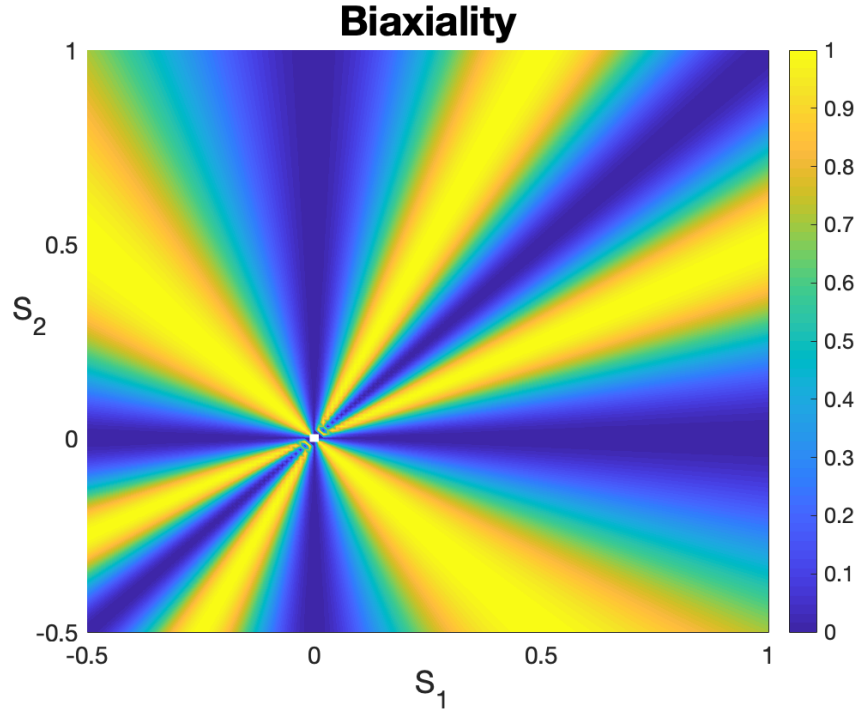
Figure 2.2: The relationship between the biaxiality parameter $\beta(Q)$ and the order parameters S_1 and S_2. $\beta(Q) = 0$ as $S_1 = 0$, $S_2 = 0$ or $S_1 = S_2$.

proof here. Apply Eq. (2.18),

$$
\begin{aligned}
trQ^3 &= \sum_{i=1}^{3} \lambda_i^3 = \frac{1}{9}(2S_1^3 + 2S_2^3 - 3S_1^2 S_2 - 3S_1 S_2^2), \\
trQ^2 &= \sum_{i=1}^{3} \lambda_i^2 = \frac{2}{3}(S_1^2 + S_2^2 - S_1 S_2),
\end{aligned}
\tag{2.23}
$$

which implies,

$$
(trQ^2)^3 - 6(trQ^3)^2 = 2S_1^2 S_2^2 (S_1 - S_2)^2 >= 0.
\tag{2.24}
$$

It follows immediately that $\beta(Q) \in [0, 1]$, and $\beta(Q) = 0$ iff either $S_1 = 0$, $S_2 = 0$ or $S_1 = S_2$, all correspond to uniaxial nematic states. The relationship between $\beta(Q)$ and the order parameter S_1, S_2 is shown in Fig. 2.2.

15

2.4   Landau-de Gennes Model

2.4.1   Phase Transition

For most liquid crystal materials, the stability of the nematic phase depends either on the temperature or the concentration of the molecules. In this work, we are interested in the phase separation driven by abrupt temperature change, and the thermotropic potential determines whether the liquid crystal is at isotropic or nematic phase. Phase transition is usually classified into first order and second order continuous transitions. First-order transition is characterized by the discontinuities in the first derivatives of the thermodynamic potential. In the nematic to isotropic (NI) phase transition, it has been observed experimentally that the order parameter S abruptly decreases from $0.25 \sim 0.5$ to zero at transition temperature, and discontinuities have also been found in the density and heat contents, which indicates a first order transition. Consequently, the potential shall be eligible to describe the first order transition. In addition, it needs to attain a minimum in the isotropic state at high temperature, whereas at low temperature the minimums exist at three uniaxial nematic states. The simplest form of such a function is a truncated Taylor expansion about $Q = \mathbf{0}$, which reads

$$f_{ther} = \frac{A}{2} Tr Q^2 + \frac{B}{3} Tr Q^3 + \frac{C}{4} (Tr Q^2)^2.$$ (2.25)

The coefficients A, B, C are in general temperature and material dependent, although it is usual to assume that B and C are independent of temperature whereas $A = a(T - T_{NI}^*)$, and T_{NI}^* is the super-cooling temperature at which the isotropic state becomes unstable. Therefore, it is the first term which drives the phase transition as temperature changes. The constant parameters $a > 0, B < 0, C > 0$, and typical values of a, B, and C are of the orders of $10^5 J/m^3 K, 10^6 J/m^3$, and $10^6 J/m^3$, respectively [44]. The NI

16

transition temperature for the 5CB material is $308.4K$ [49], but can vary dramatically for different materials.

Proposition: The set of Q which minimizing the thermotropic energy f_{ther} clearly plays a crucial role, and we claim that this set consists of uniaxial Q, i.e., Q shall be of the form $Q = S(\boldsymbol{n} \otimes \boldsymbol{n} - \frac{1}{3}\boldsymbol{I})$.

Proof: We prove it by contradiction. Assume Q is uniaxial, i.e., all three eigenvalues are distinct from each other. By applying $trQ^n = \sum_{i=1}^{3} \lambda_i^n$, the thermotropic potential can be rewritten as a function of λ_i,

$$
\begin{aligned}
f_{ther} &= \frac{A}{2}TrQ^2 + \frac{B}{3}TrQ^3 + \frac{C}{4}(TrQ^2)^2 \\
&= \frac{A}{2}\sum_{i=1}^{3}\lambda_i^2 + \frac{B}{3}\sum_{i=1}^{3}\lambda_i^3 + \frac{C}{4}(\sum_{i=1}^{3}\lambda_i^2)^2.
\end{aligned}
\tag{2.26}
$$

Tensor Q needs to be traceless, which indicates $\sum_{i=1}^{3}\lambda_i = 0$. Therefore, we can consider the Lagrange multiplier to find the minimum of f_{ther} subject to traceless condition, and the minimizer is defined by the equilibrium points of the following function,

$$
g(\lambda_1, \lambda_2, \lambda_3) = \frac{A}{2}\sum_{i=1}^{3}\lambda_i^2 + \frac{B}{3}\sum_{i=1}^{3}\lambda_i^3 + \frac{C}{4}(\sum_{i=1}^{3}\lambda_i^2)^2 - 2\eta\sum_{i=1}^{3}\lambda_i.
\tag{2.27}
$$

The equilibrium is given by a system of three equations $\frac{\partial g}{\partial \lambda_i} = 0$, which is

$$
A\lambda_i + B\lambda_i^2 + C\sum_{k=1}^{3}\lambda_k^2\lambda_i = \eta, \quad 1 \le i \le j \le 3,
\tag{2.28}
$$

or equivalently,

$$
(\lambda_i - \lambda_j)[A + B(\lambda_i + \lambda_j) + C\sum_{k=1}^{3}\lambda_k^2 = 0, \quad 1 \le i \le j \le 3.
\tag{2.29}
$$

Since all three eigenvalues are different, this indicates

$$A + B(\lambda_1 + \lambda_2) + C\sum_{k=1}^{3}\lambda_k^2 = 0,$$
$$A + B(\lambda_1 + \lambda_3) + C\sum_{k=1}^{3}\lambda_k^2 = 0.$$

(2.30)

Subtracting these two equations yields $B(\lambda_2 - \lambda_3) = 0$, which contradicts with our assumption that $\lambda_2 \neq \lambda_3$. Therefore, the equilibrium solution of the thermotropic potential f_{ther} must have at least two eigenvlaues equal and therefore corresponds to either a uniaxial or isotropic phase, which ends the proof. □

We consider a uniaxial state with $S_1 = S,\ S_2 = 0$, which makes $\lambda_2 = \lambda_3$, and the corresponding tensor $Q = S(\boldsymbol{n} \otimes \boldsymbol{n} - \dfrac{1}{3}\boldsymbol{I})$. Apply the eigenvalues information in (2.18), we can rewrite the potential f_{ther} as a function of scalar order parameter,

$$\begin{aligned}
f_{ther} &= \frac{A}{2}TrQ^2 + \frac{B}{3}TrQ^3 + \frac{C}{4}(TrQ^2)^2\\
&= \frac{A}{2}\sum_{i=1}^{3}\lambda_i^2 + \frac{B}{3}\sum_{i=1}^{3}\lambda_i^3 + \frac{C}{4}(\sum_{i=1}^{3}\lambda_i^2)^2\\
&= \frac{1}{27}(9a(T - T_{NI}^*) + 2BS + 3CS^2)S^2.
\end{aligned}$$

(2.31)

The terms can be interpreted this way, the first temperature dependent term drives the phase transition, the second term ensures the asymmetry of S by breaking the S to $-S$ invariance, ant the third term provides the lower bound of S.

We are interested in the equilibrium state of f_{ther} with a given temperature, and we find

$$\begin{aligned}
f_{ther}' &= \frac{2}{9}(3A + BS + 2CS^2)S,\\
f_{ther}'' &= \frac{2}{9}(3A + 2BS + 6CS^2).
\end{aligned}$$

(2.32)

18
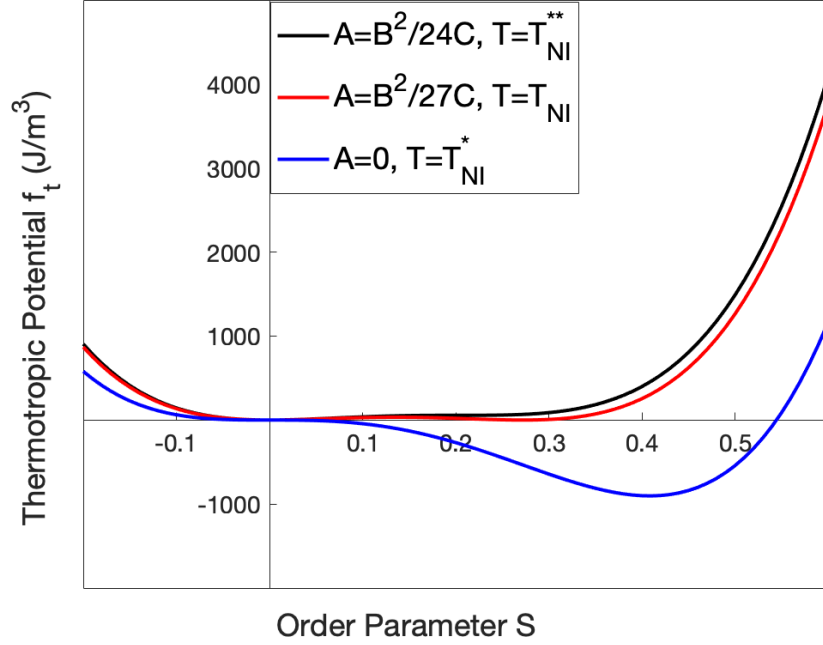
Figure 2.3: Relationship between thermotropic free energy f_{ther} with the order parameter S. The curves correspond to three special temperatures: super-heating temperature T_{NI}^{**}, NI transition temperature T_{NI}, and super-cooling temperature T_{NI}^{*}. For illustration we use $B = -0.7155 \times 10^6 \, J/m^3$, $C = 0.8758 \times 10^6 \, J/m^3$.

By applying these information, the three stationary points are 0, $\dfrac{-B \pm \sqrt{B^2 - 24AC}}{4C}$. The point $\dfrac{-B - \sqrt{B^2 - 24AC}}{4C}$ corresponds to a local maximum, and thus we are only interested in $S = 0$ and $S = \dfrac{-B + \sqrt{B^2 - 24AC}}{4C}$, which corresponds to the isotropic and uniaxial nematic state, respectively.

Fig. 2.3 illustrates the dependence of f_{ther} on S with three special cases as $A = \dfrac{B^2}{24C}, \dfrac{B^2}{27C}, 0$. The interpretation is as follows,

- As $A > \dfrac{B^2}{27C}$, the isotropic state $S = 0$ is globally stable with a global minimal energy, and the nematic state $S = \dfrac{-B + \sqrt{B^2 - 24AC}}{4C}$ is metastable with a local minimum for $\dfrac{B^2}{27C} < A < \dfrac{B^2}{24C}$, and undefined for $A > \dfrac{B^2}{24C}$.

- As $A = \dfrac{B^2}{27C}$, the free energy of the isotropic state and nematic state are equal, as shown by the red line in the Figure.

- As $A < \dfrac{B^2}{27C}$, the nematic state is globally stable with a global minimal energy, and the isotropic state is metastable with a local minimal for $A > 0$, and unstable for $A < 0$.

The corresponding temperatures of the curves in Figure 2.3 are as follows,

- The high temperature T_{NI}^{**} where the nematic state disappears, which is called super-heating temperature,

$$T_{NI}^{**} = T_{NI}^* + \frac{B^2}{24aC}. \tag{2.33}$$

- The temperature T_{NI} at which the energy of isotropic state and nematic state are equal, which is called the nematic-isotropic transition temperature,

$$T_{NI} = T_{NI}^* + \frac{B^2}{27aC}. \tag{2.34}$$

- The low temperature T_{NI}^* at which the isotropic state loses stability, which is called super-cooling temperature. Theoretically the isotropic can be cooled to this temperature.

The expression of f_{ther} is essentially a Taylor expansion about $Q = \mathbf{0}$, therefore the Landau-de Gennes theory is only valid near the nematic-isotropic transition temperature T_{NI}, where $Q \approx \mathbf{0}$. Based on what is stated above, we can define the equilibrium S_{eq} as follows,

$$S_{eq} = \begin{cases} 0 & T > T_{NI}, \\ \dfrac{1}{4C}(-B + \sqrt{B^2 - 24a(T - T_{NI}^*)C}) & T < T_{NI}. \end{cases} \tag{2.35}$$

20
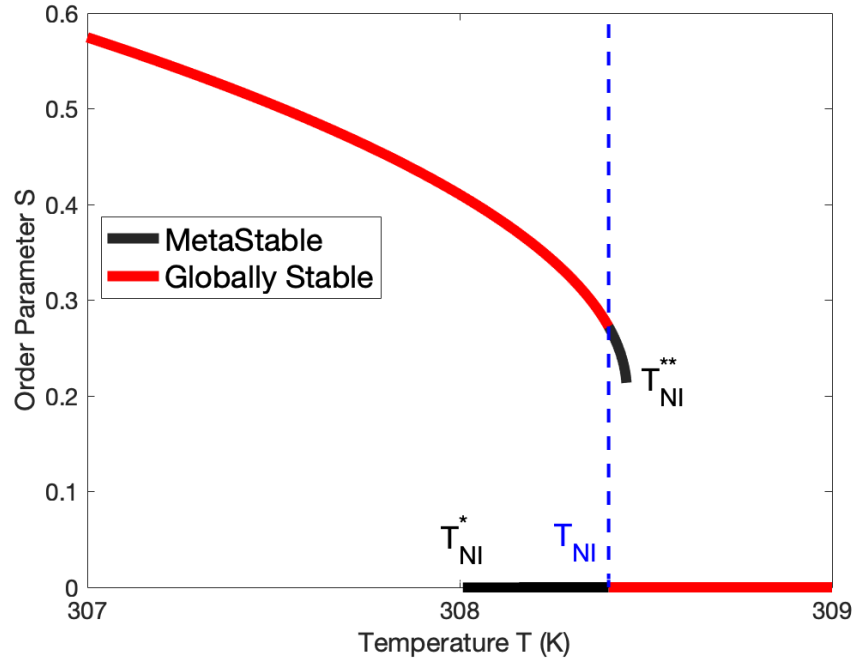
Figure 2.4: The equilibrium nematic order parameter S as a function of temperature T. The NI transition temperature shown here is $T_{NI} = 308.4K$ for nematic 5CB, and $a = 0.553 \times 10^5 J/m^3 K$, $B = -0.7155 \times 10^6 J/m^3$, $C = 0.8758 \times 10^6 J/m^3$. This gives $T_{NI}^* = 308.0085K$, and $T_{NI}^* = 308.4489K$.

Fig. 2.4 shows the variation of the S_{eq} as a function of the temperature T. At the nematic-isotropic transition temperature T_{NI}, S_{eq} undergoes a first order discontinuous transition.

2.4.2   Nematic Elasticity

In an ideal nematic phase, the molecules are averagely aligned along the director $\boldsymbol{n}$. However, in most practical circumstances, there will be some deformation of the alignment imposed by the confined surfaces and the electric or magnetic external fields acting on the molecules, etc. The distorted state may then be described entirely on the vector order parameter field $\boldsymbol{n}(r)$, and the typical deformation is one or a combination of three basic modes: splay, twist and bend [51], as shown in Fig. 2.5.

21
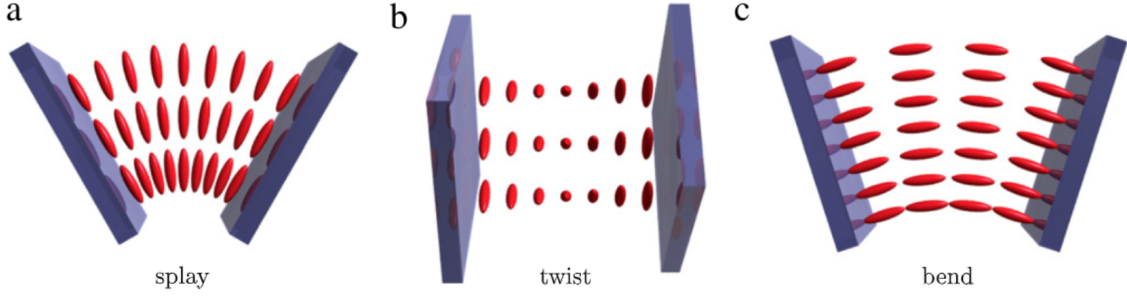
Figure 2.5: Three basic modes of the deformation of director field of nematic liquid crystal in confined geometry [53].

The spatial variation in the director field disturbs molecular packing and creates a free energy penalty. This type of description leads to the Oseen-Frank model, which provides a fundamental formula for the nematic continuum theory, and the elastic free energy density is

$$
\begin{aligned}
f_{ela}^{FO} =& \frac{1}{2}[K_1(\nabla \cdot \boldsymbol{n})^2 + K_2(\boldsymbol{n} \cdot (\nabla \times \boldsymbol{n}))^2 + K_3(\boldsymbol{n} \times (\nabla \times \boldsymbol{n}))^2 \\
& - (K_2 + K_4)\nabla \cdot (\boldsymbol{n}(\nabla \cdot \boldsymbol{n}) + \boldsymbol{n} \times (\nabla \times \boldsymbol{n}))],
\end{aligned}
\tag{2.36}
$$

where the first three terms accounts for the splay, twist and bend of the director field with corresponding Frank elastic constants $K_i \geq 0$ of units of J/m, and the last mixed coefficient $(K_2 + K_4)$ is called saddle-splay constant which gives spatial derivatives of the director within the surface plane. The last term is often omitted when the anchoring energy on the surface is sufficiently strong, since the integration of it adds only a constant and does not contribute to the bulk equilibrium configuration [52].

Based on the discussion in [54], the Frank-Oseen free energy density representation (2.36) can be rewritten into the Q tensor representation, which reads

$$
f_{ela}^{Q} = \frac{1}{2}L_1\frac{\partial Q_{ij}}{\partial x_k}\frac{\partial Q_{ij}}{\partial x_k} + \frac{1}{2}L_2\frac{\partial Q_{ij}}{\partial x_j}\frac{\partial Q_{ik}}{\partial x_k} + \frac{1}{2}L_3\frac{\partial Q_{ik}}{\partial x_j}\frac{\partial Q_{ij}}{\partial x_k} + \frac{1}{2}L_4Q_{lk}\frac{\partial Q_{ij}}{\partial x_l}\frac{\partial Q_{ij}}{\partial x_k}.
\tag{2.37}
$$

The elastic parameters L_i are related with K_i as

$$
\begin{aligned}
L_1 &= \frac{1}{6S^2}(K_3 - K_1 + 3K_2), \\
L_2 &= \frac{1}{S^2}(K_1 - K_2 - K_4), \\
L_3 &= \frac{1}{S^2}(K_4), \\
L_4 &= \frac{1}{2S^3}(K_3 - K_1),
\end{aligned}
\tag{2.38}
$$

where S is the order parameter of the liquid crystal when the experimental measurement of L_i was taken.

In practice, form (2.36) and (2.37) are too complex either because the values of the Frank elastic constants are unknown, or because the equations are difficult to solve. Further simplification is often applied by assuming the three elastic constants are equal, $K_1 = K_2 = K_3 = K$, and the coefficient $K_4 = 0$, which is referred as one constant approximation. This simplification reduces (2.36) into

$$
f_{ela}^{FO} = \frac{1}{2}K|\nabla \boldsymbol{n}|^2,
\tag{2.39}
$$

where $|\nabla \boldsymbol{n}|^2 = (\frac{\partial n_i}{\partial x_j})^2$. For the Q tensor representation form, (2.38) implies that $L_1 = \frac{K}{2S^2}$, $L_2 = 0$, $L_3 = 0$, $L_4 = 0$, and consequently (2.37) reduces to

$$
f_{ela}^{Q} = \frac{1}{2}L_1 \frac{\partial Q_{ij}}{\partial x_k}\frac{\partial Q_{ij}}{\partial x_k}.
\tag{2.40}
$$

For 5CB nematic, the splay, bend and twist elastic constants differ from the average elastic strength $K = 6 \times 10^{-12} J/m$ by around 40% [55].

Assume the nematic liquid crystal is uniaxial, i.e., $Q_{\alpha\beta} = S(n_\alpha n_\beta - \frac{1}{3}\delta_{\alpha\beta})$, we consider the spatial variation of both S and $\boldsymbol{n}$, and rewrite (2.40) in terms of variation in terms

of S and $\boldsymbol{n}$,

$$f_{ela}^Q = \frac{L_1}{2} \frac{\partial Q_{ij}}{\partial x_k} \frac{\partial Q_{ij}}{\partial x_k}$$

$$= \frac{L_1}{2} [\frac{\partial S}{\partial x_k}(n_i n_j - \frac{1}{3}\delta_{ij}) + S\frac{\partial(n_i n_j)}{\partial x_k}]^2 \tag{2.41}$$

$$= \frac{L_1}{2} [(\frac{\partial S}{\partial x_k})^2(n_i n_j - \frac{1}{3}\delta_{ij})^2 + 2S(\frac{\partial S}{\partial x_k})(n_i n_j - \frac{1}{3}\delta_{ij})\frac{\partial(n_i n_j)}{\partial x_k} + S^2(\frac{\partial(n_i n_j)}{\partial x_k})^2].$$

Since $n_i^2 = 1$, $n_i\frac{\partial n_i}{\partial x_k} = 0$, we have

$$(n_i n_j - \frac{1}{3}\delta_{ij})^2 = (n_i n_j)^2 - \frac{2}{3}n_i n_j \delta_{ij} + \frac{1}{9}\delta_{ij}^2 = \frac{2}{3},$$

$$(n_i n_j - \frac{1}{3}\delta_{ij})\frac{\partial(n_i n_j)}{\partial x_k} = 2(n_i n_j n_i \frac{\partial n_j}{\partial x_k} - \frac{1}{3}\delta_{ij}n_i \frac{\partial n_j}{\partial x_k}) = 0, \tag{2.42}$$

$$(\frac{\partial(n_i n_j)}{\partial x_k})^2 = 2n_i^2(\frac{\partial n_j}{\partial x_k})^2 + 2(n_i \frac{\partial n_i}{\partial x_k} n_j \frac{\partial n_j}{\partial x_k}) = 2(\frac{\partial n_j}{\partial x_k})^2 = 2|\nabla \boldsymbol{n}|^2.$$

This reduces (2.41) to

$$f_{ela}^Q = \frac{1}{3}L_1(\nabla S)^2 + L_1 S^2|\nabla \boldsymbol{n}|^2 = \frac{1}{3}L_1(\nabla S)^2 + \frac{1}{2}K|\nabla \boldsymbol{n}|^2, \tag{2.43}$$

which matches with (2.39) as S is a constant.

2.4.3   Bulk Free Energy

Consider the bulk free energy density f_{bulk} which contains the elastic free energy that penalizes the distortion of the director field, and the thermotropic free energy that describes the nematic order,

$$f_{bulk} = f_{ela} + f_{ther}. \tag{2.44}$$

Assume the variation of S only, and set $|\nabla \boldsymbol{n}| = 0$, then combining (2.31) and (2.43) yields

$$f_{bulk}(S, \nabla S) = \frac{1}{27}(9A + 2BS + 3CS^2)S^2 + \frac{1}{3}L(\nabla S)^2. \tag{2.45}$$

The minimizer of f_{bulk} obviously plays an important role. Consider the bulk free energy $F = \int_\Omega f_{bulk}(S, \nabla S)dV$ for the bulk domain Ω, then,

$$\delta F = \int_\Omega \frac{\partial f_{bulk}}{\partial S} \delta S dV + \int_\Omega \frac{\partial f_{bulk}}{\partial \nabla S} \nabla(\delta S) dV$$

$$= \int_\Omega (\frac{\partial f_{bulk}}{\partial S} - \nabla \cdot \frac{\partial f_{bulk}}{\partial \nabla S}) \delta S dV + \int_{\partial \Omega} \frac{\partial f_{bulk}}{\partial \nabla S} \cdot \delta S d\boldsymbol{s} \tag{2.46}$$

$$= 0.$$

This yields

$$\frac{\partial f_{bulk}}{\partial S} - \nabla \cdot \frac{\partial f_{bulk}}{\partial \nabla S} = 0. \tag{2.47}$$

Or equivalently,

$$\frac{\partial f_{bulk}}{\partial S} - \frac{2}{3}L\Delta S = 0. \tag{2.48}$$

The order parameter S shall be around S_{eq} that we introduced at (2.35). Therefore, we assume $S = S_{eq} + \delta S$ and thus,

$$\frac{\partial f_{bulk}}{\partial S} \approx \frac{\partial f_{bulk}}{\partial S}\Big|_{S_{eq}} + \frac{\partial^2 f_{bulk}}{\partial S^2}\Big|_{S_{eq}} \delta S = \frac{\partial^2 f_{bulk}}{\partial S^2}\Big|_{S_{eq}} \delta S, \tag{2.49}$$

which with (2.48) implies,

$$\frac{\delta S}{\Delta S} = \frac{2}{3}\frac{L}{(\partial^2 f_{bulk}/\partial S^2)|_{S_{eq}}} = \frac{L}{A + 2/3BS_{eq} + 2CS_{eq}^2}. \tag{2.50}$$

This ratio characterizes a length scale which measures the spatial scale of the variation

of the scalar order parameter S,

$$\xi_N = \sqrt{\frac{\delta S}{\Delta S}} = \sqrt{\frac{L}{a(T - T_{NI}^*) + 2/3BS_{eq} + 2CS_{eq}^2}}. \tag{2.51}$$

As illustrates in [42], ξ_N is referred as nematic correlation length, and it roughly determines the size of the defect in Landau de-Gennes model, which is generally at the order of a few nanometers. ξ_N will be used later to determine the mesh resolution in the numerical simulation.

2.4.4   Surface Anchoring

The surface of different materials such as fluid particles or glass slides affect the order of nematic liquid crystal by imposing a preferred molecular orientation. Such behavior is called anchoring. The usual types of anchoring are homeotropic (perpendicular) anchoring, and homogeneous (planar) with respect to the interface. The homeotropic anchoring is defined for which the molecules tend to align perpendicular to the interface, in contrast, the planar anchoring is preferred with tangential alignment, as shown in Fig. 2.6. The anchoring can usually be controlled by treating the surface in some way, for example, rubbing the surface in a fixed direction easily creates a strong homogeneous anchoring along the surface, and a suitable chemical detergent coating the surface tends to attach their polar head on the surface which imposes homeotropic anchoring [1].

For a liquid crystal system, the free energies in the bulk of nematic phase must be supplemented by the energy associated to the surface of the system. In practice, when strong anchoring is imposed, it introduces a well-defined direction to the director $\boldsymbol{n}$ at the surface, which provides a boundary condition with which the bulk energy terms only are minimized. However, in general there is a competition between the surface energy and the bulk energy, and their summation is minimized to reach the equilibrium. In
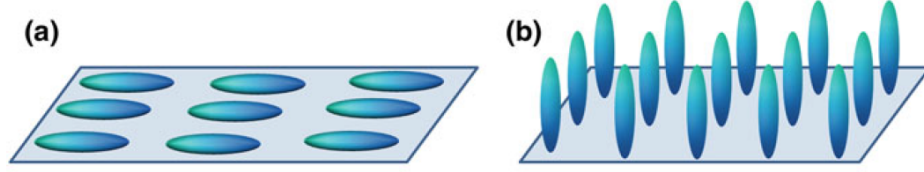
Figure 2.6: Surface anchoring of a nematic liquid crystal: (a) homogeneous, (b) homeotropic [44].

other words, the total free energy F in the nematic domain Ω with surface $\partial\Omega$ reads

$$F = \int_{\Omega} f_{bulk} dV + \int_{\partial\Omega} f_{sur} ds. \tag{2.52}$$

The surface free energy density being applied widely is the Rapini-Papoular type free energy

$$f_{sur}^{RP}(Q) = \frac{W}{2} tr(Q^S - Q)^2, \tag{2.53}$$

where $W > 0$ is the surface anchoring strength with units of J/m^2, and Q^S is the surface-preferred order parameter expressed as $Q^S = S_{eq}(\boldsymbol{n}^* \otimes \boldsymbol{n}^* - \frac{1}{3}I)$, where S_{eq} is the equilibrium order parameter defined as (2.35), and $\boldsymbol{n}^*$ is the preferred molecular alignment. Therefore, Q^S imposes the preferred director at the surface along with the equilibrium order parameter describes the degree of orientation. Typically, W is range from $10^{-3} J/m^2$ to $10^{-7} J/m^2$, where $10^{-3} \sim 10^{-4} J/m^2$ is strong anchoring and $10^{-6} \sim 10^{-7} J/m^2$ is weak [42]. As introduced in [51, 56], the ratio between elastic energy strength and anchoring energy strength also introduces a length scale to describe the strength of anchoring, namely the surface extrapolation length $\xi_S = K/W$. Assume there is an emulsion sphere particle with radius r in the nematic continuous phase, the characteristic energy specifying the interface anchoring and bulk elasticity are given by Wr^2 and Kr, respectively. Therefore, ξ_S approximates the size of the particle which balancing the

elastic energy with the surface anchoring energy. With $K \sim 10^{-11} J/m$, ξ_S has order of a few nanometers for surface possess strong anchoring $W \sim 10^{-3} J/m^2$, and it may go up to a few micrometers for weak anchoring $W \sim 10^{-6} J/m^2$.

As mentioned in [57], (2.53) is a special case of the more general surface anchoring energy strength

$$f_{sur} = W_{11}\boldsymbol{e} \cdot Q\boldsymbol{e} + W_{21}trQ^2 + W_{22}(\boldsymbol{e} \cdot Q\boldsymbol{e})^2 + W_{23}Q\boldsymbol{e} \cdot Q\boldsymbol{e}, \qquad (2.54)$$

where W_{ij} are the material dependent constants, and $\boldsymbol{e}$ is the preferred unit vector at the surface.

In our system, we have an isotropic material, like a polymer, nucleating in the nematic liquid crystal continuous phase induced from temperature quenching, which is characterized by a fast initial nucleation of small particles and subsequent slow growth and coarsening. Since numerous and uncontrolled particles appear, communicate and grow in the bulk, it is not practical to mark the interface $\partial\Omega$ and impose the boundary type energy (2.53). Instead, a volumetric anchoring energy is considered, which gives energy penalty primarily at the interface of the particles. Denote $\phi(r,t)$ as the volume fraction of the isotropic polymer that changes spatially and temporally, then the interface is the region where ϕ has a significant variation. In the light of (2.54), the preferred anchoring is specified by $\nabla\phi$, and the following volumetric anchoring free energy density is introduced for the particles [4, 6],

$$F_{sur}(Q) = \int_{\Omega} \frac{W_v}{2}(\nabla\phi) \cdot Q(\nabla\phi)dV = \int_{\Omega} \frac{W_v}{2}(\nabla_{\alpha}\phi)(\nabla_{\beta}\phi)Q_{\alpha\beta}dV, \qquad (2.55)$$

where W_v is the volumetric anchoring strength of unit J/m^3, and it specifies the orientation at the interface between polymer-rich phase and LC-rich phase: as $W_v < 0$,

the homeotropic anchoring is favorable, in contrast, as $W_v > 0$, the planar anchoring is preferred. Since W_v is volumetric, the surface extrapolation length ξ_S does not appear at this case.

2.5   Topological Defects

Defects in nematic liquid crystals are localized regions where the microstructure changes suddenly and creates striking patterns when passing polarized light. The presence of defects not only changes the physical properties in their vicinity, but also it is not energy favorable. Topological defects may be created between confined surfaces, under external fields or during symmetry breaking phase transitions.

Describing defects is a basic challenge in theoretical study of nematic liquid crystals. In the continuum theory, the microstructure of the material is described in the order-parameter space. In the Oseen-Frank model, the chosen order parameter is the unit director field $\boldsymbol{n}$, which measures the mean orientation of the molecules throughout the space, and defects correspond to discontinuities in $\boldsymbol{n}$. The discontinuity could occur as a point, line or on a surface, which are referred as point, line or sheet defects. The sheet defects are considered unstable since they tend to smear out into structures called walls and are omitted in the literature. The most common defects are then point and line defects. Line defects are usually called line disclinations, and point defect can be characterized by the number of times $\boldsymbol{n}$ rotates through 2π as an oriented circuit around the defect is traversed, which is called winding number. Fig. 2.7 shows the point defects associated with their appearance under crossed polarized light, and the defect locates at the place where the sudden change occurs.

One of the limitations of the Oseen-Frank model is that it only accounts for point defects in 3D, and point defect in 2D or line disclinations have infinity energy and failed
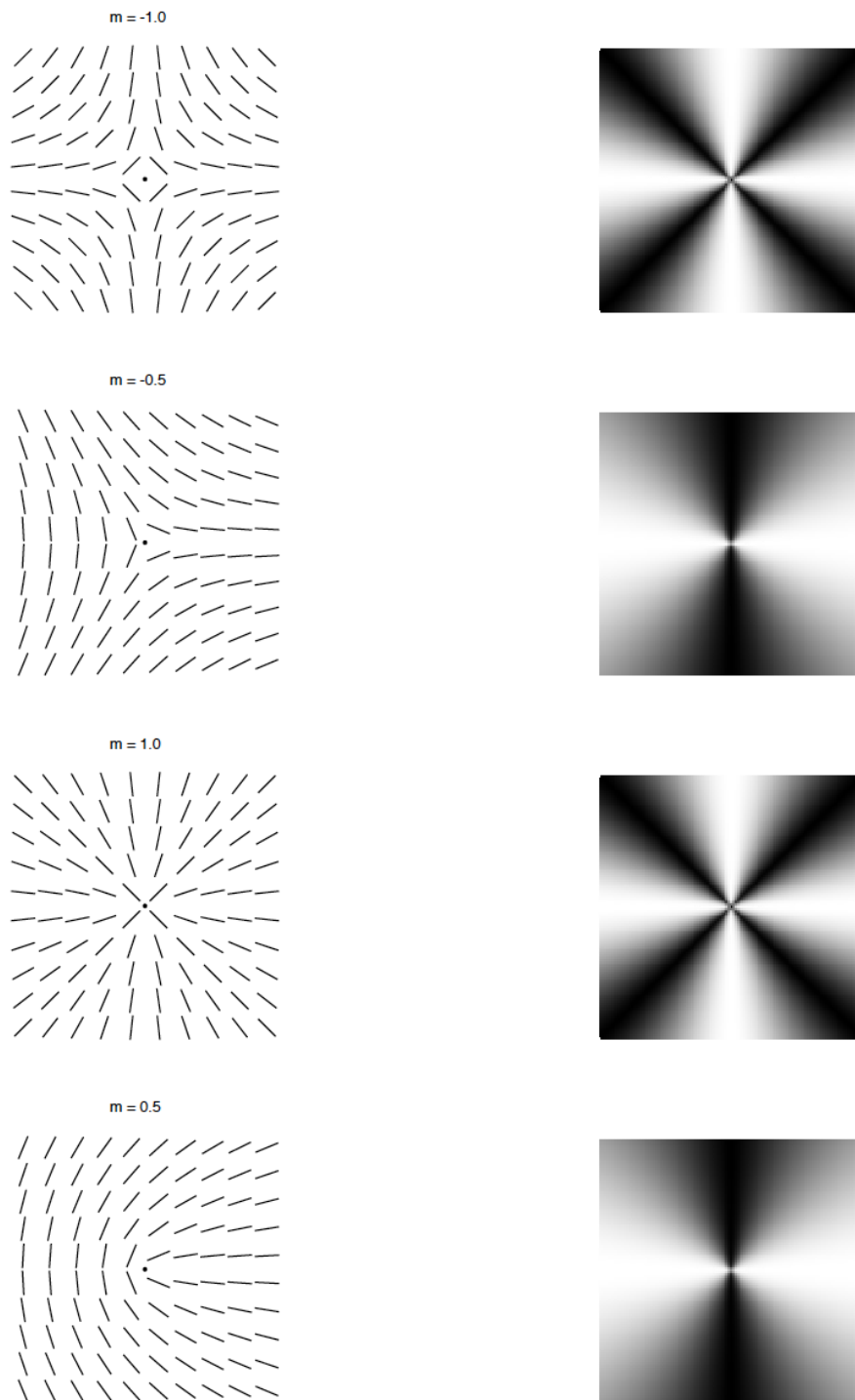
Figure 2.7: From top to bottom are director fields of the point defects (left) and the appearance under crossed polarized light (right) for hyperbolic hedgehog (-1), $-1/2$, radial hedgehog $(+1)$, $1/2$. m denotes the winding number.

to be described by this model. A more comprehensive theory is the continuum Er-icksen model, which is also restricted to uniaxial liquid crystal as Oseen-Frank model, however, it accounts for spatially variation of the degree of orientational order besides $\boldsymbol{n}$, and the state of liquid crystal is described by a pair $(S, \boldsymbol{n})$, where S is the scalar order parameter. This energy can describe all physically observable defects [43]. The most general continuum theory is based on Landau-de Gennes model which can account for uniaxial and biaxial phases. The tensor order parameter Q is used to describe the orientational order of nematic liquid crystal. As mentioned in [58], Oseen-Frank theory corresponds to the regime where Q have (nearly) everywhere a (nearly) doubly degenerate eigenvalue, and the unique nondegenerate eigenvector then corresponds to the director $\boldsymbol{n}$ under Oseen-Frank theory. Therefore, the defect in Landau-de Gennes model occurs where Q is far from having a doubly degenerate eigenvalue. The energy of point and line defects are finite, which makes Landau-de Gennes model suppress the Oseen-Frank model to capture different types of defects. The analytic description of defects in the Landau-de Gennes model is challenging, nevertheless, there has been substantial progress in recent years in analyzing the existence, structure and stability of certain defects with LdG model [58, 59, 60, 61, 62, 43, 41, 42].

All the three continuous models admit radial hedgehog solution, which possess a radially aligned director field $\boldsymbol{n}$, as shown in Fig. 2.7. The order parameter S is zero at the origin and positive elsewhere. For Landau-de Gennes model, it has been shown both numerically and theoretically that the radial hedgehog solution is not stable for low temperature in the deep nematic regime [50], instead the point defect will broaden into a +1/2 disclination ring, where each point at the ring is a defect with winding number +1/2. The nematic is uniaxial within the ring, and it is surrounded with a torus-shaped region of biaxially. Similar behaviour occurs for line defects, which feature a central core of uniaxiality, surrounded by a ring of biaxiality in which the Q-tensor changes to match

the bulk orientation [63]. As we mentioned earlier, the Oseen-Frank model can only admit isolated point defects and the disclination ring solution does not exist. For the Ericksen's model, although it has been argued that it can predict the disclination line solution, the shape and stability of the line may be quite different from that predicted by the Landau-de Gennes model because the Ericksen's model does not allow biaxiality.

Fig. 2.8 shows the typical structures when there are suspension of surfactant-coated water droplets in uniformly aligned nematic liquid crystal, and the homeotropic anchoring is preferred at the interface, which perturbs the director field and creates defects. The surrounding perturbation and defects are often referred as elastic dipoles (top left) or quadrupoles (top right and bottom) [35], and the configuration depends on the size of the particle, the surface anchoring strength W, the confinement, and the external electric or magnetic fields [64]. As shown in Fig. 2.8, the first plot is the elastic dipole characterized by a $+1$ radial hedgehog sits at the center of the water droplet accompanying with a -1 hyperbolic hedgehog besides the droplet. If the particle size decreases, the hyperbolic hedgehog can be opened up to a topologically equivalent $-1/2$ disclination ring around the equator of the particle, which is called Saturn ring, and this structure represents a quadrupole. When the surface anchoring strength gets weaker, the Saturn ring shrinks the size until it sits directly on the partial, which is named as a surface ring. All of these configurations have been observed in real experiments.

Specifically, the dipole has attracted considerable attention since it is found in the striking self-assembly chaining phenomena created by the colloidal dispersions and emulsions in the nematic liquid crystal continuous phase [32, 33, 34, 35, 36, 37, 38], which offers great potential applications [39, 40]. Theoretical [41] and numerical [42] studies have been conducted to nematic liquid crystal colloids, which show that the dipole configuration with -1 point defects form in between the droplets stablize the chain. The dipole was thoroughly studied with the help of ansatz functions which were motivated
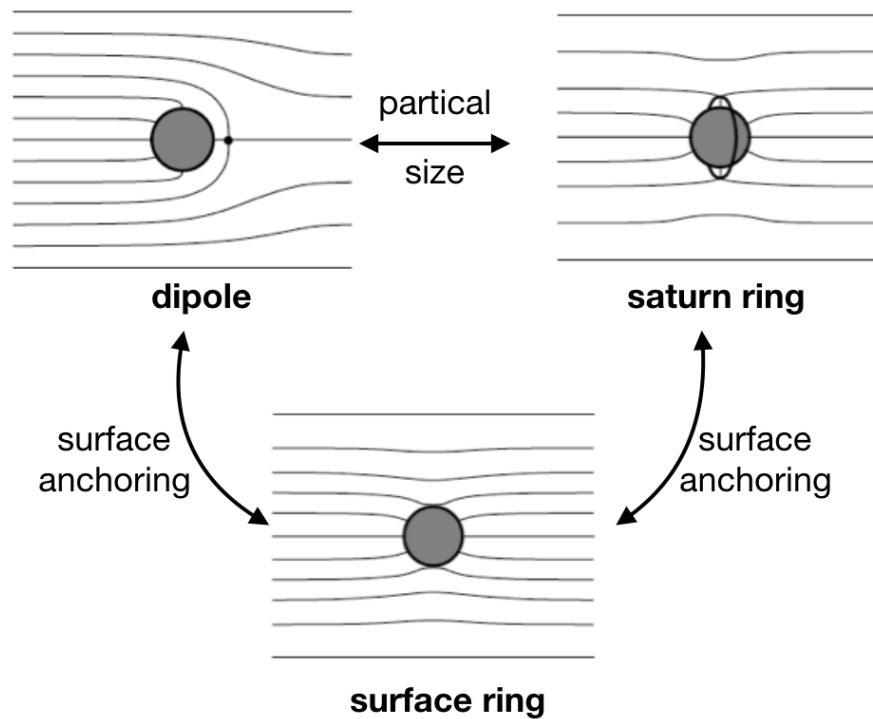
Figure 2.8: A spherical particle with a preferred homeotropic anchoring at its surface that is placed into a uniformly aligned nematic liquid crystal exhibits 3 possible structures: the dipole where the particle is accompanied by a hyperbolic hedgehog, the Saturn ring where the particle is surrounded by a -1/2 disclination ring around the equator, and the surface ring configuration where the -1/2 disclination ring shrink to sit directly on the sphere.

by the electric field solution of electrostatic analogy that a charged metal sphere placed into a uniform electric field. We show two representing dipole configurations in Fig. 2.9. The left plot of Fig. 2.9 shows the case when the bulk is confined between parallel plates treated to force planar anchoring condition at the infinity and homeotropic anchoring condition at the interface of the particles. The water droplets itself is a +1 point defect accompanied with a −1 hyperbolic defect, which produce the total topological charge to be 0. The right plot shows the case when a large nematic droplet contains five water droplets. There is a −1 hyperbolic hedgehog between each pair of particles, thus the number of droplets is always one more than the number of hyperbolic hedgehogs, which produce +1 total topological charge. Both of these two phenomena are explained experimentally [33, 32].
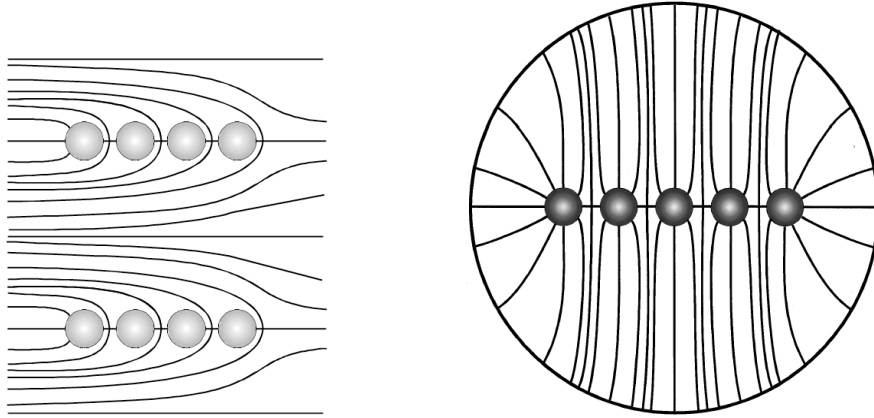
Figure 2.9: Two dipole configurations. Left: water droplets with homogeneous planar anchoring at infinity and homeotropic anchoring at the interface. Each particle is a +1 radial hedgehog accompanied with a −1 hyperbolic defect, and there are exactly as many +1 droplets as the −1 defect, which possess a total topological charge 0. Right: nematic droplet contains water droplets. The −1 point defects appear in between of the droplets, and there is always one less −1 defect than the number of +1 droplets, which generate total topological charge 1.

Chapter 3

Mathematical Model and Numerical Method

3.1 Introduction

In this Chapter, we present the mathematical model and numerical method to learn the the nucleation of an isotropic material in the nematic liquid crystal continuous phase induced from temperature quenching in 2D or 3D channel. The mixture is represented by a compositional order parameter, which is generally the volume fraction of one species, and an orientational order parameter, which describes the nematic liquid crystal. The Cahn-Hilliard framework with these two parameters are extensively exploited to govern the evolution of this type of systems.

In earlier studies, phase field model with a vector order parameter $\boldsymbol{n}$ is applied widely [2, 3, 29]. However, as we mentioned in last Chapter, the vector description has several deficiencies to describe the nematic liquid crystal, and the Landau-de Gennes model which applies a tensor order parameter overcomes the shortcomings and is more comprehensive to study the domain anisotropy. Our work employs the Landau-de Gennes

model, and the free energy of the system is then formulated with the conserved volume fraction of one chosen species and the non-conserved tensor order parameter. The evolution of the system is governed by the coupled time-dependent Ginzburg-Landau equations (model C) [30, 31]. Similar models have been widely used in phase separation studies with some degree of simplification [4, 5, 6, 12, 13, 14, 15]. To the best of our knowledge, this is the first time the full model has been utilized to learn the phase separation in confined geometries.

In the following sections, we discuss the formulation of free energy with Landau-de Gennes model, non-dimensionalization, kinetic equation that minimizes the free energy and governs the evolution, initial and boundary conditions, and the numerical scheme applied.

3.2   Free Energy Formulation

Consider a binary mixture of isotropic fluid and nematic liquid crystal confined between two rigid walls, the system can be described with the tensor order parameter Q and a compositional order parameter $\phi \in [0, 1]$ that represents the local volume fraction of the flexible isotropic polymer in the binary mixture. Assuming the incompressibility of the system, the local volume fraction of the nematic liquid crystal is thus $1 - \phi$. Therefore, the pure, bulk phases are identified with $\phi = 0$ and $\phi = 1$ for the nematic liquid crystal and the isotropic fluid, respectively.

In order to model the thermodynamic behavior of our system, the free energy density functionals introduced in Chapter 2 are the fundamental elements that govern the evolution of the mixture and drive the system to the equilibrium state. The total free energy density f of the system depend on the Q, ϕ and their gradients, $f = f(Q, \nabla Q, \phi, \nabla \phi)$, and it consists of two parts: the Flory-Huggins free mixing energy, which governs phase

separation, and the Laudau-de Gennes free energy, which governs the nematic component. Therefore,

$$f(Q, \nabla Q, \phi, \nabla \phi) = f_{mix}(\phi, \nabla \phi) + f_{nem}(Q, \nabla Q, \phi, \nabla \phi). \tag{3.1}$$

According to Flory-Huggins theory, f_{mix} is given by (2.10). On the basis of the Q tensor model, the free energy of the nematic ordering includes three parts: an orientational distortion energy density of the nematic, f_{ela}, a thermotropic energy density that describes the preferred phase of the nematic, f_{ther}, and the anchoring energy density of the nematic molecules at interfaces, f_{anc}. The surface anchoring along the two rigid walls is strong and imposed as a strict boundary condition instead of an energy penalty. Therefore, we have

$$f_{nem}(Q, \nabla Q, \phi, \nabla \phi) = (1 - \phi)[f_{ela}(\nabla Q) + f_{ther}(Q, \phi) + f_{anc}(Q, \nabla \phi)]. \tag{3.2}$$

To avoid detailed quantitative modeling of materials, the single elastic constant approximation is used, and f_{ela} is chosen as (2.40). The volumetric anchoring (2.55) is used for the interface of the LC-rich and polymer-rich phase since the nucleation generates uncontrolled interface which is not markable. In addition, the homeotropic anchoring is the prevalent, preferential orientation of the director field at the experimentally observed surfaces of the nucleated droplets, and thus we consider $W < 0$ mainly for f_{anc} given by (2.55). The thermotropic energy density f_{ther} takes the form (2.25), and we assume $T_{NI}^* = T_c - d\phi$, where T_c is super-cooling temperature in the absence of isotropic fluid, and the relationship implies that nematic ordering is disturbed by the existence of isotropic phase so that the transition temperature is a decreasing function of ϕ. This form has been used theoretically [4] and it matches with the experimental observations

[65]. More explicitly,

$$f_{mix}(\phi, \nabla\phi) = \frac{\lambda_c}{2}[|\nabla\phi|^2 + \frac{\beta\phi\ln\phi + (1-\phi)\ln(1-\phi) + \frac{g_0}{T}\phi(1-\phi)}{2\epsilon_c^2}],$$

$$f_{nem}(Q, \nabla Q, \phi, \nabla\phi) = (1-\phi)[\frac{K_c}{2}(\nabla_\gamma Q_{\alpha\beta})(\nabla_\gamma Q_{\alpha\beta}) + \frac{W_c}{2}(\nabla_\alpha\phi)(\nabla_\beta\phi)Q_{\alpha\beta} \qquad (3.3)$$

$$+\frac{a_c(T - (T_c - d\phi))}{2}TrQ^2 + \frac{B_c}{3}TrQ^3 + \frac{C_c}{4}(TrQ^2)^2],$$

where we use the subscript c to denote the dimensional parameters. With a rectangular domain $\Omega = [0, L_{xc}] \times [0, L_{yc}]$ for 2D channel, or $\Omega = [0, L_{xc}] \times [0, L_{yc}] \times [0, L_{zc}]$ for 3D channel, the total free energy is

$$F(Q, \nabla Q, \phi, \nabla\phi) = \int_\Omega f(Q, \nabla Q, \phi, \nabla\phi)dV. \qquad (3.4)$$

The parameters can be nondimensionalized by selected characteristic length and energy scales L_c and E_c, respectively. Then, the free energy parameters are made dimensionless with $\lambda = \lambda_c L_c/E_c, \epsilon = \epsilon_c/L_c, W = W_c L_c/E_c, K = K_c L_c/E_c, A = A_c L_c^3/E_c, B = B_c L_c^3/E_c, C = C_c L_c^3/E_c, L_x = L_{xc}/L_c, L_y = L_{yc}/L_c, L_z = L_{zc}/L_c, \Delta x = \Delta x_c/L_c, \Delta y = \Delta y_c/L_c, \Delta z = \Delta z_c/L_c$.

Therefore, the total free energy functional reads

$$F(Q, \nabla Q, \phi, \nabla\phi) = F_{mix}(\phi, \nabla\phi) + F_{nem}(Q, \nabla Q, \phi, \nabla\phi), \qquad (3.5)$$

where

$$F_{mix}(\phi, \nabla\phi) = \int_\Omega d\vec{r}\frac{\lambda}{2}[(\nabla\phi)^2 + \frac{\beta\phi\ln\phi + (1-\phi)\ln(1-\phi) + g\phi(1-\phi)}{2\epsilon^2}],$$

$$F_{nem}(Q, \nabla Q, \phi, \nabla\phi) = \int_\Omega d\vec{r}(1-\phi)[\frac{K}{2}(\nabla_\gamma Q_{\alpha\beta})(\nabla_\gamma Q_{\alpha\beta}) + \frac{W}{2}(\nabla_\alpha\phi)(\nabla_\beta\phi)Q_{\alpha\beta} \quad (3.6)$$

$$+\frac{A}{2}TrQ^2 + \frac{B}{3}TrQ^3 + \frac{C}{4}(TrQ^2)^2].$$

3.3 Kinetic Equation

The evolution of the conserved volume fraction of isotropic phase ϕ and the non-conserved orientational order parameter Q are governed by the coupled time-dependent Ginzburg-Landau(TDGL) equations (model C),

$$\frac{\partial\phi}{\partial t} = \nabla \cdot (M_\phi\nabla\frac{\delta F}{\delta\phi}) + \eta,$$

$$\quad (3.7)$$

$$\frac{\partial Q_{\alpha\beta}}{\partial t} = -M_Q\frac{\delta F}{\delta Q_{\alpha\beta}} + \eta_{\alpha\beta} + \lambda\delta_{\alpha\beta},$$

where M_ϕ and M_Q are the mobility coefficients that depend on the molecular weights of isotropic and liquid crystal molecules as well as the local compositional order parameter ϕ and orientational order parameter Q. The general kinetic equation expresses mobility coefficients as a matrix, which could allow one order parameter to be driven by gradient of the other. Here for simplicity, they are both assumed to be constants as employed by Motoyama et al. in [4].

The thermal noise η and $\eta_{\alpha\beta}$ are neglected. $\delta_{\alpha\beta}$ stands for the Kronecker delta and λ is determined by the traceless condition $TrQ = 0$. We note that a Lagrangian multiplier for the symmetry constraint, $Q_{ij} = Q_{ji}$, is omitted here because non-symmetrical terms

in (2.37) were assumed to be zero. The system (2.12) comprises six coupled nonlinear parabolic partial differential equations, with traceless condition is simplified as $Q_{33} = -Q_{11} - Q_{22}$.

Since Q is a traceless and symmetric matrix, there are only 5 independent components of Q matters,

$$
Q = \begin{bmatrix} Q_{11} & Q_{12} & Q_{13} \\ Q_{12} & Q_{22} & Q_{23} \\ Q_{13} & Q_{23} & -Q_{11} - Q_{22} \end{bmatrix}.
$$

The following computes the variation derivatives of (3.7), which generates the boundary condition and differential equations of ϕ and $Q_{\alpha\beta}$. In order to perform the variation of F with repsect to Q and ϕ, one explicitly introduces the perturbation of ϕ and $Q_{\alpha\beta}$ as $\phi = \phi_0 + \epsilon\psi$, $Q_{\alpha\beta} = (Q_{\alpha\beta})_0 + \epsilon P_{\alpha\beta}$, where $P_{\alpha\beta}$ and ψ are the testing function of $Q_{\alpha\beta}$ and ϕ, respectively. Let $\boldsymbol{v}$ denote the outward normal vector to the boundary $\partial\Omega$. The Gauss divergence theorem are used to generate surface terms, as shown in the box,

$$
\begin{aligned}
&\frac{\partial}{\partial\epsilon}\int_\Omega [\frac{1}{2}(\nabla(\phi + \epsilon\psi))^2]dV\Big|_{\epsilon=0} \\
&= \int_\Omega (\nabla\phi\nabla\psi)dV \\
&= -\int_\Omega \psi\Delta\phi dV + \int_\Omega \nabla\cdot(\psi\nabla\phi)dV \\
&= -\int \psi\Delta\phi dV + \boxed{\int_{\partial\Omega} \psi\frac{\partial\phi}{\partial\boldsymbol{v}}ds},
\end{aligned}
\tag{3.8}
$$

$$\frac{\partial}{\partial \epsilon} \int_\Omega (1-\phi)\frac{K}{2}(\nabla_\gamma\{Q_{\alpha\beta}+\epsilon P_{\alpha\beta}\})(\nabla_\gamma\{Q_{\alpha\beta}+\epsilon P_{\alpha\beta}\})dV\Big|_{\epsilon=0}$$

$$=\int_\Omega K(1-\phi)\nabla_\gamma Q_{\alpha\beta}\nabla_\gamma P_{\alpha\beta}dV$$

$$=-\int_\Omega KP_{\alpha\beta}\nabla_\gamma\{(1-\phi)\nabla_\gamma Q_{\alpha\beta}\}dV+\int_\Omega K\nabla_\gamma\{P_{\alpha\beta}(1-\phi)\nabla_\gamma Q_{\alpha\beta}\}dV$$

$$=-\int_\Omega KP_{\alpha\beta}\nabla\cdot[(1-\phi)\nabla Q_{\alpha\beta}]dV+\boxed{\int_{\partial\Omega} KP_{\alpha\beta}(1-\phi)\frac{\partial Q_{\alpha\beta}}{\partial \boldsymbol{v}}ds},$$

$$\tag{3.9}$$

$$\frac{\partial}{\partial \epsilon} \int_\Omega (1-\phi-\epsilon\psi)\frac{W}{2}(\nabla_\alpha\{\phi+\epsilon\psi\})(\nabla_\beta\{\phi+\epsilon\psi\})Q_{\alpha\beta}dV\Big|_{\epsilon=0}$$

$$=-\int_\Omega \psi\frac{W}{2}(\nabla_\alpha\phi)(\nabla_\beta\phi)Q_{\alpha\beta}dV+\int_\Omega W(1-\phi)(\nabla_\beta\phi)(\nabla_\alpha\psi)Q_{\alpha\beta}dV$$

$$=-\int_\Omega \psi\frac{W}{2}(\nabla_\alpha\phi)(\nabla_\beta\phi)Q_{\alpha\beta}dV-\int_\Omega W\psi\nabla_\alpha\{(1-\phi)\nabla_\beta\phi Q_{\alpha\beta}\}dV$$

$$+\int_\Omega W\nabla_\alpha\{\psi(1-\phi)\nabla_\beta\phi Q_{\alpha\beta}\}dV$$

$$=-\int_\Omega \psi\frac{W}{2}(\nabla_\alpha\phi)(\nabla_\beta\phi)Q_{\alpha\beta}dV-\int_\Omega \psi W\nabla_\alpha\{(1-\phi)\nabla_\beta\phi Q_{\alpha\beta}\}dV$$

$$+\boxed{\int_{\partial\Omega} \psi W(1-\phi)\nabla\phi\cdot Q^T\cdot\boldsymbol{v}ds}.$$

$$\tag{3.10}$$

Thus, we should impose the following boundary conditions to eliminate the boxed terms in (3.8)-(3.10). For $Q_{\alpha\beta}$,

$$\int_{\partial\Omega} KP_{\alpha\beta}(1-\phi)\frac{\partial Q_{\alpha\beta}}{\partial \boldsymbol{v}}ds=0. \tag{3.11}$$

For ϕ,

$$\int_{\partial\Omega} \psi[\frac{\partial\phi}{\partial \boldsymbol{v}}+W(1-\phi)\nabla\phi\cdot Q^T\cdot\boldsymbol{v}]ds=0. \tag{3.12}$$

41

The coupled system of the equations that govern the evolution of the mixture are

$$\frac{1}{M_Q}\frac{\partial Q_{\alpha\beta}}{\partial t} = K\nabla_\gamma[(1-\phi)\nabla_\gamma Q_{\alpha\beta}] - (1-\phi)[\frac{W}{2}(\nabla_\alpha\phi)(\nabla_\beta\phi)$$

$$-\frac{W}{6}(\nabla\phi)^2\delta_{\alpha\beta} + \{A + C(TrQ^2)\}Q_{\alpha\beta} + B(Q^2)_{\alpha\beta} - \frac{B}{3}TrQ^2\delta_{\alpha\beta}],$$

$$\frac{1}{M_\phi}\frac{\partial\phi}{\partial t} = \nabla\cdot\nabla[\lambda(-\nabla^2\phi + \frac{\beta\ln(\phi) - \ln(1-\phi) - 2g\phi}{4\epsilon^2}) + (1-\phi)\frac{ad}{2}TrQ^2 \qquad (3.13)$$

$$-W\nabla_\alpha\{(1-\phi)(\nabla_\beta\phi)Q_{\alpha\beta}\} - \frac{K}{2}(\nabla_\gamma Q_{\alpha\beta})(\nabla_\gamma Q_{\alpha\beta}) - \frac{W}{2}(\nabla_\alpha\phi)(\nabla_\beta\phi)Q_{\alpha\beta}$$

$$-\frac{A}{2}TrQ^2 - \frac{B}{3}TrQ^3 - \frac{C}{4}(TrQ^2)^2].$$

The terms $-\dfrac{W}{6}(\nabla\phi)^2\delta_{\alpha\beta}$ and $-\dfrac{B}{3}TrQ^2\delta_{\alpha\beta}$ are being added to $Q_{\alpha\beta}$ equations to maintain the traceless property of Q tensor.

More explicitly,

$$\frac{1}{M_Q}\frac{\partial Q_{11}}{\partial t} = K\nabla \cdot [(1-\phi)\nabla Q_{11}] - (1-\phi)[\frac{W}{2}(\nabla_x\phi)^2 - \frac{W}{6}(\nabla\phi)^2$$
$$+\{A + C(TrQ^2)\}Q_{11} + B(Q^2)_{11} - \frac{B}{3}TrQ^2],$$

$$\frac{1}{M_Q}\frac{\partial Q_{12}}{\partial t} = K\nabla \cdot [(1-\phi)\nabla Q_{12}] - (1-\phi)[\frac{W}{2}(\nabla_x\phi)(\nabla_y\phi)$$
$$+\{A + C(TrQ^2)\}Q_{12} + B(Q^2)_{12}],$$

$$\frac{1}{M_Q}\frac{\partial Q_{13}}{\partial t} = K\nabla \cdot [(1-\phi)\nabla Q_{13}] - (1-\phi)[\frac{W}{2}(\nabla_x\phi)(\nabla_z\phi)$$
$$+\{A + C(TrQ^2)\}Q_{13} + B(Q^2)_{13}],$$

$$\frac{1}{M_Q}\frac{\partial Q_{22}}{\partial t} = K\nabla \cdot [(1-\phi)\nabla Q_{22}] - (1-\phi)[\frac{W}{2}(\nabla_y\phi)^2 - \frac{W}{6}(\nabla\phi)^2$$
$$+\{A + C(TrQ^2)\}Q_{22} + B(Q^2)_{22} - \frac{B}{3}TrQ^2],$$

(3.14)

$$\frac{1}{M_Q}\frac{\partial Q_{23}}{\partial t} = K\nabla \cdot [(1-\phi)\nabla Q_{23}] - (1-\phi)[\frac{W}{2}(\nabla_y\phi)(\nabla_z\phi)$$
$$+\{A + C(TrQ^2)\}Q_{23} + B(Q^2)_{23}],$$

$$Q_{33} = -Q_{11} - Q_{22},$$

$$\frac{1}{M_\phi}\frac{\partial \phi}{\partial t} = \nabla \cdot \nabla[\lambda(-\nabla^2\phi + \frac{\beta\ln(\phi) - \ln(1-\phi) - 2g\phi}{4\epsilon^2}) + \frac{ad}{2}(1-\phi)TrQ^2$$

$$-W\nabla_\alpha\{(1-\phi)(\nabla_\beta\phi)Q_{\alpha\beta}\} - \frac{K}{2}(\nabla_\gamma Q_{\alpha\beta})(\nabla_\gamma Q_{\alpha\beta}) - \frac{W}{2}(\nabla_\alpha\phi)(\nabla_\beta\phi)Q_{\alpha\beta}$$

$$-\frac{A}{2}TrQ^2 - \frac{B}{3}TrQ^3 - \frac{C}{4}(TrQ^2)^2].$$

The equilibrium profile of the Q and ϕ are found by solving the above set of coupled nonlinear equations with proper initial and boundary conditions.

3.4 Initial and Boundary Condition

First we explore the relationship between Q and $\boldsymbol{n}, S, TrQ^2, TrQ^3$, which are required to display the director field and biaxiality parameter of the mixture,

$$TrQ^2 = Q_{11}^2 + Q_{22}^2 + Q_{33}^2 + 2(Q_{12}^2 + Q_{13}^2 + Q_{23}^2), \tag{3.15}$$

$$TrQ^3 = Q_{11}^3 + Q_{22}^3 + Q_{33}^3 + 3Q_{11}(Q_{12}^2 + Q_{13}^2) + 3Q_{22}(Q_{12}^2 + Q_{23}^2)$$
$$+ 3Q_{33}(Q_{13}^2 + Q_{23}^2) + 6Q_{12}Q_{13}Q_{23}. \tag{3.16}$$

For the uniaxial case, $TrQ^2 = \frac{2}{3}S^2$, which provides a fast way to obtain scalar order parameter S from Q. However, since biaxial case might occur and we use a more general way to update S and $\boldsymbol{n}$. As mention in previous section, $2S/3$ and $\boldsymbol{n}$ are found as the largest eigenvalue and the corresponding eigenvector of tensor Q.

3.4.1 Initial Condition

The initial condition of director field $\boldsymbol{n}_0$, scalar order parameter S_0, and local volume fraction of isotropic phase ϕ_0 are provided. Consequently Q_0 can be initialized by $\boldsymbol{n}_0$ and S, i.e., $Q_0 = S_0(\boldsymbol{n}_0 \otimes \boldsymbol{n}_0 - \frac{1}{3}\boldsymbol{I})$.

We consider an initial state defined by a small perturbation of the uniform mixture,

$$\phi_0(x_i, y_j, z_k) = 0.4 + \gamma_{ijk}, \tag{3.17}$$

where γ_{ijk} is a uniformly distributed random number in $(-0.001, \ 0.001)$.

Assume that the glass walls are coated with polyvinylalcohol and rubbed, which forces the nematic continuous phase to homogeneously align parallel to the slides, this leads to

the following initial director field $\boldsymbol{n}_0$,

$$\boldsymbol{n}_0(x_i, y_j, z_k) = \frac{(1, \omega_{ijk}, 0)}{\sqrt{1 + \omega_{ijk}^2}}, \tag{3.18}$$

where ω_{ijk} is a random number that uniformly distributes between $(0, \eta_j)$ with

$$\eta_j = \begin{cases} \dfrac{1.4(j\Delta y)}{L_y} & \text{if } j\Delta y < \dfrac{L_y}{2}, \\ \dfrac{1.4(L_y - j\Delta y)}{L_y} & \text{if } j\Delta y >= \dfrac{L_y}{2}, \end{cases} \tag{3.19}$$

where L_y is the spacial size between the walls. This makes $\boldsymbol{n}_0$ aligns perfectly parallel to the slides, and perturbed in terms of the distance to the wall. The farther away from the wall, the more $\boldsymbol{n}_0$ is skewed from the planar direction.

The initial S_0 is set to be the equilibrium of the nematic liquid crystal, which is given in (2.35),

$$S_0 = \frac{1}{4C}(-B + \sqrt{B^2 - 24a(T - T_c + d\phi_0)C}). \tag{3.20}$$

3.4.2   Boundary Condition

The boundary conditions of Q and ϕ are required to satisfy (3.11)-(3.12) in order to eliminate the boundary terms generated from variation of calculus. With a rectangular domain $\Omega = [0, L_x] \times [0, L_y] \times [0, L_z]$, where the walls locate at XZ plane and L_y denotes the spacial size between the walls, it is natural to set periodic boundary conditions along X and Z directions, which ensures (3.11) and (3.12) to be hold along the horizontal

directions. Therefore, for any $(x, y, z) \in \Omega$,

$$Q(x, y, z, t) = Q(x + L_x, y, z, t) = Q(x, y, z + L_z, t), \qquad (3.21)$$

$$\phi(x, y, z, t) = \phi(x + L_x, y, z, t) = \phi(x, y, z + L_z, t). \qquad (3.22)$$
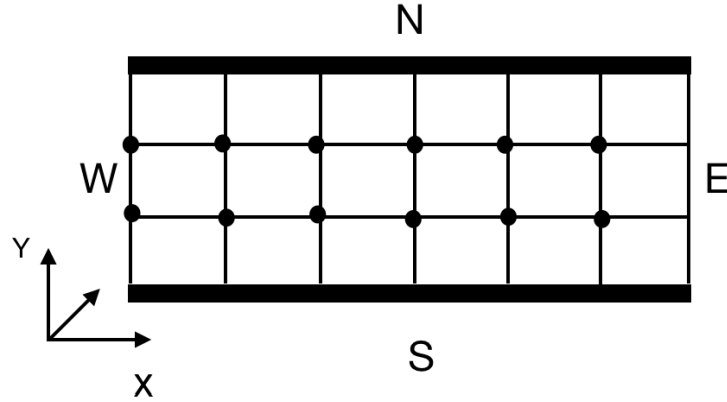
Figure 3.1: Mixture confined between two rigid surfaces N, S.

The walls are usually glass slides that being coated and rubbed to obtain strong uniform long-range anchoring, which makes the molecules homogeneously aligned parallel to the walls. This implies the prescribed boundary values for Q at the walls, and (3.11) is satisfied with test function $P_{\alpha\beta}$ which vanishes at the walls. More specifically,

$$Q\Big|_{y=0,\ L_y} = Q^S = S_{eq}\left(\boldsymbol{\tau} \otimes \boldsymbol{\tau} - \frac{1}{3}\boldsymbol{I}\right), \qquad (3.23)$$

where S_{eq} is determined by (2.35), and $\boldsymbol{\tau}$ is the in plane director field along the walls whose direction is determined by how the glass slides are rubbed.

Now we explore the boundary condition of ϕ at the walls to satisfy (3.12). Denote the unit normal vector of the walls as $\boldsymbol{v}$, with the planar anchoring at the wall, $\boldsymbol{\tau} \cdot \boldsymbol{v} = 0$,

which implies,

$$Q \cdot \boldsymbol{v} = S_{eq}(\boldsymbol{\tau} \otimes \boldsymbol{\tau} - \frac{1}{3}\boldsymbol{I}) \cdot \boldsymbol{v} = -\frac{1}{3}S_{eq} \cdot \boldsymbol{v}, \tag{3.24}$$

therefore,

$$\begin{aligned}
0 &= \frac{\partial \phi}{\partial \boldsymbol{v}} + W(1-\phi)\nabla\phi \cdot Q^T \cdot \boldsymbol{v} \\
&= \frac{\partial \phi}{\partial \boldsymbol{v}} - \frac{W}{3}(1-\phi)S_{eq}\nabla\phi \cdot \boldsymbol{v} \\
&= \frac{\partial \phi}{\partial \boldsymbol{v}}(1 - \frac{W}{3}S + \frac{W}{3}\phi S_{eq}),
\end{aligned} \tag{3.25}$$

which implies,

$$\left.\frac{\partial \phi}{\partial \boldsymbol{v}}\right|_{y=0,\ L_y} = 0. \tag{3.26}$$

The Neumann boundary condition at the walls is sufficient for ϕ to satisfy (3.12).

Since the differential equation of ϕ is 4-th order in (3.13), another boundary condition of ϕ is required. It is derived from the fact that ϕ is a conserved quantity, i.e.

$$\frac{d}{dt}\int_\Omega \phi dV = \int_\Omega \nabla \cdot (M_\phi \nabla \frac{\delta F}{\delta \phi})dV = \int_{\partial\Omega} M_\phi \frac{\partial}{\partial \boldsymbol{v}}(\frac{\delta F}{\delta \phi})ds = 0. \tag{3.27}$$

Along X and Z boundaries, this holds because of the periodic boundary condition. Along Y boundary, we need to set $\left.\frac{\partial}{\partial \boldsymbol{v}}(\frac{\delta F}{\delta \phi})\right|_{y=0,\ L_y} = 0$. More explicitly,

$$\begin{aligned}
\left.\frac{\partial(\lambda(\nabla^2\phi))}{\partial \boldsymbol{v}}\right|_{y=0,\ L_y} &= \frac{\partial}{\partial \boldsymbol{v}}[\lambda(\frac{\beta \ln(\phi) - \ln(1-\phi) - 2g\phi}{4\epsilon^2}) + (1-\phi)\frac{ad}{2}TrQ^2 \\
&- W\nabla_\alpha\{(1-\phi)(\nabla_\beta\phi)Q_{\alpha\beta}\} - \frac{K}{2}(\nabla_\gamma Q_{\alpha\beta})(\nabla_\gamma Q_{\alpha\beta}) - \frac{W}{2}(\nabla_\alpha\phi)(\nabla_\beta\phi)Q_{\alpha\beta} \\
&- \frac{A}{2}TrQ^2 - \frac{B}{3}TrQ^3 - \frac{C}{4}(TrQ^2)^2)]\bigg|_{y=0,\ L_y}.
\end{aligned} \tag{3.28}$$

We conclude that the boundary conditions of ϕ and Q are: (i) along X direction, periodic for both Q and ϕ, and (ii) along Y direction, prescribed value for Q, Neumann

for ϕ, i.e. $Q = Q^S$, $\dfrac{\partial \phi}{\partial \boldsymbol{v}} = 0$ and (3.27) are to be hold.

3.5   Numerical Method

Typical numerical methods used in liquid crystal system for free energy minimization are finite difference, finite element and lattice Boltzmann approach. They all start with molecular fields for tensor order parameter Q or vector order parameter $\boldsymbol{n}$ with given boundary conditions. In our system, the compositional order ϕ is also involved. They are all discretized on the rectangular domain that represents the confined geometry. Both refining and fixed grids are explored in various studies. The non-uniform refining grid usually reduces resolution in the regions where variation of variables is small, and attains dense resolution around the interface of the particles, which helps precisely describe the defects. The square [66], staggered [67], cubic [68, 42], triangular [69] grids have all been explored. In addition, adaptive timestepping has also been used extensively in phase separation studies.

In our system, since numerous droplets nucleate and coalescence in the nematic continuous phase, and there is no track of interface, therefore we apply the uniform grid with finite difference method. At each time step, we need to solve five second order partial differential equations (PDEs) for $Q_{\alpha\beta}$ and one fourth order PDE for ϕ. We enforce strictly the traceless requirement for Q by determining Q_{33} directly from this condition. This coupled system is numerically stiff due to the presence of many high order spatial derivatives. In addition, there are two distinctly different time scales, a fast one associated with an initial fast phase separation and a slow one in which domain coarsening takes place. In order to relax the numerical stiffness, we employ a semi-implicit method in which we identify the linearly dominant terms at small scales and discretize these implicitly while treating the remaining nonlinear terms explicitly.

For 2D channel, we assume there are no gradients in the z direction, i.e. $\nabla_z f = 0$ for any of the relevant functions f. The time discretized form of (**??**) are presented below.

3.5.1   Solver for Q

The Q equations in (3.13) are discretized along temporal direction as follows,

$$\frac{1}{M_Q}\frac{Q_{\alpha\beta}^{j+1} - Q_{\alpha\beta}^{j}}{\Delta t} = \mu_1(\Delta Q_{\alpha\beta})^{j+1} + g(\phi^j, Q_{\alpha\beta}^j), \qquad (3.29)$$

where $\mu_1 = \dfrac{\max(K(1-\phi))}{2} = \dfrac{K}{2}$ is a numerical constant parameter introduced to relax the timestep stability constraint [70], and

$$\begin{aligned}
g(\phi, Q_{\alpha\beta}) =&(K(1-\phi) - \mu_1)\Delta Q_{\alpha\beta} - K\nabla\phi\nabla Q_{\alpha\beta} - (1-\phi)[\frac{W}{2}(\nabla_\alpha\phi)(\nabla_\beta\phi)\\
&- \frac{W}{6}(\nabla\phi)^2\delta_{\alpha\beta} + \{A + C(TrQ^2)\}Q_{\alpha\beta} + B(Q^2)_{\alpha\beta} - \frac{B}{3}TrQ^2\delta_{\alpha\beta}].
\end{aligned} \qquad (3.30)$$

These equations are solved in a rectangular domain with periodic boundary condition along X and Z directions. Therefore, we can do discrete Fourier transform along X and Z, respectively, and obtain a linear system along Y direction. The subscripts are omit for simplicity.

We discretize the domain $\Omega = [0, L_x]\times[0, L_y]\times[0, L_z]$ into M, N, P parts, respectively. Apply central difference to approximate the Laplacian, for $m = 2, 3, \cdots, M - 1$, $n = 2, 3, \cdots, N - 1$, $p = 2, 3, \cdots, P - 1$,

$$\begin{aligned}
\frac{1}{M_Q}\frac{Q_{mnp}^{j+1} - Q_{mnp}^{j}}{\Delta t} =&\mu_1\frac{Q_{m+1,n,p}^{j+1} - 2Q_{mnp}^{j+1} + Q_{m-1,n,p}^{j+1}}{(\Delta x)^2}\\
&+ \mu_1\frac{Q_{m,n,p+1}^{j+1} - 2Q_{mnp}^{j+1} + Q_{m,n,p-1}^{j+1}}{(\Delta z)^2}\\
&+ \mu_1\frac{Q_{m,n+1,p}^{j+1} - 2Q_{mnp}^{j+1} + Q_{m,n-1,p}^{j+1}}{(\Delta y)^2} + g_{mnp}(\phi^j, Q^j).
\end{aligned} \qquad (3.31)$$

With the following DFT,

$$Q_{mnp} = \frac{1}{MP} \sum_{k=1}^{M} \sum_{q=1}^{P} \hat{Q}_{knq} \exp(\frac{2\pi i(m-1)(k-1)}{M}) \exp(\frac{2\pi i(p-1)(q-1)}{P}),$$

$$\hat{Q}_{knq} = \sum_{m=1}^{M} \sum_{p=1}^{P} Q_{mnp} \exp(\frac{-2\pi i(m-1)(k-1)}{M}) \exp(\frac{-2\pi i(p-1)(q-1)}{P}),$$

(3.32)

it implies,

$$\frac{1}{M_Q} \frac{\hat{Q}_{knq}^{j+1} - \hat{Q}_{knq}^{j}}{\Delta t} = L_{kq}\hat{Q}_{knq}^{j+1} + \mu_1 \frac{\hat{Q}_{k,n+1,q}^{j+1} - 2\hat{Q}_{knq}^{j+1} + \hat{Q}_{k,n-1,q}^{j+1}}{(\Delta y)^2} + \hat{g}_{knq}(\phi^j, Q^j), \quad (3.33)$$

where

$$L_{kq} = \frac{2\mu_1}{(\Delta x)^2}(\cos(\frac{2\pi(k-1)}{M}) - 1) + \frac{2\mu_1}{(\Delta z)^2}(\cos(\frac{2\pi(q-1)}{P}) - 1). \quad (3.34)$$

Rearrange the equation yields

$$\frac{\hat{Q}_{k,n+1,q}^{j+1} - 2\hat{Q}_{knq}^{j+1} + \hat{Q}_{k,n-1,q}^{j+1}}{(\Delta y)^2} = \frac{(1 - L_{kq}M_Q dt)\hat{Q}_{knq}^{j+1} - \hat{Q}_{knq}^{j} - \hat{g}_{knq}(\phi^j, Q^j)M_Q dt}{\mu_1 M_Q \Delta t}, \quad (3.35)$$

which can be discretized as a tridiagonal linear system for each $k = 1, 2, \cdots, M$, $q = 1, 2, \cdots, P$,

$$\begin{bmatrix} -2-\alpha_{kq} & 1 & & & \\ 1 & -2-\alpha_{kq} & 1 & & \\ & \cdots & \cdots & \cdots & \\ & & 1 & -2-\alpha_{kq} & 1 \\ & & & 1 & -2-\alpha_{kq} \end{bmatrix} \begin{bmatrix} \hat{Q}_{k,2,q}^{n+1} \\ \\ \vdots \\ \\ \hat{Q}_{k,N-1,q}^{n+1} \end{bmatrix} = \begin{bmatrix} \beta_{k,2,q} - \hat{Q}_{k,1,q} \\ \beta_{k,3,q} \\ \vdots \\ \beta_{k,N-2,q} \\ \beta_{k,N-1,q} - \hat{Q}_{k,N,q} \end{bmatrix}.$$

(3.36)

where

$$\alpha_{kq} = \left(\frac{1}{\mu_1 M_Q \Delta t} - \frac{L_{kq}}{\mu_1}\right)(\Delta y)^2,$$

$$\beta_{knq} = \left(-\frac{\hat{g}_{knq}^j(\phi^j, Q^j)}{\mu_1} - \frac{\hat{Q}_{knq}}{\mu_1 M_Q \Delta t}\right)(\Delta y)^2,$$
(3.37)

and the terms $\hat{Q}_{k,1,q}$ and $\hat{Q}_{k,N,q}$ are determined by the Dirichlet boundary condition of Q at the walls.

3.5.2   Solver for ϕ

Assume the mobility M_ϕ is a constant, the equation of ϕ in (3.13) is discretized as follows,

$$\frac{1}{M_\phi}\frac{\phi^{j+1} - \phi^j}{\Delta t} = \nabla \cdot \nabla[-\lambda(\Delta\phi)^{j+1} + \mu_2\phi^{j+1} + h(\phi^j, Q_{\alpha\beta}^j)],$$
(3.38)

where

$$\mu_2 = \max\left|\frac{d}{d\phi}\lambda\left(\frac{\beta\ln(\phi) - \ln(1-\phi) - 2g\phi}{2\epsilon^2}\right)\right|$$
(3.39)

is used to relax the timestep stability constraint [70], and

$$\begin{aligned}
h(\phi, Q_{\alpha\beta}) =& \lambda\left(\frac{\beta\ln(\phi) - \ln(1-\phi) - 2g\phi}{2\epsilon^2}\right) - \mu_2\phi + \frac{ad}{2}(1-\phi)TrQ^2 \\
& - W\nabla_\alpha\{(1-\phi)(\nabla_\beta\phi)Q_{\alpha\beta}\} - \frac{K}{2}(\nabla_\gamma Q_{\alpha\beta})(\nabla_\gamma Q_{\alpha\beta}) \\
& - \frac{W}{2}(\nabla_\alpha\phi)(\nabla_\beta\phi)Q_{\alpha\beta} - \frac{A}{2}TrQ^2 - \frac{B}{3}TrQ^3 - \frac{C}{4}(TrQ^2)^2.
\end{aligned}$$
(3.40)

Similar with Q equations, the periodic boundary condition for ϕ ensures the DFT along X and Z directions. Along Y there are 2 boundary conditions,

$$\frac{\partial\phi}{\partial y} = 0,$$
(3.41)

$$\frac{\partial(\Delta\phi)}{\partial y} = \frac{1}{\lambda}\frac{\partial h}{\partial y} \tag{3.42}$$

where

$$\begin{aligned}
\frac{1}{\lambda}\frac{\partial h}{\partial y} = \frac{1}{\lambda}(\{&(1-\phi)ad - A - CTrQ^2\}Q_{\alpha\beta}\frac{\partial Q_{\alpha\beta}}{\partial y} - B(Q^2)_{\alpha\beta}\frac{\partial Q_{\alpha\beta}}{\partial y} \\
&+ (\frac{W}{2}(\phi_x)^2 - W(1-\phi)\phi_{xx})\frac{\partial Q_{11}}{\partial y} - W(1-\phi)\phi_x\frac{\partial(\nabla_\alpha Q_{1\alpha})}{\partial y} \\
&- K(\nabla_\gamma Q_{\alpha\beta})\frac{\partial(\nabla_\gamma Q_{\alpha\beta})}{\partial y}).
\end{aligned} \tag{3.43}$$

At the walls we have a Dirichlet boundary condition for Q (3.23) and Neumann boundary conditions for ϕ(3.41) and for the Laplacian of ϕ (3.42), respectively. The latter involves derivatives of Q and since these are not specified at the boundary, condition (**??**) represents a notable challenge. Other numerical investigations have avoided this problem by opting to use instead the homogeneous Neumann boundary condition. We prove below that this condition can be expressed in the following form:

Proposition: The discretization form of (3.38) remains the same if we simplify the boundary condition (3.42) as follows

$$\frac{\partial^3\phi}{\partial y^3} = \frac{1}{\lambda}\frac{\partial h}{\partial y} = 0. \tag{3.44}$$

Proof: Consider 2D discretization of (3.38), for $m = 1, \cdots, M, \ n = 1, \cdots, N,$

$$\frac{1}{M_\phi}\frac{\phi^{j+1} - \phi^j}{\Delta t} - \mu_2(\Delta\phi)^{j+1} + \lambda(\Delta\phi)_{xx}^{j+1} + \lambda(\Delta\phi)_{yy}^{j+1} = h_{xx}^j + h_{yy}^j. \tag{3.45}$$

The terms that relevant to boundary condition (3.42) is $\Sigma = \lambda(\Delta\phi)_{yy}^{j+1} - h_{yy}^j$. After

imposing the ghost points $\phi_{m,0}$ and $h_{m,0}$ for the bottom wall,

$$\Sigma_S = \lambda \frac{(\Delta\phi)_{m,2}^{j+1} - 2(\Delta\phi)_{m,1}^{j+1} + (\Delta\phi)_{m,0}^{j+1}}{(\Delta y)^2} - \frac{h_{m,2}^j - 2h_{m,1}^j + h_{m,0}^j}{(\Delta y)^2}. \tag{3.46}$$

Assume the boundary condition $\dfrac{\partial(\Delta\phi_{m,1})}{\partial y} = \dfrac{1}{\lambda}\dfrac{\partial(h_{m,1})}{\partial y} = \xi$, by central difference it reads

$$\frac{(\Delta\phi)_{m,2} - (\Delta\phi)_{m,0}}{2\Delta y} = \xi,$$

$$\frac{1}{\lambda}\frac{h_{m,2} - h_{m,0}}{2\Delta y} = \xi, \tag{3.47}$$

which implies,

$$\begin{aligned} \Sigma_S &= \lambda \frac{2(\Delta\phi)_{m,2}^{j+1} - 2(\Delta\phi)_{m,1}^{j+1}}{(\Delta y)^2} - \frac{h_{m,2}^j - 2h_{m,1}^j}{(\Delta y)^2} + \frac{2\lambda\xi\Delta y}{(\Delta y)^2} - \frac{2\lambda\xi\Delta y}{(\Delta y)^2} \\ &= \lambda \frac{2(\Delta\phi)_{m,2}^{j+1} - 2(\Delta\phi)_{m,1}^{j+1}}{(\Delta y)^2} - \frac{h_{m,2}^j - 2h_{m,1}^j}{(\Delta y)^2}. \end{aligned} \tag{3.48}$$

This is the discretization form when we assume that $\phi_{yyy} = 0$ and $\dfrac{\partial h}{\partial y} = 0$. The north boundary can be treated similarly by imposing ghost points $\phi_{m,N+1}$ and $h_{m,N+1}$. Therefore, (3.44) can be used and makes its enforcement more tractable than (3.42).

$\square$

For $3D$ simulation, we want to take the following DFT along X and Z directions,

$$\phi_{mnp} = \frac{1}{MP} \sum_{k=1}^{M} \sum_{q=1}^{P} \hat{\phi}_{knq} \exp(\frac{2\pi i(m-1)(k-1)}{M}) \exp(\frac{2\pi i(p-1)(q-1)}{P}),$$

$$\hat{\phi}_{knq} = \sum_{m=1}^{M} \sum_{p=1}^{P} \phi_{mnp} \exp(\frac{-2\pi i(m-1)(k-1)}{M}) \exp(\frac{-2\pi i(p-1)(q-1)}{P}). \tag{3.49}$$

After the discretization for (3.38) and Fourier transform, we could derive that for $k =$

$1, \cdots, M, n = 1, \cdots, N, q = 1, \cdots, P,$

$$\frac{1}{M_\phi} \frac{\hat{\phi}_{knq}^{j+1} - \hat{\phi}_{knq}^{j}}{\Delta t} = -\lambda(\alpha_{1k} + \alpha_{1q} + 2\alpha_{2k}\alpha_{2q})\hat{\phi}_{knq}^{j+1} + \mu_2(\alpha_{2k} + \alpha_{2q})\hat{\phi}_{knq}^{j+1}$$
$$- \lambda(\hat{\phi}_{knq}^{j+1})_{yyyy} - 2\lambda(\alpha_{2k} + \alpha_{2q})(\hat{\phi}_{knq}^{j+1})_{yy} + (\Delta h)_{knq}^{j}, \tag{3.50}$$

where

$$\alpha_{1k} = \frac{1}{(\Delta x)^4}(6 - 8\cos(\frac{2\pi(k-1)}{M}) + 2\cos(\frac{4\pi(k-1)}{M})),$$

$$\alpha_{1q} = \frac{1}{(\Delta z)^4}(6 - 8\cos(\frac{2\pi(q-1)}{P}) + 2\cos(\frac{4\pi(q-1)}{P})),$$

$$\alpha_{2k} = \frac{1}{(\Delta x)^2}(2\cos(\frac{2\pi(k-1)}{M}) - 2), \tag{3.51}$$

$$\alpha_{2q} = \frac{1}{(\Delta z)^2}(2\cos(\frac{2\pi(q-1)}{P}) - 2).$$

Rearrange the equation yields,

$$\lambda(\hat{\phi}_{knq}^{j+1})_{yyyy} + 2\lambda(\alpha_{2k} + \alpha_{2q})(\hat{\phi}_{knq}^{j+1})_{yy} + \lambda(\alpha_{1k} + \alpha_{1q} + 2\alpha_{2k}\alpha_{2q})\hat{\phi}_{knq}^{j+1} +$$
$$\mu_2(\alpha_{2k} + \alpha_{2q})\hat{\phi}_{knq}^{j+1} + \frac{\hat{\phi}_{knq}^{j+1}}{M_\phi \Delta t} = \frac{\hat{\phi}_{knq}^{j}}{M_\phi \Delta t} + (\Delta h)_{knq}^{j}. \tag{3.52}$$

This corresponds to the linear system,

$$
\begin{bmatrix}
\beta_3 & \beta_2 + \beta_4 & \beta_1 + \beta_5 & & & & \\
\beta_2 & \beta_1 + \beta_3 & \beta_4 & \beta_5 & & & \\
\beta_1 & \beta_2 & \beta_3 & \beta_4 & \beta_5 & & \\
\cdots & \cdots & \cdots & \cdots & \cdots & & \\
& \beta_1 & \beta_2 & \beta_3 & \beta_4 & \beta_5 & \\
& & \beta_1 & \beta_2 & \beta_3 + \beta_5 & \beta_4 & \\
& & & \beta_1 + \beta_5 & \beta_2 + \beta_4 & \beta_3
\end{bmatrix}
\begin{bmatrix}
\hat{\phi}_{k,1,q}^{n+1} \\
\vdots \\
\vdots \\
\vdots \\
\hat{\phi}_{k,N,q}^{n+1}
\end{bmatrix}
=
\begin{bmatrix}
\dfrac{\hat{\phi}_{k1q}^{j}}{M_\phi \Delta t} + (\Delta h)_{k1q}^{j} \\
\vdots \\
\vdots \\
\vdots \\
\dfrac{\hat{\phi}_{kNq}^{j}}{M_\phi \Delta t} + (\Delta h)_{kNq}^{j}
\end{bmatrix},
$$

$$(3.53)$$

where

$$
\begin{aligned}
\beta_1 &= \beta_5 = \frac{\lambda}{(\Delta y)^4}, \\
\beta_2 &= \beta_4 = \frac{2\lambda(\alpha_{2k} + \alpha_{2q}) - \mu}{(\Delta y)^2} - \frac{4\lambda}{(\Delta y)^4}, \\
\beta_3 &= \frac{1}{M\Delta t} + \lambda(\alpha_{1k} + \alpha_{1q} + 2\alpha_{2k}\alpha_{2q}) - \mu(\alpha_{2k} + \alpha_{2q}) \\
&\quad + \frac{-4\lambda(\alpha_{2k} + \alpha_{2q}) + 2\mu}{(\Delta y)^2} + \frac{6\lambda}{(\Delta y)^4}.
\end{aligned}
$$

$$(3.54)$$

Note that in order to obtain $h(\phi, Q)$ at the walls ($n = 1$ and $n = N$) we extrapolate $\nabla_\nu Q_{\alpha\beta}$ from the interior values. The algorithm flow is shown in Fig. 3.2.

3.6   Parameters

In this section, we want to specify the parameters used in the simulation. There is a large number of parameters in the Landau-de Gennes model. We have chosen these parameters to approximate those of a 5CB nematic liquid crystal [42]. Their values
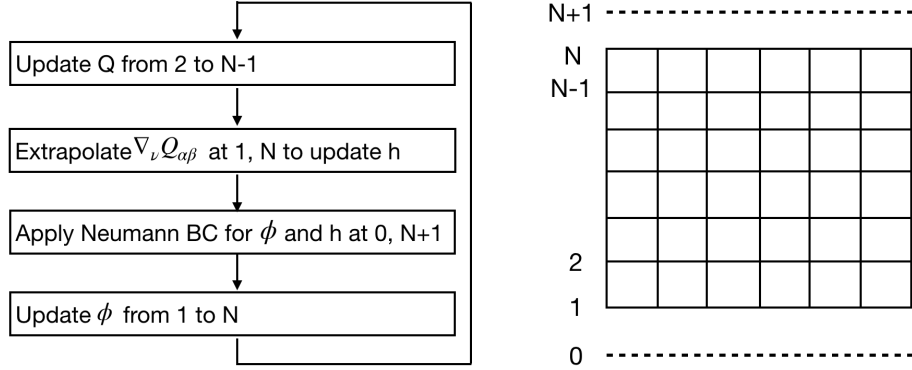
Figure 3.2: Algorithm flow of the coupled system. The dashed line at 0 and $N + 1$ are ghost points induced for ϕ and h, whose values are found by Neumann boundary condition.

and the numerical mesh sizes are provided in Table 3.1. The quenching temperature, and initial composition were selected so that some phase separation or nucleation takes place before there is any significant orientational order away from the walls. Two sets of thermotropic energy parameters (a, B, and C) are considered (labeled Set 1 and Set 2 in Table 3.1) to obtain an initially nematic and isotropic state of the LC component as determined by S_{eq}, which is evaluated using (2.35) with $\phi = 0.4$ as the initial, mean polymer concentration. The two values of S_{eq} in Table 3.1 correspond to a weakly nematic initial state of the LC for Set 1 and an isotropic state for Set 2.

The correlation length ξ_N, which gives a measure of the orientational defect size if there is any, was computed using (2.51). Consequently, to adequately resolve such small length scale we take the uniform mesh size to be $\Delta x_c = \Delta y_c = 10nm$. The (fictitious time) step size is $\Delta t = 0.1$ and remains constant through all simulations. For 2D experiment, the rectangular domain size is set to be $L_{xc} = 2.56\mu m$ and $L_{yc} = 2.56\mu m$. For 3D case, $L_{xc} = 1.28\mu m$, $L_{yc} = 1\mu m$, and $L_{zc} = 1.28\mu m$. In both cases, the normal-wall direction is y.

As mentioned in Section 3.2, the parameters are nondimensionalzed by choosing a

Parameters	Set 1	Set 2
λ_c	$4 \times 10^{-11} J/m$	*
K_c	$4 \times 10^{-11} J/m$	*
W_c	$-1 \times 10^{-10} J/m$	*
a_c	$0.553 \times 10^5 J/m^3 K$	$8 \times 10^5 J/m^3 K$
B_c	$-0.7155 \times 10^6 J/m^3$	$-0.1 \times 10^6 J/m^3$
C_c	$0.8758 \times 10^6 J/m^3$	$1.6 \times 10^6 J/m^3$
M_Q	$10^{-20} m^3/J\Delta t$	*
M_ϕ	$10^{-4} m^3/J\Delta t$	*
β	1	*
g_0	2.8K	*
T	1.3K	*
T_c	2K	*
d	2K	*
ϵ_c	50nm	*
S_{eq}	0.384	0
ξ_N	22.29nm	85.05nm
Δx_c	10nm	*
Δy_c	10nm	*
Δt	0.1	*

Table 3.1: Two sets of parameters used for numerical simulations. Set 1 corresponds roughly to 5CB nematic liquid crystal [42], and * in set 2 takes the same value as in set 1. The temperature related parameters are taken from [4].

characteristic length scale L_c and a characteristic energy scale E_c. We take $L_c = 1\mu m$ and $E_c = 1 \times 10^{-14} J$.

We also want to check the evolution of the total volume fraction, which is expected to be preserved, and the total free energy, which shall decrease monotonically per step. The total amount of these quantities in the rectangular domain is approximated by the

composite trapezoidal rule, which reads

$$
\begin{aligned}
\iint_\Omega f(x,y)dxdy \approx \frac{1}{4}\Delta x \Delta y (&f(0,0) + f(0,H) + f(L,0) + f(L,H) \\
&+ 2\sum_{i=1}^{M-1}(f(x_i,0) + f(x_i,H)) + 2\sum_{j=1}^{N-1}(f(0,y_j) + f(L,y_j)) \\
&+ 4\sum_{i=1}^{M-1}\sum_{j=1}^{N-1} f(x_i,y_j)).
\end{aligned}
\tag{3.55}
$$

For all simulation reported in this paper, it is verified that the free energy decreased monotonically per step and the total volume fraction is preserved accurately with a 10^{-13} variation after 10^4 steps.

Chapter 4

2D Order in Confined Walls

4.1 Introduction

In this Chapter, we present our numerical results of ordering and structure formation of an isotropic material, such as a flexible polymer, nucleating in a liquid crystal (LC) continuous phase in a 2D channel. The polymer-LC system is confined between two parallel walls and periodic boundary conditions are imposed in the parallel-wall direction. The walls are usually glass slides that being coated and rubbed to obtain uniform long-range anchoring, which makes the molecules homogeneously aligned parallel to the walls. We are particularly concerned with the interplay of phase separation and nematic ordering induced by wall anchoring so we impose strong planar anchoring at the walls and examine both homeotropic and planar anchoring at the polymer-LC surfaces.

The Chapter is organized as follows. First, we start with the Cahn-Hilliard equation which contains plain mixing energy only, and the nematic effect is omitted. The result generated are compared with the full system, so that we could have a better understanding about how a nematic component affects the morphology of nucleation under temperature quenching. Next, we present two fabulous structures found with appropriate

parameter sets, which are chain order and lamellae order. The effect of elastic energy strength, anchoring energy strength and mixing energy strength are discussed. Lastly, we have shown that the Landau-de Gennes model in this framework is incapable to preserve the dipole configuration, instead the -1 point defect opens up to two $-1/2$ point defects in 2D and a $-1/2$ disclination ring in 3D, which represents a quadrupole. Therefore, the dipole cannot be sustained and it provides an explanation about why the chain order structure cannot be arrested in our model.

4.2 Cahn-Hilliard Equation

First, we consider only mixing free energy in the system, and the free energy generated by nematic component is ignored. Therefore, the system only involves a compositional order parameter ϕ, and the corresponding Cahn-Hilliard equation governs the evolution of ϕ,

$$\frac{\partial \phi}{\partial t} = \nabla \cdot M_\phi \nabla \mu, \tag{4.1}$$

where

$$\mu = \frac{\delta F_{mix}}{\delta \phi} = \lambda(-\nabla^2 \phi + \frac{\beta \ln(\phi) - \ln(1 - \phi) - 2g\phi}{4\epsilon^2}). \tag{4.2}$$

The simulation is run with step $\Delta t = 0.1$ up to t=15000 from the slightly perturbed initial phase $\phi \sim 0.4$, the quenching temperature is $T = 1.3$, which is considered a relatively shallow quench. The results are shown in Fig. 4.1, where the isotropic-rich phase is shown in blue and the nematic-rich phase is red. The colorbar shows the volume fraction of the red phase. Initially, there is diffusion of the volume fraction at $t = 2000$, and the small isotropic particles start to nucleate at $t = 3000$ throughout the entire domain and subsequently grow the size with coalescence at the following steps.

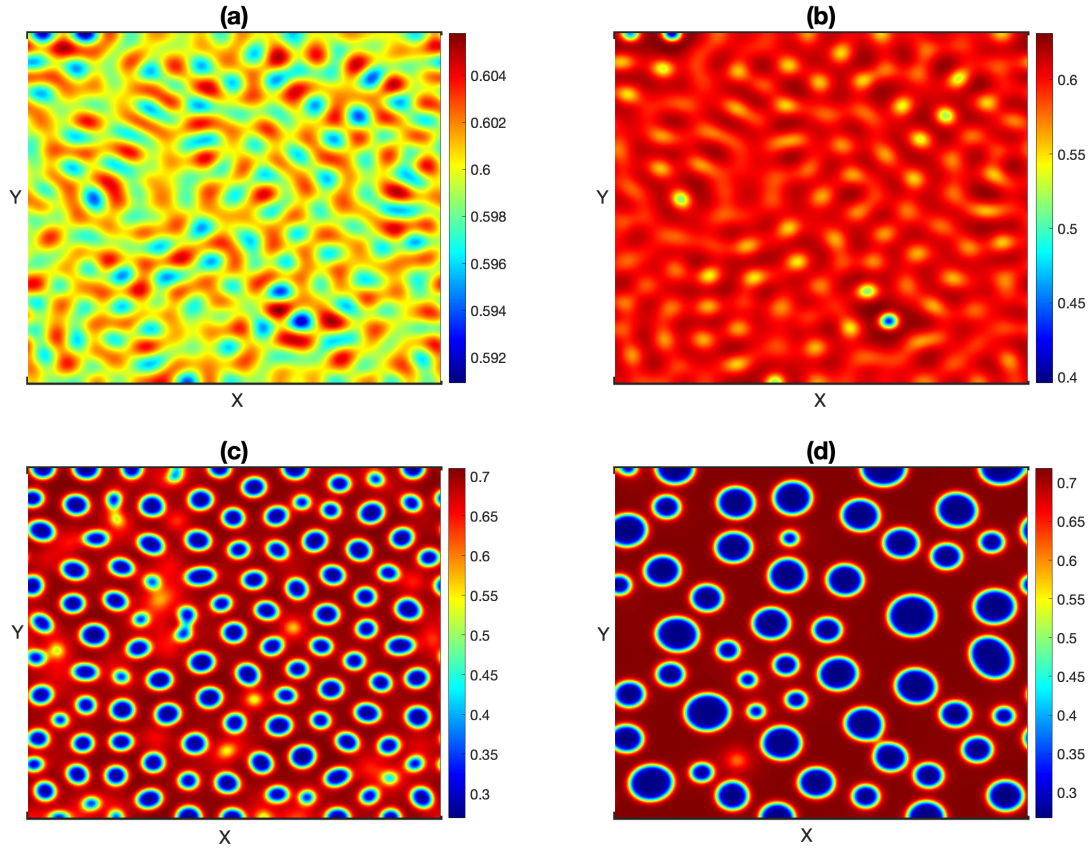We have also explored different quenching temperature T at $T = 1.1$, 1.2. As shown

Figure 4.1: *From left to right* phase separation evolution at steps $t = 2000,\ 3000,\ 4000,\ 20000$ for Cahn-Hilliard equation containing mixing energy only. The quenching temperature $T = 1.3$, capillary length $\epsilon = \dfrac{\Delta x}{2}$.
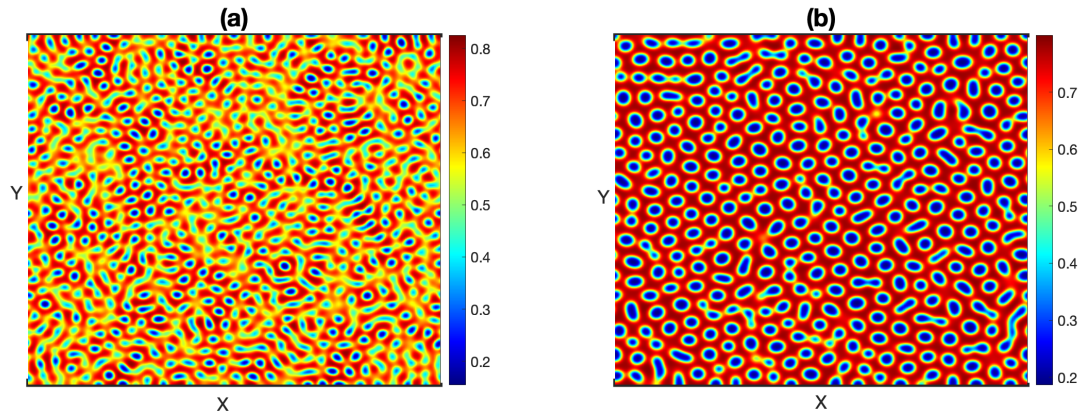

Figure 4.2: The initial step at which minority phase starts nucleate with quenching temperature (a) $T = 1.1$, (b)$T = 1.2$. The step is (a) $t = 100$, (b) $t = 400$.

in Fig. 4.2, T has a significant effect on the speed and extent of phase separation. The initial step that nucleation occurs with $T = 1.1$, 1.2 are $t = 100$, 400, respectively, whereas for $T = 1.3$ is $t = 4000$. With smaller T and deeper quenching, the larger force drives a faster and stronger nucleation, and the volume fraction ϕ also possess extremer value. As $T = 1.3$, $\phi = 0.27$, 0.72 characterize the LC-rich and polymer-rich region, respectively. With deeper quench, the extreme values for ϕ are 0.19, 0.82 at $T = 1.2$, and 0.13, 0.87 for $T = 1.1$. It is also worth noting that deeper quench yields smaller droplet size as is evidenced in Fig. 4.2.

4.3 Nucleation with Nematic Component

4.3.1 Chain Order

Now we consider the full system with nematic effects, and compare the structures created with the Cahn-Hilliard equation.

The experimental results of Loudet, Barois, and Poulin [32] show spectacularly that a polymer phase can nucleate in a confined nematic LC matrix to form highly ordered droplet chains whose orientation can be controlled by wall anchoring. We examine next to which extent this fascinating phenomenon can be captured by the Landau-de Gennes model.

We consider a relatively shallow quench (T=1.3) so that some phase separation occurs prior to when the orientational order becomes significant. The surface anchoring at the interface of the polymer particles is homeotropic, i.e. the preferential nematic orientation at the polymer-LC interfaces is normal to those surfaces. This is also the prevalent, preferential anchoring at the experimental surfaces of the nucleated droplets. The strong wall anchoring is homogeneously align along the wall. After nondimensionalization of

parameters in Set 1 of Table 3.1, the values of relevant parameters are $a = 5.528$, $B = -71.55$, and $C = 87.58$ for the thermotropic energy, and $W = -0.01$, $K = 0.004$, and $\lambda = 0.004$ for the anchoring strength, the elastic constant, and the mixing energy strength, respectively.
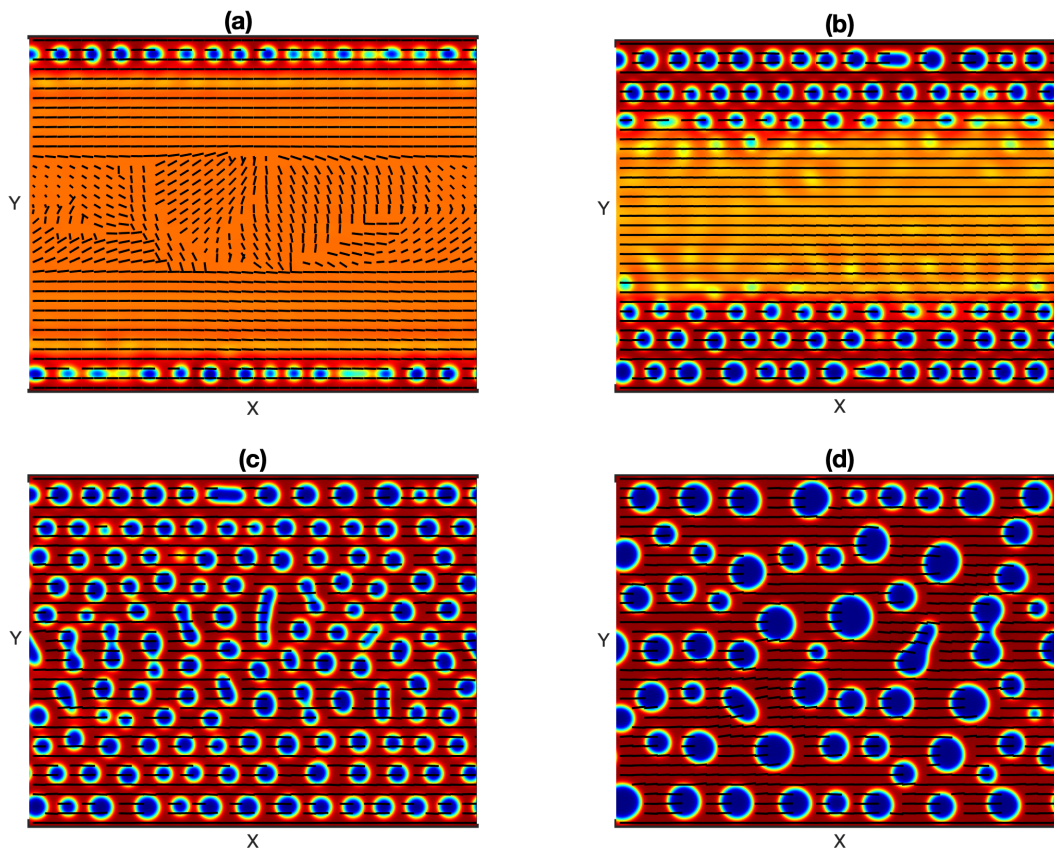

Figure 4.3: Time sequence of the polymer volume fraction ϕ and the subsampled director field for a polymer phase nucleating in a liquid-crystal matrix at (nondimensional times) (a) $t = 1000$, (b) $t = 2000$, (c) $t = 3000$, and (d) $t = 12000$. The thermotropic energy parameters are $a = 5.528$, $B = -71.55$, $C = 87.58$. LC-rich phase in red and polymer-rich phase in blue.

Figure 4.3 displays a series of snapshots of the phase separation process in the 2D channel. The polymer-rich phase is shown in blue and the LC-rich phase in red. A subsampled, in-plane component of the director field is also displayed. In the early stages of the spinodal decomposition [Fig. 4.3(a)], a row of polymer-rich droplets is nucleated

adjacent to each wall in two corresponding LC-rich layers. The wall anchoring induces an orientational order that quickly propagates from the walls inward, toward the channel center, and produces a director field that is nearly horizontal in about 2/3 of the domain.

LC-rich layers immediately next to the walls have also been observed in the simulations by Xia *et al.* [6] for a similar system but with free wall anchoring (i.e. no preferred nematic orientation enforced at the walls) and with an affinity wall potential. Here, however, the LC-layers are induced by the planar wall anchoring, which has a dramatic long range effect as Fig. 4.3(b) shows; the director field is horizontal at the domain center and more rows of polymer-rich droplets have formed. In contrast, in a typical spinodal decomposition of a binary mixture with a dominant component as modelled by the Cahn-Hilliard equation, the minority phase starts to nucleate throughout the entire domain without any ordering.
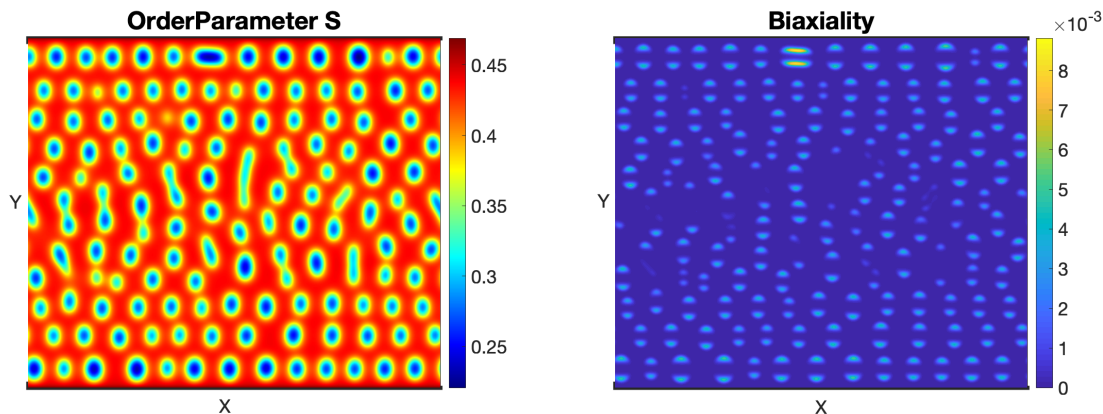

Figure 4.4: The left and right plots are the order parameter S and biaxiality $\beta(Q)$ taken at $t = 3000$.

The nucleated droplets create some distortion on the orientational order induced by the walls. Note that the surface anchoring is not strong (the director field is not entirely normal to the polymer-LC surfaces). In the current model, to simulate homeotropic surface anchoring W has to be negative and so a large $|W|$ necessitates a larger mixing energy strength λ to keep the system well-posed. As a result, when we increase both

parameters we would see elongated polymer-rich domains instead of circular droplets. In other words, there is a delicate balance of wall and surface anchoring, mixing energy, orientational elasticity and thermotropic effects that comes into play within the Landau-de Gennes model to give rise to this extraordinary ordered droplet chains. As shown in Fig. 4.3(c), drop coalescence takes place in the middle of the channel at a later time and the polymer-rich domains continue to coarsen [Fig. 4.3(d)].

In contrast to the phase separation process depicted in Fig. 4.3, the experiments of Loudet, Barois, and Poulin [32] show that the coarsening is arrested once the droplets reach a critical size, so that the chain structure is preserved and stable. This is explained in [32] by the presence of a -1 hyperbolic point defect form between each droplet in a chain, which represents the elastic dipole. As shown in Fig. 4.4, our numerical solution obtains a continuous order parameter S without any singularity shows up. In addition, the entire domain is nearly uniaxial with biaxiality parameter $\beta(Q)$ is closed to zero. Therefore, there is no indication of orientational defects in our result. In the absence of defect, there is no mechanism to stop the coarsening of the polymer-rich droplets and eventually the chain structure ordering is destroyed.

4.3.2   Effect of Elastic Energy

We want to check the effect of the elastic energy, which critically decides the distortion of the directional field and further influence the formation of the structure. Fig. 4.5 shows the evolution with a weak elastic energy strength $K = 0.001$ at $t = 500, 1000, 1500, 12000$, respectively. With this smaller elastic energy, the initial LC-rich layer still appears besides the wall in (a), as we have also observed with $K = 0.004$. However, the distortion penalty is not strong enough to force the directional field aligns homogeneously along the wall before nucleation starts. After the nucleation starts in (b),

droplets appear throughout the entire domain without any order, and the director field
is distorted by the surface anchoring. After a long time of running, the droplet size grows
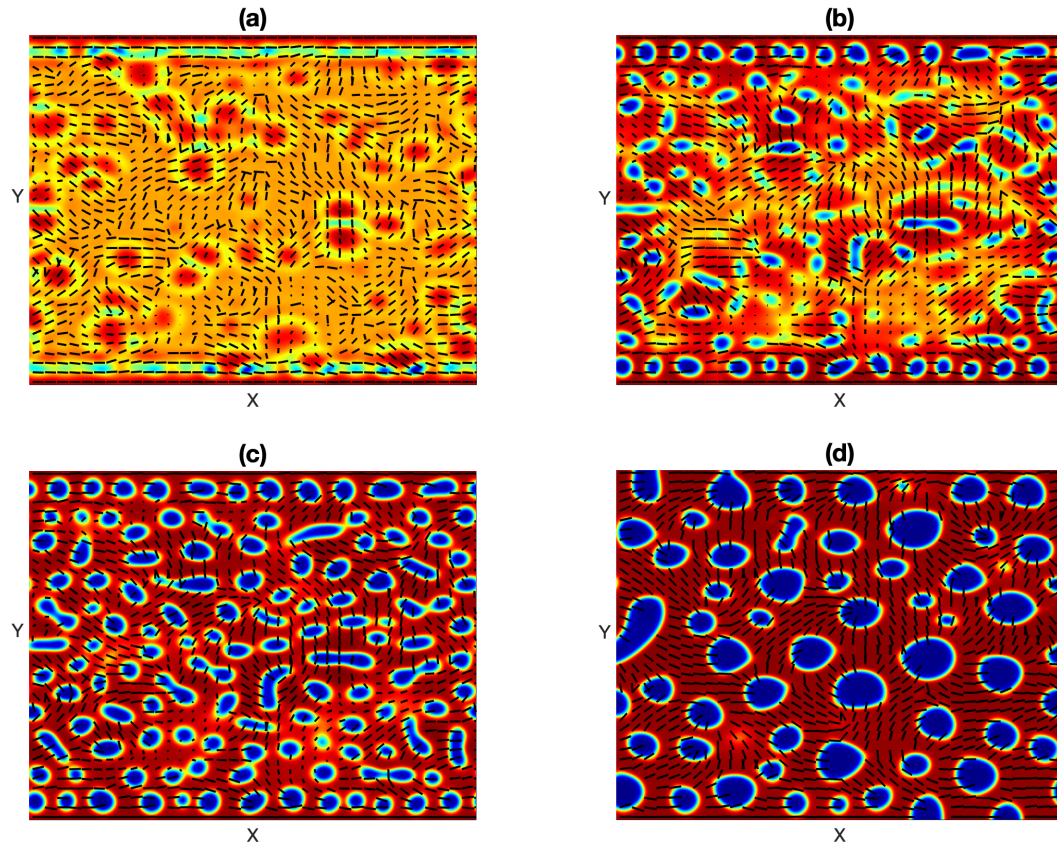with coalescence and there is no order found in the director field.

Figure 4.5: Nucleation of isotropic phase with $K = 0.001$ at (a) t=500, (b) t=1000,
(c) t=1500, (d) t=12000.

4.3.3   Effect of Surface Anchoring

We also examine the effect of the surface anchoring strength at the interface between
isotropic phase and nematic liquid crystal phase. Taking the same parameters as in pre-
viously discusses case but with different anchoring energy at the interface. Fig. 4.6 shows
snapshots of the planar interface anchoring with $W = 0.03$, no interface anchoring with

$W = 0$ at step $t = 4500$. As we can see, the droplets tend to be elongated horizontally or vertically to increase the interface area and adapt to the preferential surface anchoring, and the finger-like regions are formed, which are different from what we captured in Fig. 4.3.
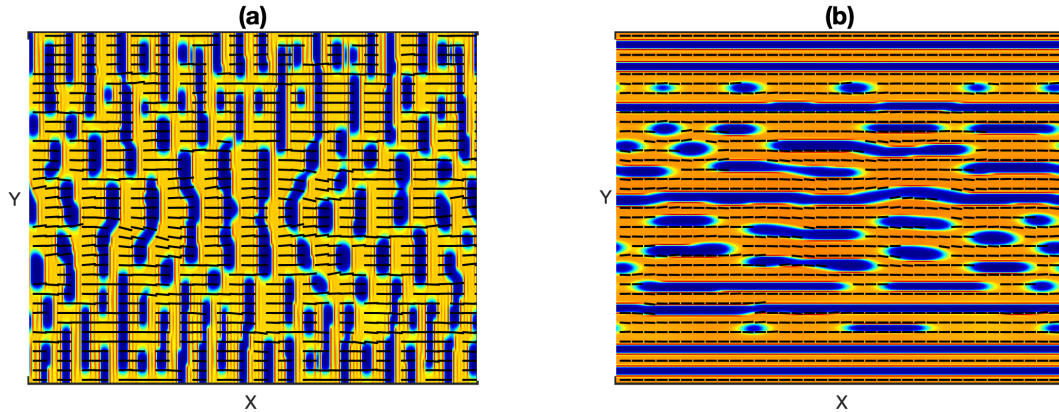

Figure 4.6: (a) and (b) plots the volume fraction associated with subsampled director field with $W = -0.02$, 0.03, which represents strong homeotropic anchoring/planar anchoring at the interface, respectively. The step $t = 4500$. Isotropic fluid phase in blue.

Also, it is worth noting that the mixing energy strength plays a critical role to the formation of the droplets structure. With dominant mixing energy, the dynamic behaves like Cahn-Hilliard type separation that the droplets coalescence at an earlier stage with preserved round-like shape. However, with smaller mixing energy, the droplets tend to be elongated horizontally or vertically to accommodate with the anchoring condition at the interface of the droplets. Our model restricts the ratio between anchoring energy strength W with mixing energy strength λ to be relatively small in order to maintain the well-postedness of the differential equation (3.13). Therefore, we can not introduce a strong anchoring at the interface, and a proper mixing energy strength is significant to obtain the chain-like structure with round-shaped particle without much deformation.

4.3.4   Lamellae Order

We consider next the same set-up as before, an initial mean polymer volume fraction of $\phi = 0.4$, but now the LC in the mixture is initially in isotropic phase. Such state is obtained by changing the thermotropic energy coefficients to $a = 80$, $B = -10$, $C = 160$, which with $\phi = 0.4$ give $S_{eq} = 0$. All the other parameters remain the same (Set 2 in Table 3.1). As before, the wall anchoring remains planar. We consider first homeotropic surface anchoring. Figure 4.7 shows snapshots of the phase separation process in the 2D channel. At early times [Fig. 4.7(a)] a layer of LC-rich material develops adjacent to the each wall, just as in the chain structure nucleation case, but now these first LC-rich layers are accompanied by equal polymer-rich layers. As initial isotropic binary mixture phase-separates at the walls, the strong anchoring there induces the lamellae. A similar appearance of phase-separated layers adjacent to walls has been observed in a thin film of a polymer blend [71], a diblock copolymer [72], and a polymer dispersed nematic [6] when they were confined between two walls. As Fig. 4.7(a) shows, these layers drastically modify the orientational field, turning it vertically aligned to comply with the homeotropic surface anchoring preference, a significant distance from the walls. This orientational distortion favors the formation of more lamellae [Fig. 4.7(b)], which alternate in polymer-rich and LC-reach composition, and propagate from the walls in to fill the entire channel [Fig. 4.7(c)(d)]. Once this occurs the system is in equilibrium and the lamellae will not coarsen, in striking contrast to what happens in spinodal decomposition of a binary isotropic mixture (as modeled by the Cahn-Hilliard equation).

To have a more explicit understanding of the pattern, we also monitored the evolution of the energies and related them with the formation of the system structures. As shown in Fig. 4.8, the total free energy is decreasing coordinately while the layers are forming and propagating, and it reaches to the minimum when the equilibrium configuration is
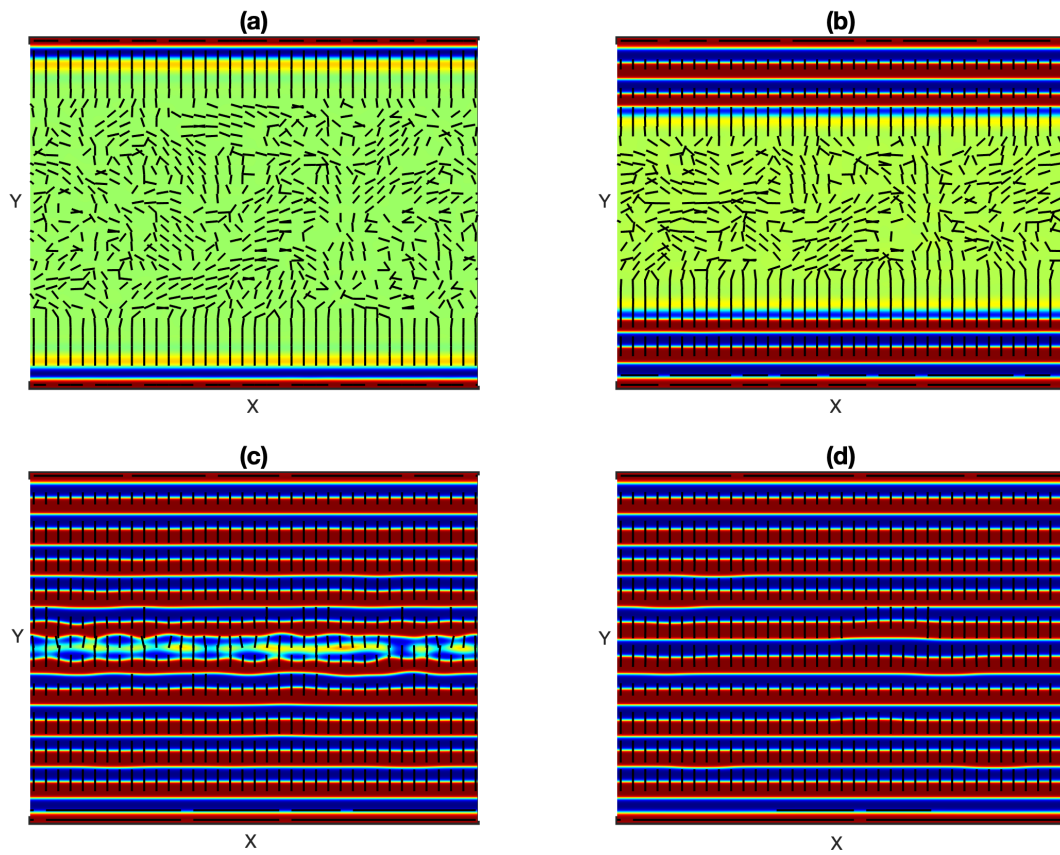
Figure 4.7: *From top left to bottom right* Time sequence of the volume fraction ϕ and the subsampled director field for isotropic lamellae in a nematic liquid crystal phase at $t = 500, 1500, 3500, 12000$ with $a = 80$, $B = -10$, $C = 160$, $W = -0.01$. Nematic phase in red and isotropic fluid phase in blue.
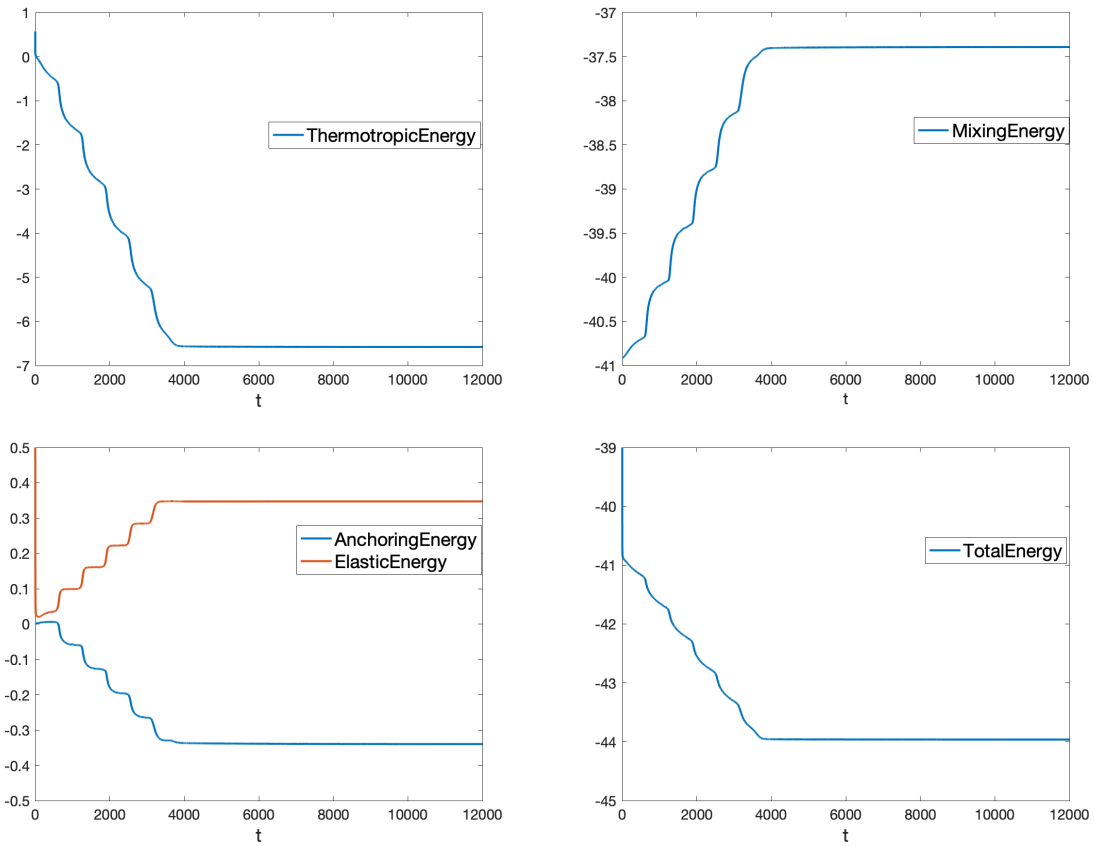
Figure 4.8: *From left to right* The evolution of the anchoring energy, elastic energy and total free energy in the domain for the lamellae case.

formed. It is the thermotropic energy which keeps decreasing and initiates the formation of the structure. The anchoring energy and elastic energy at the interface tend to balance with each other, which also contributes to the structure. Again, we provide the order parameter S and biaxiality $\beta(Q)$ at Fig. 4.9. There is no indication of defect since S contains no singularities. The confinement walls introduce two lines of biaxial region besides the wall.

Surface anchoring plays a crucial role in the formation of lamellae from an initially isotropic mixture such as the one just considered (parameter Set 2 in Table 3.1). If we choose planar surface anchoring, as shown in Fig. 4.10, the system phase separates into lamellae growing from the walls inward, just as with homeotropic anchoring. However,
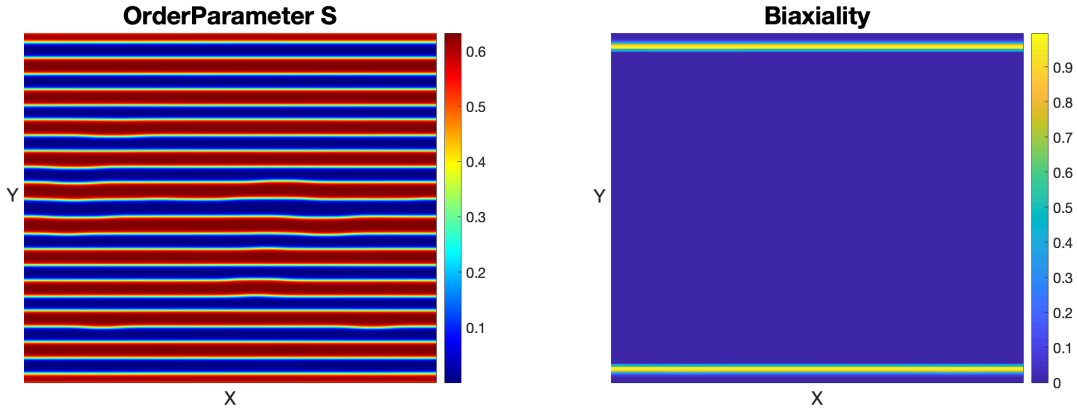
Figure 4.9: The left and right plots are the order parameter S and biaxiality $\beta(Q)$ taken at $t = 12000$.

the orientational field undergoes a very different distortion that the orientational field aligns along the surface of the polymer to match the planar anchoring requirement. If we do not impose anchoring at the surface of isotropic particle, the result becomes quite different. As evident in Fig. 4.11, the director field is still homogeneous planar to adapt to the strong wall anchoring, however, without surface anchoring, the layers are thicker than before and produce a distorted region when the top and bottom regions catch up with each other, as shown in (b) and (c). It then takes 10^5 steps to straighten the region and obtain a final lamellae, which is not equally spaced in the region. This indicates that the surface anchoring, no matter planar or homeotropic, help stabilize the lamellae configuration.

4.4 Elastic Dipole

The elastic dipole is characterized by a -1 hyperbolic point defect accompanied with the $+1$ radial droplet defect. Since the dipole is critical to the formation of highly self-assembly phenomenon, we want to investigate it using our model. It is difficult to capture the appearance of defect when numerous particles nucleate from temperature quenching.
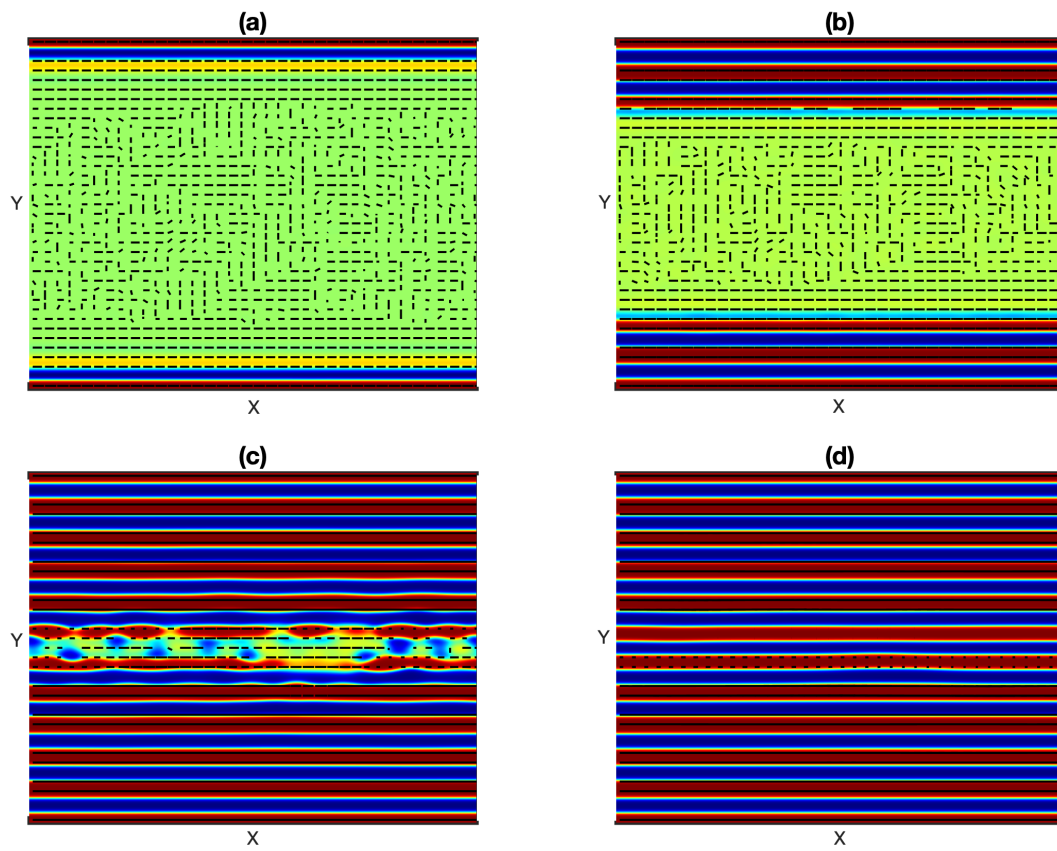
Figure 4.10: Time sequence of the polymer volume fraction ϕ and the subsampled director field for the phase separation of a polymer-LC mixture where the LC component is initially in isotropic state (thermotropic energy parameters $a = 80$, $B = -10$, $C = 160$) with planar surface anchoring $W = 0.01$ at (a) $t = 500$, (b) $t = 1500$, (c) $t = 3500$, (d) $t = 12000$. LC-rich phase is in red and polymer-rich phase is in blue.
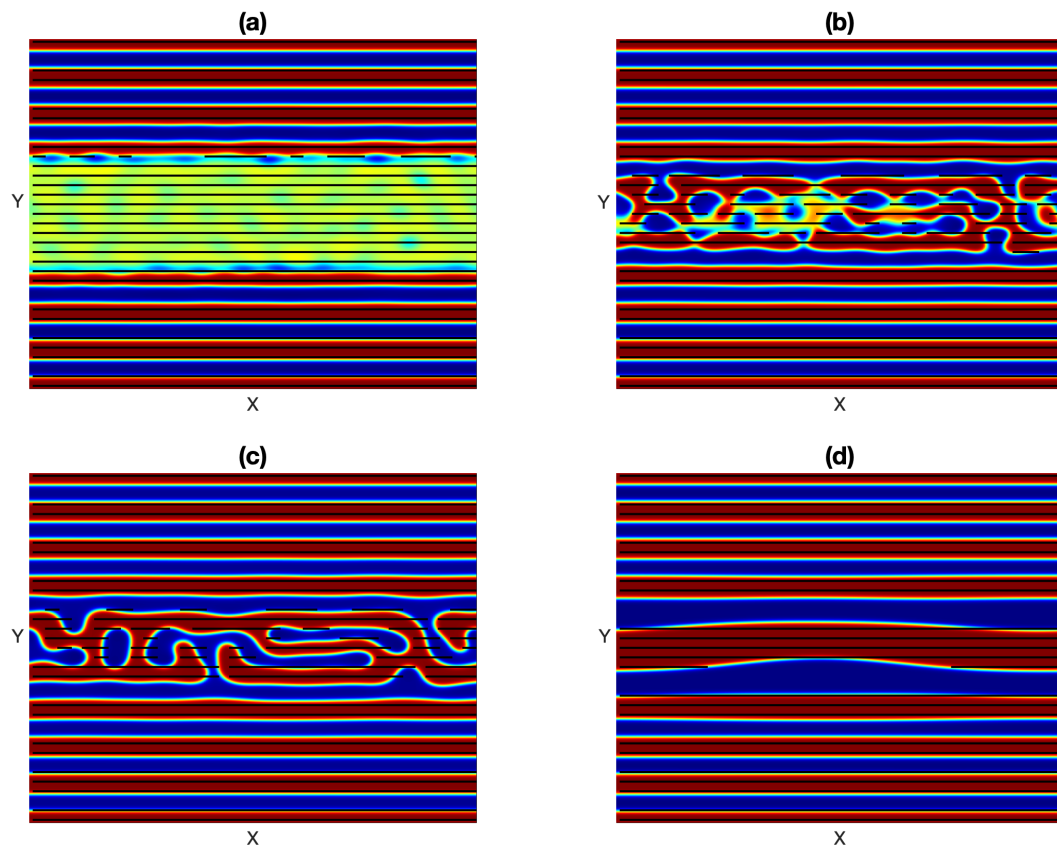
Figure 4.11: Time sequence of the polymer volume fraction ϕ and the subsampled director field for the phase separation of a polymer-LC mixture where the LC component is initially in isotropic state (thermotropic energy parameters $a = 80$, $B = -10$, $C = 160$) without surface anchoring $W = 0$ at (a) $t = 3000$, (b) $t = 4000$, (c) $t = 5000$, (d) $t = 130,000$. LC-rich phase is in red and polymer-rich phase is in blue.
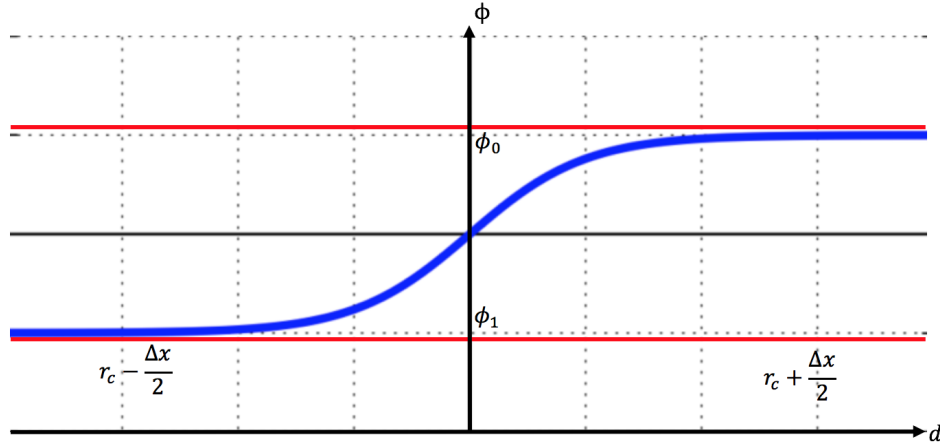
Figure 4.12: Graph of volume fraction ϕ as a function of distance distance d to the center of the particle.

However, it is feasible to start with an initial configuration which is close to dipole, and governing its evolution with the same system (3.13).

4.4.1   One Droplet

We consider the simplest case that a single droplet of polymer is dispersed in a nematic matrix with an orientational field that approximately corresponds to a dipole.

Assume the volume fraction $\phi = \phi_0$ outside the droplet and $\phi = \phi_1$ inside the droplet, whose value are taken as the local minimum of the mixing energy potential f_{mix}. Set $T = 1.3$, then $\phi_0 = 0.27$, $\phi_1 = 0.72$. To make a smooth variation of ϕ through the interface, we define $\phi(x)$ using hyperbolic function as below,

$$\phi(x) = \phi_0 + \frac{\phi_1 - \phi_0}{1 + \exp(\dfrac{12}{\Delta x}(d - r_c))}, \tag{4.3}$$

where r_c is the radius of the droplet, Δx is the thickness of the interface, and $d = ||\mathbf{x} - \bar{\mathbf{x}}||$ is the Euclidean distance between the position $\mathbf{x}$ with the center of the droplet $\bar{\mathbf{x}}$.

The order parameter S is set the same way:

$$S(x) = S_0 + \frac{S_1 - S_0}{1 + \exp(\frac{12}{\Delta x}(d - r_c))}, \tag{4.4}$$

where $S \sim S_1 = 0$ inside the droplet, and $S \sim S_0$ outside the droplet, which is estimated by (2.35).

Based on the plot of the hyperbolic function in Fig. 4.4.1, we find that,

$$d \geq r_c + \Delta x/2, \quad -x \geq 6, \quad \phi \to \phi_0, \quad S \to S_0,$$

$$d \leq r_c - \Delta x/2, \quad -x \leq -6, \quad \phi \to \phi_1, \quad S \to S_1.$$

To define the director field $\mathbf{n}$, we artificially make it to be close to a elastic dipole,

$$\mathbf{n} = (1, 0, 0) - Pr_c^2 \frac{\mathbf{x} - \overline{\mathbf{x}}}{d^3}, \tag{4.5}$$

where P is a constant which determines the initial position of the -1 point defect, here we choose $P = 2.08$.

We set the parameters $a = 5.528$, $B = -71.55$, $C = 87.58$, $\lambda = 0.004$, $K = 0.002$, $W = -0.0015$, and Fig. 4.13 shows the experiment result, where the left plots represent the initial volume fraction accompanied with subsampled director field, the order parameter S and the biaxiality parameter $\beta(Q)$. Apparently that the initial configuration is close to dipole, with a hyperbolic hedgehog sits besides the particle. There is a singularity point at the order parameter S which also indicates the defect existence, and the entire region is uniaxial. The right three plots corresponds to $t = 50,000$ with $\Delta t = 0.02$, which shows that the defect splits into two $-1/2$ defects, continuously moved away from each other, and transformed into quadrupoles. Therefore, the elastic dipole can not be sustained by the model. In addition, the two $-1/2$ defects are surrounded by a ring of
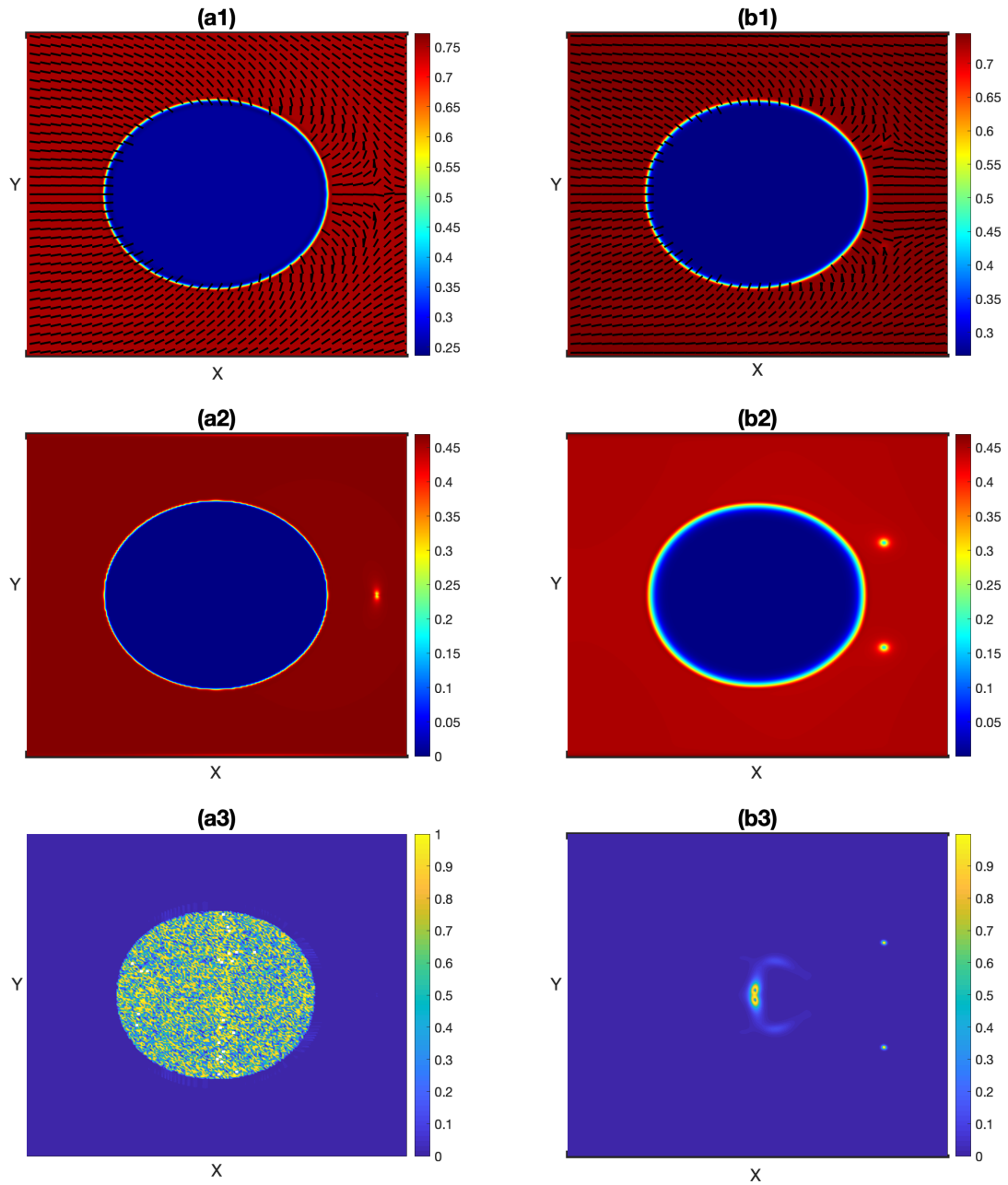
Figure 4.13: The top/middle/bottom plots show the volume fraction ϕ with the sub-smapled director field $\boldsymbol{n}$, the scalar order parameter S, and the biaxiality parameter $\beta(Q)$, respectively. The left plots are the initial setting at $t = 1$ which approximates an elastic dipole with a -1 defect besides the droplet, and the right plots are at $t = 50,000$. The parameters are $a = 5.528$, $B = -71.55$, $C = 87.58$, $\lambda = 0.004$, $K = 0.002$, $W = -0.0015$. LC-rich phase in red and polymer-rich phase in blue.

biaxility region in which the order parameter has a discontinuity. Similar observations have been found that the hedeghog point defect is unstable for large droplet radii and low temperatures with Landau-de Gennes model, instead forming a $-1/2$ disclination loop about the particle which is surrounded by a region of biaxiality [50]. Therefore, in the absence of elastic dipole, there is no mechanism in the Landau-de Gennes model to stop the coarsening of the polymer-rich droplets and eventually the chain structure ordering is destroyed, which further explains the result in Section 4.3.1.

4.4.2   Two Droplets Chain

Next we consider the case when there are two droplets align with each other. The initial configuration is defined similarly as above.

$$
\begin{aligned}
\phi_l(x) &= \phi_0 + \frac{\phi_1 - \phi_0}{1 + \exp(\dfrac{12}{\Delta x}(d_1 - r_{c1}))}, \\
\phi_r(x) &= \phi_0 + \frac{\phi_1 - \phi_0}{1 + \exp(\dfrac{12}{\Delta x}(d_2 - r_{c2}))},
\end{aligned}
\tag{4.6}
$$

where d_1 and d_2 are the Euclidean distance between the position $\mathbf{x}$ and the center of the droplet $\mathbf{\bar{x}_1}$ and $\mathbf{\bar{x}_2}$, respectively. The order parameter S is defined coordinately. This describes two particles chain up in the nematic host with radial orientational field around them. Besides each particle there resides a -1 point defect, which represents a dipole.

Apply the same set of parameters with the one particle case, Fig. 4.14 presents the initial structures on the left and the intermediate structures with $t = 10,000$ on the right. Again, the -1 defects open up to two $-1/2$ point defects as before, and we expect that the two droplets will eventually coalescence together. Therefore, the chain ordered structure is not stable in our model.
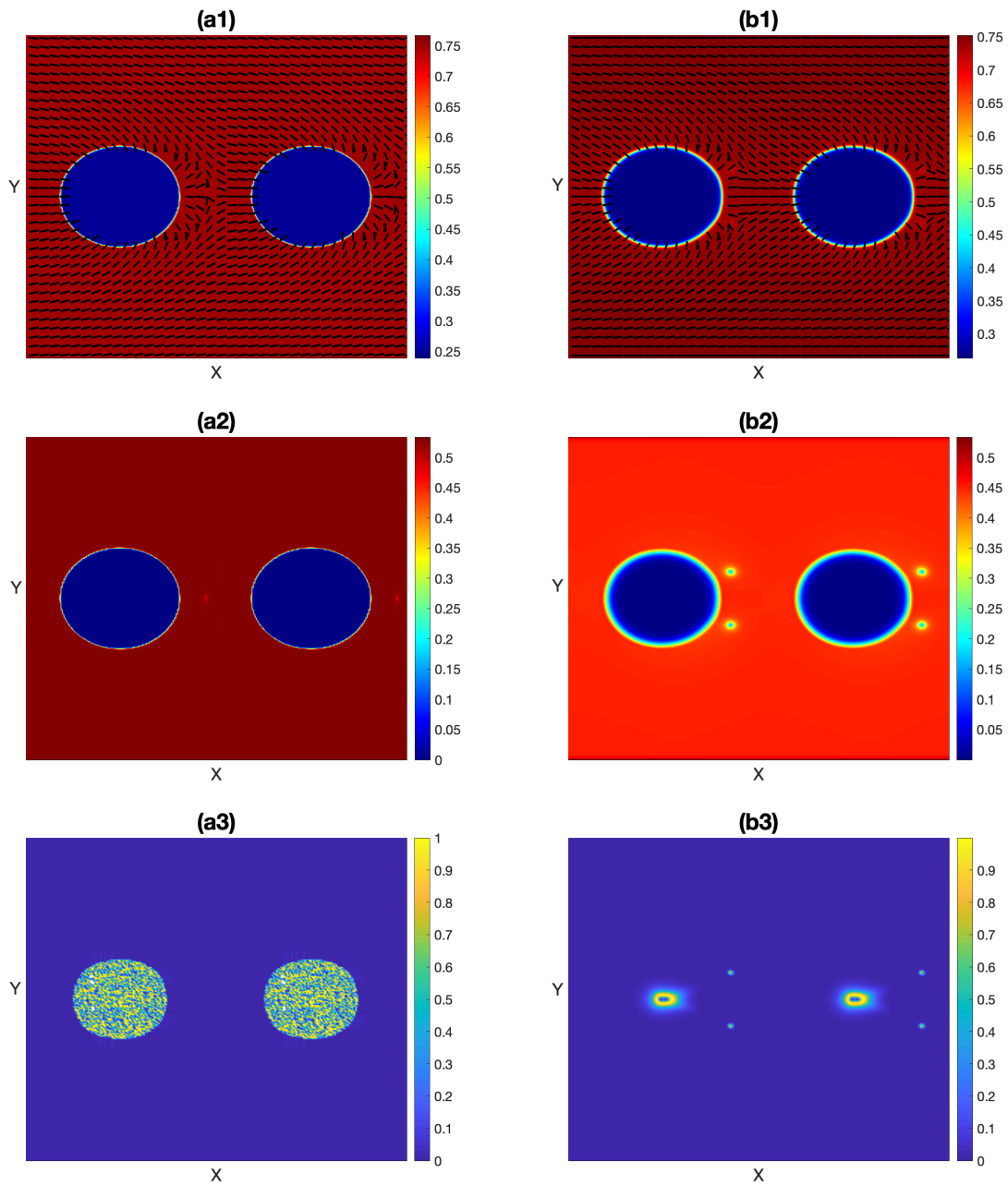
Figure 4.14: The top/middle/bottom plots show the volume fraction ϕ with the sub-smapled director field $\boldsymbol{n}$, the scalar order parameter S, and the biaxiality parameter $\beta(Q)$, respectively. The left plots are the initial setting at $t = 1$ which approximates an elastic dipole with a -1 defect besides the droplet, and the right plots are at $t = 10,000$. The parameters are $a = 5.528$, $B = -71.55$, $C = 87.58$, $\lambda = 0.004$, $K = 0.002$, $W = -0.0015$. LC-rich phase in red and polymer-rich phase in blue.

4.4.3   3D Dipole

The other observations have shown that the hedgehog point defect transits into a $-1/2$ disclination loop about the particle [50], and we instead observed two $-1/2$ point defects in a 2D channel which may reflect a cross-section of the 3D ring defect. Here we verify the formation of disclination loop by exploring further the 3D case.

Apply the same set of parameters with the one particle case in 2D, Fig. 4.15 presents the initial structures on the left and the intermediate structures with $t = 10,000$ on the right. The plot shows the isosurface of volume fraction ϕ, order parameter S and biaxiality parameter $\beta(Q)$. As shown in the plots, the -1 hyperbolic defect opens up to a disclination ring which is surrounded by the biaxial region, as we expected. It is also worth noting that as time goes, the ring continuously grows the radius and moves toward the droplet. Eventually it locates at the surface of the droplet and changes the shape of the droplet. In the same experiment of two droplets dipole chain in 3D, the two droplets again absorb the disclination ring defect, change their shape, and elongate to shrink the distance between the droplets.
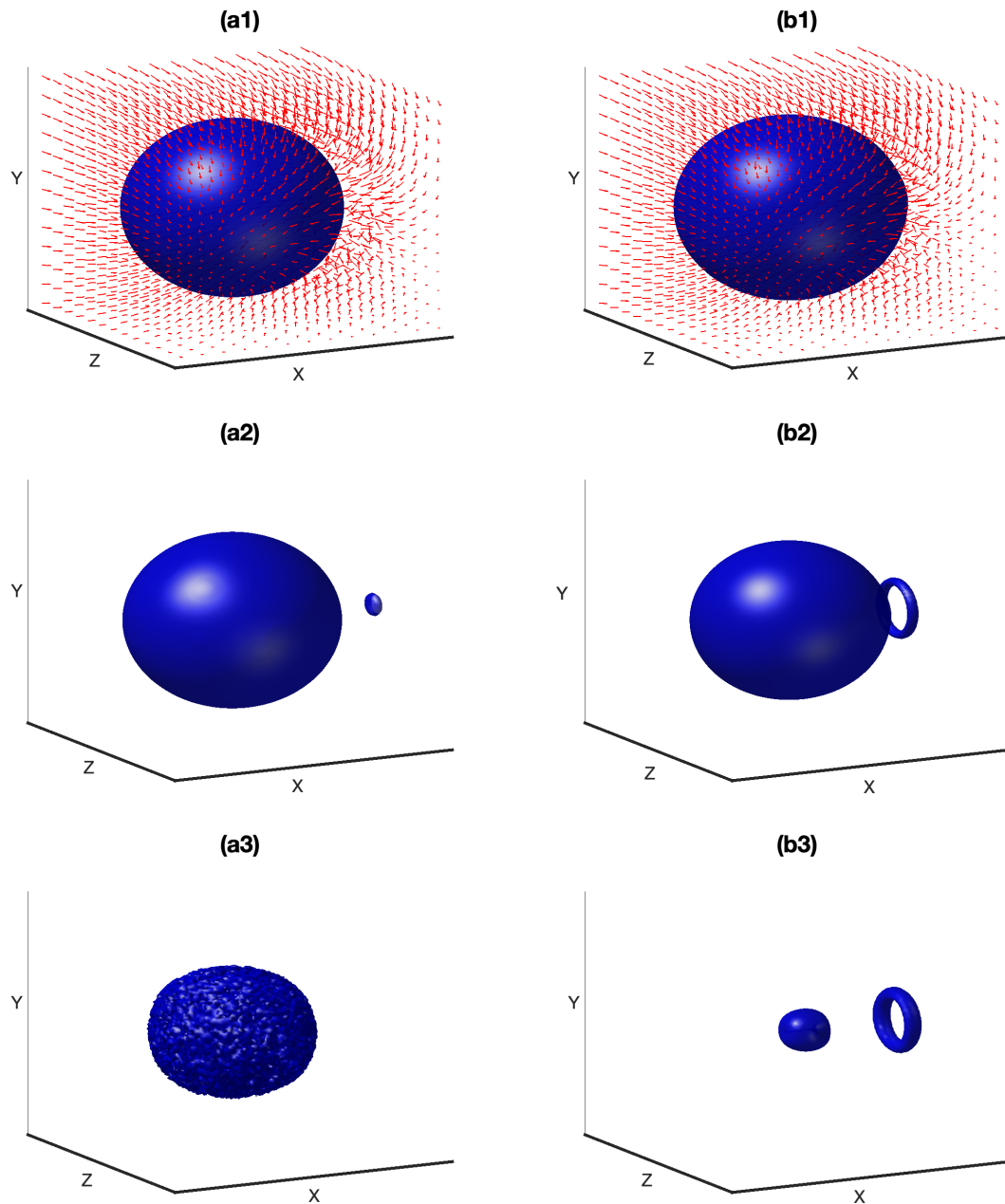
(a1)   **(b1)**

(a2)   **(b2)**

(a3)   **(b3)**

Figure 4.15: The top/middle/bottom plots show the isofurfaces of volume fraction ϕ with the subsmapled director field $\boldsymbol{n}$, the scalar order parameter S, and the biaxiality parameter $\beta(Q)$, respectively. The left plots are the initial setting at $t = 1$ which approximates an elastic dipole with a -1 defect besides the droplet, and the right plots are at $t = 10,000$. The parameters are $a = 5.528$, $B = -71.55$, $C = 87.58$, $\lambda = 0.004$, $K = 0.002$, $W = -0.0015$. XZ plane represents the wall.

Chapter 5

3D Order in Confined Walls

In this Chapter, we present the same simulations as last Chapter but in the 3D channel. Again, various surface anchoring and in-plane anchoring are explored.

5.1   Cahn-Hilliard Equation

As before, we study with the Cahn-Hilliard equation, which only take into account the mixing energy. Subsequently, we explore the effect of the nematic components. Fig. 5.1 shows a time series of the isosurface of volume fraction in the rectangular domain $X = 128$, $Y = 100$, $Z = 128$, where XZ plane locates the walls. (a) represents the initial state in which the mixture is slightly perturbed with uniform distribution around $\phi = 0.4$. After that, there is diffusion of ϕ at (b), and the minority phase starts to nucleate at (c), and keeps growing the size by coalescence at (d). The result is similar with what we observed in 2D case.
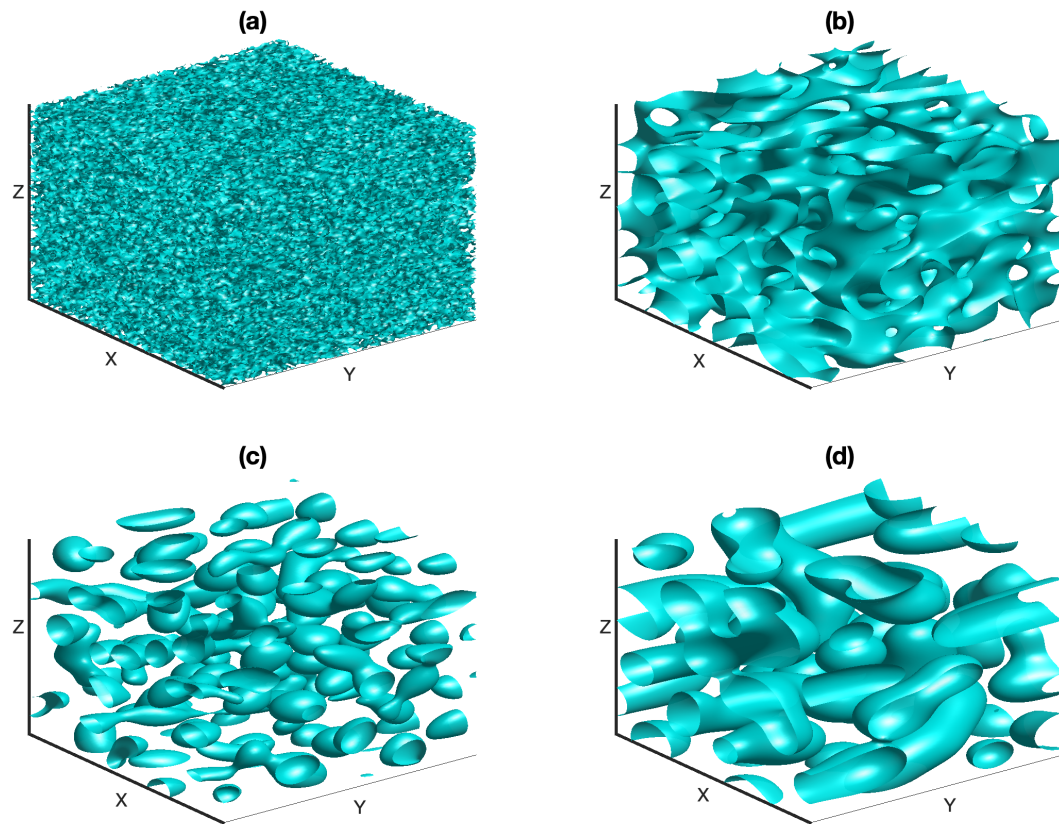
Figure 5.1: *From left to right* phase separation evolution at steps $t = 1$, 2000, 4000, 10000 for 3D Cahn-Hilliard equation containing mixing energy only. The quenching temperature $T = 1.3$, capillary length $\epsilon = \dfrac{\Delta x}{2}$.

5.2   Cylindrical Order

In this section, we take the nematic effect into account and present the morphology found in 3D nucleation with various interface and wall anchoring conditions. By retaining the same set of parameters as the 2D droplet chain order case, we investigate the same system but in a 3D channel. The relevant physical parameters and the initial condition are the same as in the 2D channel discussed in last Chapter, and homeotropic surface anchoring is chosen. The wall anchoring is again planar but now we consider two different orientations: 1) aligned with the x-axis, and 2) aligned at a 45 degree angle between the x and z axes. Fig. 5.2 displays isosurfaces of polymer volume fraction ϕ and a subsample of the director field at time $t = 1100$, 3500 for the planar wall anchoring 1) and 2). Again, there is first a LC-rich region enriched besides the walls, then the orientational order induced by the wall anchoring and the favored homeotropic surface anchoring produce chains of elongated cylinders of polymer-rich mate rial instead of droplets, in contrast to the 2D case.

As seen in the bottom two plots in Fig. 5.2, wall anchoring controls the orientation of these chain structures, which now align at a 45 degree angle between the x and z axis. The nucleation of perfectly ordered layers of polymer-rich cylinders takes place, just as in the 2D counterpart, from the walls inward, until coarsening and coalescence destroy the order.

Even though homeotropic surface anchoring is more prevalent in these systems than the planar one, we consider latter to examine its effects on the nucleated morphology. Fig. 5.3 shows that again polymer-rich cylinders are nucleated but now the axis of these cylinders is oriented in the the direction of the wall anchoring. It is important to note that just as in the 2D case, the wall anchoring quickly produces a layer of LC-rich material adjacent to the walls at which the nucleation of the first cylinder layers begins.
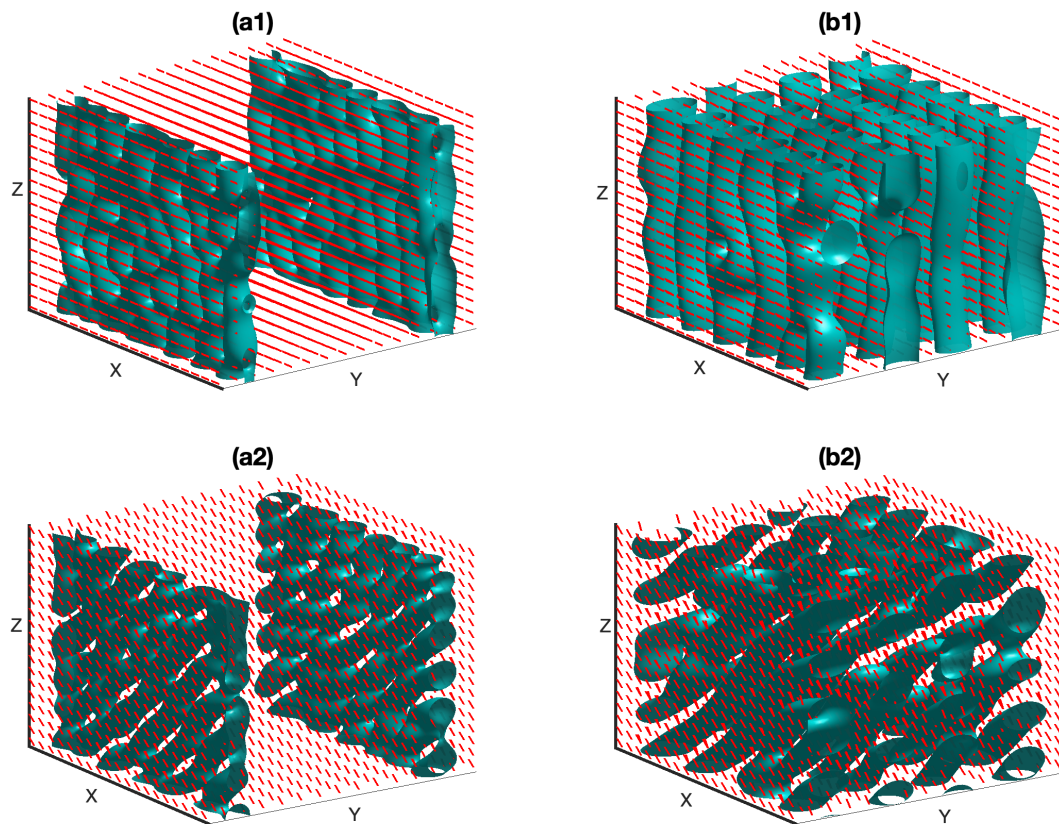
Figure 5.2: The top (bottom) two plots show isosurfaces and a sample of the director field at $t = 1100$ (left) and $t = 3500$ (right) when the wall anchoring is along the x axis (top) and at a 45 degree angle (bottom). The surface anchoring is homeotropic and the thermotropic energy parameters are $a = 5.528$, $B = -71.55$, $C = 87.58$.
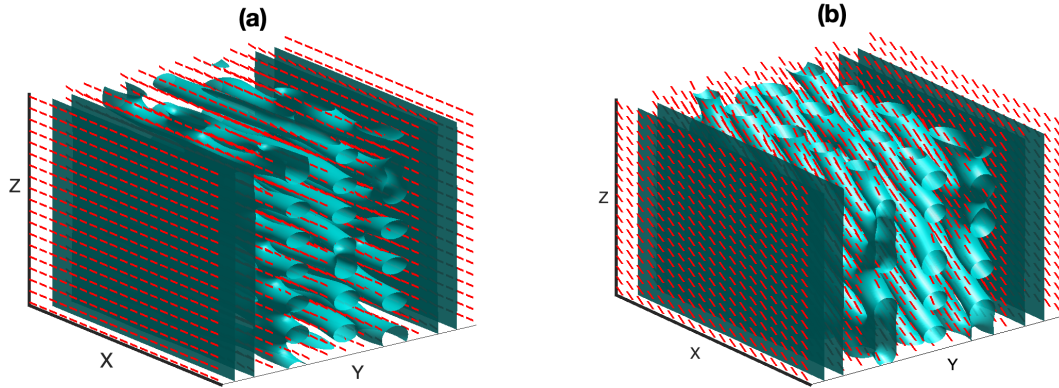
Figure 5.3:   Isosurfaces and a sample of the director field for nucleation with planar surface anchoring and planar wall anchoring along the (a) x direction and (b) in a 45 degree angle between the x and z axes. The time step is t $= 3500$. The thermotropic energy parameters are $a = 5.528$, $B = -71.55$, $C = 87.58$.

5.3   Lamellae Order

Again, we investigate the case for $a = 80$, $B = -10$, $C = 160$, and set the other parameters to be unchanged as above. In the 3D channel, the phase separation and the formation of lamellae follows the same dynamics as the 2D case. Fig. 5.3 presents isosurfaces of the polymer volume fraction and a subsampled director field at two different times for both wall anchoring aligned with the x axis and at a 45 degree angle between the x and z axis. The surface anchoring is homeotropic. As in the 2D case, once the phase-separated layers cover the entire channel, the system reaches an equilibrium and coarsening is arrested. Fig. 5.3 changes the anchoring at the surface of the particles to be planar. Like before, the director field are fully controlled by the interface anchoring and the strong long-range wall anchoring.
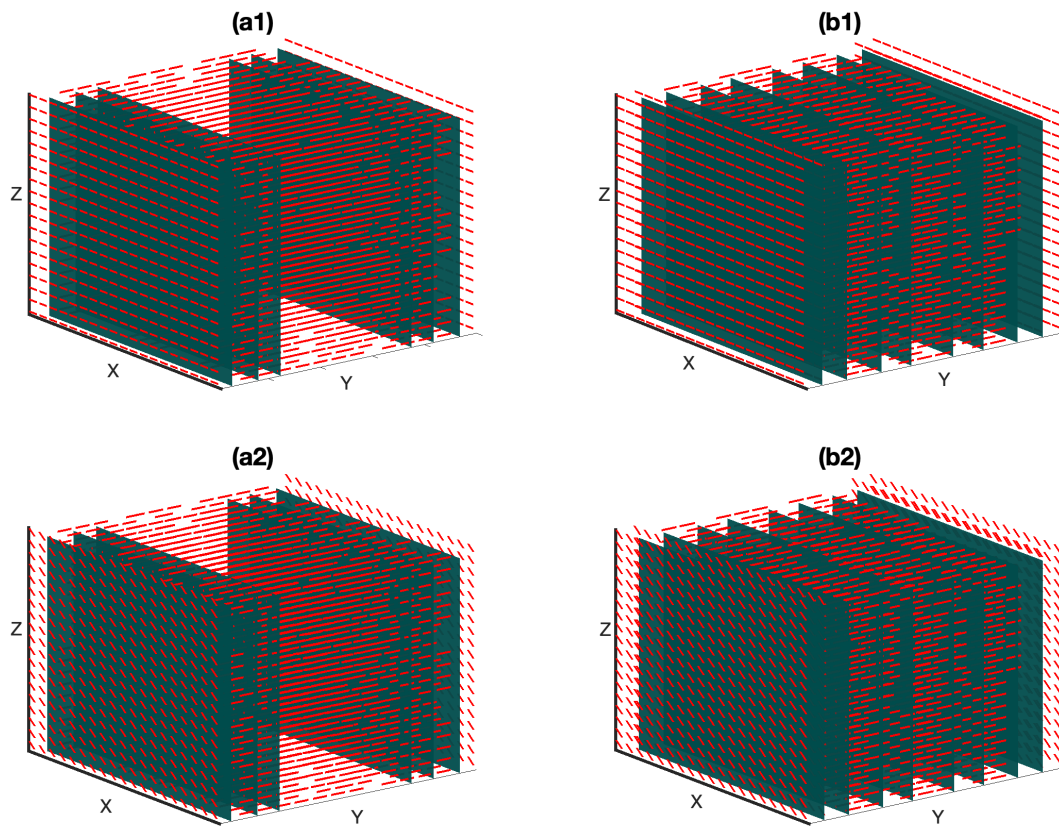
Figure 5.4: The top (bottom) two plots show isosurfaces of ϕ and a sample of the director field at $t = 500$ (left) and $t = 3500$ (right) when the wall anchoring is along the x axis (top) and at a 45 degree angle (bottom). The surface anchoring is homeotropic and the thermotropic energy parameters are $a = 80$, $B = -10$, $C = 160$.
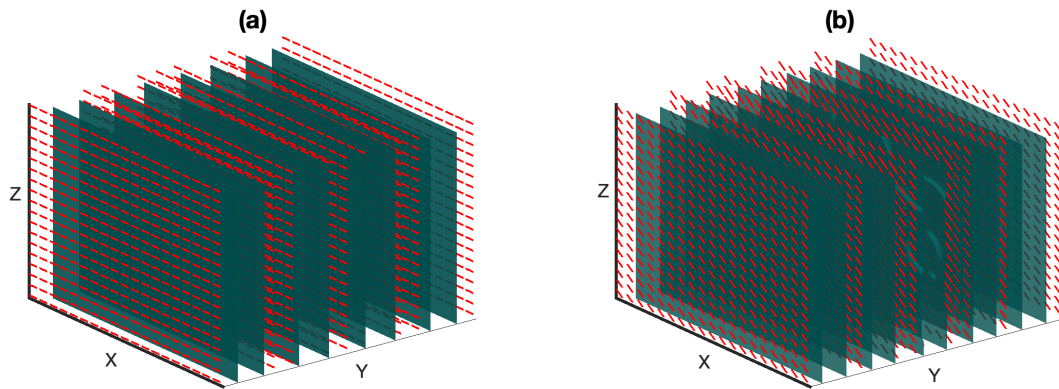
Figure 5.5: Isosurfaces and a sample of the director field for nucleation with planar surface anchoring and planar wall anchoring along the (a) x direction and (b) in a 45 degree angle between the x and z axes. The time step is t $= 3500$. The thermotropic energy parameters are $a = 80$, $B = -10$, $C = 160$.

Chapter 6

Conclusion

We have presented a numerical investigation, both in 2D and 3D, of the ordering and structure formation of a polymer nucleating in a LC continuous phase induced from temperature quenching. The polymer-LC system is confined between two parallel walls which are rubbed and coated to provide the strong planar long-range wall anchoring. Both homeotropic and planar surface anchoring are considered at the polymer-LC interface. The model is the Ginzburg-Landau theory for the conserved composition density ϕ, which represents the volume fraction of the polymer, and the non-conserved nematic tensor order parameter Q, which describes the orientation of the rigid rod-like nematic molecules. To our knowledge, this is the first 3D numerical investigation of nucleation in a confined geometry. Our study demonstrates that the presence of the nematic liquid crystal has profound effect on the morphology of nucleation of the minority phase. Moreover, the long-range wall anchoring and surface anchoring dramatically affect the orientation of the ordered structures. With certain set of parameters, remarkable polymer-rich domain chain structures are observed when quenching from the nematic initial state in both the 2D and 3D channel. However, there is no apparent mechanism in this Landau-de Gennes model to arrest the coarsening of the polymer-rich domains and eventually the chain

structure order is destroyed. As argued in [32], the highly ordered array of monodisperse droplet chains observed in experiments is preserved and stable during phase separation because of the formation of elastic dipole, which is characterized by -1 topological point defects formed in between the $+1$ radial droplet defects. However, we show with a numerical example that the -1 point defect opens up to two $-1/2$ point defects in 2D, and a $-1/2$ disclination ring in 3D, or equivalently, the dipoles cannot be sustained and eventually transits to quadrupoles in the Landau-de Gennes model. The use of variable mobility that depends on both Q and ϕ might provide a mechanism to arrest or slow down the coarsening once the ordered structures have formed.

We also find a stable lamellae order when quenching from isotropic phase. The system reaches equilibrium with alternating polymer-rich and LC-rich layers, and the coarsening is arrested. While the model considered here has limitations, the results reveal the strong effects that the orientational order induced by the presence of a liquid crystal component and by anchoring can have on nucleation and phase separation, and underlines a potential mechanism for controlling morphology in this type of binary systems.

Bibliography

[1] P. D. Gennes, *The physics of liquid crystals.* Oxford, Clarendon Press, 1974.

[2] M.Mata, C.J.García-Cervera, and H. D. Ceniceros, *Ordering kinetics of a conserved binary mixture with a nematic liquid crystal component*, J. Non-Newtonian Fluid Mech. **212** (2014) 18–27.

[3] R. Nós, A. Roma, C. García-Cervera, and H. Ceniceros, *Three-dimensional coarsening dynamics of a conserved, nematic liquid crystal-isotropic fluid mixture*, J. Non-Newtonian Fluid Mech. **248** (2017) 62–73.

[4] M. Motoyama, H. Nakazawa, T. Ohta, T. Fujisawa, H. Nakada, M. Hayashi, and M. Aizawa, *Phase separation of liquid crystal-polymer mixtures*, Comput. Theor. Polym. Sci. **10** (2000), no. 3-4 287–297.

[5] H. Nakazawaa, S. Fujinami, M. Motoyama, T. Ohta, T. Araki, H. Tanaka, T. Fujisawa, H. Nakada, M. Hayashi, and M. Aizawa, *Phase separation and gelation of polymer-dispersed liquid crystals*, Comput. Theor. Polym. Sci. **11** (2001), no. 6 445458.

[6] J. Xia, J. Wang, Z. Lin, F. Qiu, and Y. Yang, *Phase separation kinetics of polymer dispersed liquid crystals confined between two parallel walls*, Macromolecules **39** (2006), no. 6 2247–2253.

[7] Y. J. Jeon, Y. Bingzhu, J. Rhee, D. Cheung, and M. Jamil, *Application and new developments in polymer-dispersed liquid crystal simulation studies*, Macromol. Theory Simul **16** (2007), no. 7 643–659.

[8] A. Matsuyama and R. Hirashima, *Phase separations in liquid crystal colloid mixtures*, J. Chem. Phys. **128** (2008), no. 4 044907.

[9] S. Bronnikov, S. Kostromin, and V. Zuev, *Thermally induced isotropic-nematic phase separation in mixtures of low-molecular weight and polymer liquid crystals*, Soft Mater. **11** (2013), no. 1 6–12.

[10] S. Bronnikov, C. Racles, and V. Cozan, *Kinetics of the nematic phase growth across the isotropic-nematic phase transition in polymerdispersed liquid crystals*, Liq. Cryst. **36** (2009), no. 3 319–328.

[11] C. Muratova and W. E, *Theory of phase separation kinetics in polymerliquid crystal systems*, J. Chem. Phys. **116** (2002), no. 11 4723.

[12] E. Soulé, N. Abukhdeir, and A. Rey, *Thermodynamics, transition dynamics, and texturing in Polymer-Dispersed Liquid Crystals with Mesogens exhibiting a direct isotropic/smectic-A transition*, Macromolecules **42** (2009), no. 24 94869497.

[13] A. Lapena, S. Glotzer, S. Langer, and A. Liu, *Effect of ordering on spinodal decomposition of liquid-crystal/polymer mixtures*, Phys. Rev. E **60** (1999), no. 1 R29.

[14] E. Soulé and A.D.Rey, *Modelling complex liquid crystal mixtures: from polymer dispersed mesophase to nematic nanocolloids*, Phys. Rev. Lett. **112** (2014), no. 22 225501.

[15] A. Matsuyama, *Nematic Ordering in Mixtures of Polymers and Liquid Crystals*, Res. Rep. Fac. Eng. Mie Univ. **27** (2002) 9–22.

[16] A. Bray, *Theory of phase-ordering kinetics*, Adv. Phys. **43** (1994), no. 3 357–459.

[17] A. Bray, *Coarsening dynamics of phase-separating systems*, Philos. Trans. R. Soc., A **361** (2004), no. 1805 781–792.

[18] P. Drzaic, *Liquid Crystal Dispersions*, vol. 1. World Scientific: Singapore, 1995.

[19] P. Drzaic, *Putting liquid crystal droplets to work: a short history of polymer dispersed liquid crystals*, Liq. Cryst. **33** (2006), no. 11-12 12811296.

[20] J. Lyu, H. Kikuchi, D. Kim, J. Lee, K. Kim, H. Higuchi, and S. Lee, *Phase separation of monomer in liquid crystal mixtures and surface morphology in polymer-stabilized vertical alignment liquid crystal displays*, J. Phys. D: Appl. Phys. **44** (2011), no. 32 325104.

[21] F. Ahmad, M. Jamil, L. Woo, and Y. Jeon, *The investigation of molecular affinity involved in poly(ethylene glycol)-based polymer-dispersed liquid crystal display*, Colloid Polym. Sci. **290** (2012), no. 7 599606.

[22] H. Kakiuchida, M. Tazawa, K. Yoshimura, and A. Ogiwara, *Optical diffractometry of highly anisotropic holographic gratings formed by liquid crystal and polymer phase separation*, Phys. Rev. E **86** (2012), no. 6-1 061701.

[23] R. Shanks and D. Staszczyk, *Thermal and optical characterization of polymerdispersed liquid crystals*, Int. J. Polym. Anal. **2012** (2012) 767581.

[24] J.-D. Cho, S.-S. Lee, S.-C. Park, Y.-B. Kim, and J.-W. Hong, *Optimization of LC droplet size and electro-optical properties of acrylate-based polymer-dispersed liquid crystal by controlling photocure rate*, J. Appl. Polym. Sci. **130** (2013), no. 5 30983104.

[25] R. Deshmukh and M. Malik, *Effect of dichroic dye on phase separation kinetics and electro-optical characteristics of polymer dispersed liquid crystals*, J. Phys. Chem. Solids **74** (2013), no. 2 215224.

[26] M. Ellahi, F. Liu, P. Song, Y. Gao, H. Cao, M. Rafique, M. Khaskheli, M. Z. Iqbal, and H. Yang, *Influence of the multi-functional epoxy monomers structure on the electro-optical properties and morphology of polymer-dispersed liquid crystal films*, Polym. Bull. **70** (2013), no. 11 29672980.

[27] J.-H. Lee and T.-H. Yoon, *Effect of the surface affinity of liquid crystals and monomers on the orientation of polymer-dispersed liquid crystal*, Jpn. J. Appl. Phys. **52** (2013), no. 9R 091702.

[28] S.-L. Hou, W.-K. Choi, and G.-D. Su, *Ultra-bright heads-up displays using a method of projected color images by combination of LEDs and polymer-dispersed liquid crystals*, J. Disp. Technol. **10** (2014) 228234.

[29] P. Yue, J. Feng, C. Liu, and J. Shen, *A diffuse-interface method for simulating two-phase flows of complex fluids*, J. Fluid Mech. **515** (2004) 293317.

[30] P. Hohenberg and B. Halperin, *Theory of dynamic critical phenomena*, ReV. Mod. Phys. **49** (1977) 435.

[31] A. Liu and G. F. Fredrickson, *Phase Separation Kinetics of Rod/Coil Mixtures*, Macromolecules **29** (1996) 8000.

[32] J.-C. Loudet, P. Barois, and P. Poulin, *Colloidal ordering from phase separation in a liquid-crystalline continuous phase*, Nature (2000), no. 407 611613.

[33] P. Poulin, H. Stark, T. Lubenski, and D. Weitz, *Novel colloidal interactions in anisotropic fluids*, Science **275** (1997), no. 5307 1770–1773.

[34] N. Silvestre, Q. Liu, B. Senyuk, I. Salyukh, and M. Tasinkevych, *Towards template-assisted assembly of nematic colloids*, Phys. Rev. Lett. **112** (2014), no. 22 225501.

[35] H. Stark, *Physics of colloidal dispersions in nematic liquid crystals*, Phys. Rep. **351** (2001), no. 6 387–474.

[36] J. Loudet, P. Barois, P. Auroy, P. Keller, H. Richard, and P. Poulin, *Colloidal Structures from Bulk Demixing in Liquid Crystals*, Langmuir **20** (2004), no. 26 11336–11347.

[37] R. Trivedi, M. Tasinkevych, and I. Smalyukh1, *Nonsingular defects and self-assembly of colloidal particles in cholesteric liquid crystals*, Phys. Rev. E **94** (2016) 062703.

[38] C. Zhou, P. Yue, and J. Feng, *Dynamic Simulation of Droplet Interaction and Self-Assembly in a Nematic Liquid Crystal*, Langmuir **24** (2008), no. 7 3099–3110.

[39] T. Porenta, S. Copar, P. Ackerman, M. Pandey, M. Varney, I.I.Smalyukh, and S. umer, *Topological switching and orbiting dynamics of colloidal spheres dressed with chiral nematic solitons*, Sci. Rep. **4** (2014) 7337.

[40] B. Senyuk, Q. Liu, S. He, R. Kamien, R. Kusner, T. Lubensky, and I. Smalyukh, *Topological colloids*, Nature **493** (2013), no. 7431 200205.

[41] S. Alama, L. Bronsard, and X. Lamy, *Minimizers of the Landau-de Gennes energy around a spherical colloid particle*, Arch. Rational Mech. Anal. **222** (2016), no. 1 427450.

[42] M. Ravnik and S. Zumer, *Landaude Gennes modelling of nematic liquid crystal colloids*, Liq. Cryst. **36** (2009), no. 10-11 12011214.

[43] A. Majumdar and A. Zarnescu, *Landau-De Gennes theory of nematic liquid crystals: the Oseen-Frank limit and beyond*, Arch. Ration. Mech. Anal. **196** (2010), no. 1 227280.

[44] A.Sengupta, *Topological Microfluidics, LiquidCrystalTheory:pp7-36*. Springer, Cham, 2013.

[45] P. Flory, *Thermodynamics of High Polymer Solutions*, J. Chem. Phys. **10** (1942) 51–61.

[46] M. Huggins, *Solutions of Long Chain Compounds*, J. Chem. Phys. **9** (1941) 440.

[47] P. G. de Gennes, *Dynamics of fluctuations and spinodal decomposition in polymer blends*, J. Chem. Phys. **72** (1980) 4756.

[48] I. M. Lifshitz, A. Y. Grosberg, and A. R. Khokhlov, *Some problems of the statistical physics of polymer chains with volume interaction*, Rev. Mod. Phys. **50** (1978), no. 3 683–713.

[49] M. Magnuson, B. Fung, and J. Bayle, *On the temperature dependence of the order parameter of liquid crystals over a wide nematic range*, Liq. Cryst. **19** (1995), no. 6 823–832.

[50] S. Mkaddem and E. C. Gartland, *Fine structure of defects in radial nematic droplets*, Phys. Rev. E **62** (2000) 6694 6705.

[51] P. D. Gennes, *The physics of liquid crystals.* Oxford University Press, 1995.

[52] I. Stewart, *The Static and Dynamic Continuum Theory of Liquid Crystals.* Taylor Francis, 2004.

[53] M. Ravnik, *Colloidal structures confined to thin nematic layers.* PhD dissertation, University of Ljubljana, Slovenia, 2009.

[54] H. MORI, E. GARTLAND, J. KELLY, and P. BOS, *Multidimensional Director Modeling Using the Q Tensor Representation in a Liquid Crystal Cell and Its Application to the Cell with Patterned Electrodes,* Jpn. J. Appl. Phys. **38** (1999) 135–146.

[55] G. Chen, H.Takezoe, and A. Fukuda, *Determination of Ki (i=13) and j(j = 26) in 5CB by observing the angular dependence of Rayleigh line spectral widths, Liq. Cryst.* **5** (2006) 341–347.

[56] M. Cleman and C. Williams, *Anchoring energies and the nucleation of surface disclination lines in nematics,* Phil. Mag. **28** (1973) 725–732.

[57] S. Kralj, *Finite-size effects on order reconstruction around nematic defects,* Phys. Rev. E **81** (2010) 021702.

[58] G. Kitavtsev, J. Robbins, V. Slastikov, and A. Zarnescu, *Liquid crystal defects in the Landau-de Gennes theory in two dimensions beyond the one-constant approximation,* Math. Models Methods Appl. Sci. **26** (2016), no. 14 2769–2808.

[59] Y. Hu, Y. Y. Qu, and P. Zhang, *On the disclination lines of nematic liquid crystals,* COMMUN COMPUT PHYS. **19** (2016) 354379.

[60] X. Lamy, *Uniaxial symmetry in nematic liquid crystals,* Annales de lInstitut Henri Poincare (C) Non Linear Analysis **32** (2015), no. 5 11251144.

[61] R. Ignat, L. Nguyen, V. Slastikov, and A.Zarnescu, *Stability of the melting hedgehog in the Landau-de Gennes theory of nematic liquid crystals,* Arch. Ration. Mech. Anal. **215** (2015), no. 2 633–673.

[62] R. Ignat, L. Nguyen, V. Slastikov, and A.Zarnescu, *Stability of the vortex defect in the Landau-de Gennes theory for nematic liquid crystals.,* C. R. Math. Acad. Sci. Paris **351** (2013), no. 13-14 533–537.

[63] A. Sonnet, A. Kilian, and S. Hess., *Alignment tensor versus director: Description of defects in nematic liquid crystals,* Phys. Rev. E **52** (1995) 718–722.

[64] T. Lubensky, D. Pettey, N. Currier, and H. Stark, *Topological defects and interactions in nematic emulsions,* Phys. Rev. E **57** (1998), no. 1 610–625.

[65] V. Anderson, E. Terentjev, S. Meeker, J. Crain, and W. Poon, *Cellular solid behaviour of liquid crystal colloids 1: Phase separation and morphology, Eur. Phys. J. E* **4** (2001) 11–20.

[66] C. Denniston, E. Orlandini, and J. Yeomans, *Lattice Boltzmann simulations of liquid crystal hydrodynamics, Phys. Rev. E* **63** (2001) 056702.

[67] D. Svensek and S. Zumer, *Hydrodynamics of Pair-Annihilating Disclinations in SmC Films, Phys. Rev. Lett.* **90** (2003) 155501.

[68] P. Kossyrev, M. Ravnik, and S. Zumer, *Branching of colloidal chains in capillary-confined nematics, Phys. Rev. Lett.* **96** (2006) 048301.

[69] P. Patricio, M. Tasinkevych, and M. T. da Gama, *Colloidal dipolar interactions in 2D smectic-C films, Eur. Phys. J. E* **7** (2002) 117.

[70] V. Badalassi, H. Ceniceros, and S. Banerjee, *Computation of multiphase systems with phase field models, J. Comput. Phys.* **190** (2003), no. 2 371–397.

[71] G. Krausch, E. K. C. Dia, J. Marko, and F. Bates, *nterference of spinodal waves in thin polymer films, Macromolecules* **26** (1993), no. 21 5566–5571.

[72] G. Brown and A. Chakrabarti, *Ordering of block copolymer melts in confined geometry, Chem. Phys.* **102** (1995), no. 3 1440–1448.